

Dissertation
submitted to the
Combined Faculties for the Natural Sciences and for Mathematics
of the Ruperto-Carola University of Heidelberg, Germany
for the degree of
Doctor of Natural Sciences

put forward by

Diplom Physicist:
born in:

Silke Ulrich
Bad Wildungen

Oral examination: 02.12.2009

Optimization, Realization and Quality Assessment of Arc-Modulated Cone Beam Therapy

Referees:

Prof. Dr. Uwe Oelfke

Prof. Dr. Wolfgang Schlegel

Optimization, Realization and Quality Assessment of Arc-Modulated Cone Beam Therapy

Advanced radiation therapy techniques rely on a modulation of the fluence fields to optimize the clinical benefit of the treatment. This increased flexibility for intensity-modulated radiation therapy (IMRT) in comparison to conventional techniques allows the realization of excellent dose distributions. However, the advantage of superior dose distributions for IMRT usually requires an increased treatment time. A dose delivery technique with the potential to overcome this problem without impairing the treatment quality is dynamic rotation therapy in a single arc. This technique uses dynamic field shaping with a multi-leaf collimator (MLC) and a variable dose rate of the linac during irradiation to conform the dose distribution to the target volume. This thesis introduces an optimization concept for dynamic rotation therapy with variable dose rate, called arc-modulated cone beam therapy (AMCBT), that also accounts for all practical limitations of this approach imposed by the dose delivery hardware. This optimization algorithm is applied to assess the clinical potential of AMCBT via comparative treatment planning studies. Finally, a first realization of AMCBT based on a Siemens ArtisteTM linac equipped with a dynamic MLC was developed and investigated.

Optimierung, Realisierung und Qualitätsanalyse der Kegelstrahl-Rotationstherapie

Moderne Techniken in der Strahlentherapie verwenden eine Modulation der Fluenzfelder um den klinischen Nutzen einer Behandlung zu optimieren. Diese erhöhte Flexibilität für intensitätsmodulierte Strahlentherapie (IMRT) im Vergleich zu konventionellen Techniken ermöglicht die Realisierung von exzellenten Dosisverteilungen. Allerdings führt der Vorteil der verbesserten Dosisverteilung üblicherweise zu einer verlängerten Behandlungszeit. Eine Bestrahlungstechnik mit dem Potenzial dieses Problem zu überwinden ohne die Qualität der Behandlung zu beeinträchtigen ist die dynamische Rotationstherapie in einer einzelnen Gantryumdrehung. Diese Technik verwendet eine dynamische Anpassung des Bestrahlungsfeldes mittels eines Multi-Lamellen Kollimators (MLC) und eine variable Dosisrate des Beschleunigers während der Bestrahlung um die Dosisverteilung an das Targetvolumen anzupassen. In dieser Doktorarbeit wird ein Optimierungskonzept für die dynamische Rotationstherapie mit variabler Dosisrate, genannt Kegelstrahl-Rotationstherapie (AMCBT), vorgestellt, welches auch alle praktischen Einschränkungen durch die Bestrahlungs-Hardware berücksichtigt. Diese Optimierungsstrategie wurde verwendet um das klinische Potenzial von AMCBT in vergleichenden Planungsstudien zu untersuchen. Schließlich wurde eine erste Realisierung von AMCBT basierend auf einem Siemens ArtisteTM Beschleuniger mit dynamischen MLC entwickelt.

Contents

1	Introduction	1
2	Basics of Radiotherapy	5
2.1	Course of radiotherapy	5
2.2	Treatment delivery techniques	6
2.2.1	Fixed-field intensity-modulated radiation therapy	8
2.2.2	Dynamic rotational treatment techniques	8
2.3	Inverse treatment planning and dose optimization	10
2.3.1	Principle of inverse planning for IMRT	10
2.3.2	Optimization concepts for arc therapy with variable dose rate	12
2.4	Challenges in high precision radiotherapy	14
3	Optimization concept for arc-modulated cone beam therapy	15
3.1	The optimization concept	15
3.1.1	Automated generation of initial field shapes	16
3.1.2	Optimization loop	17
3.2	Hardware limitations	23
4	Treatment plan comparisons	27
4.1	Comparison of IMRT and AMCBT	28
4.1.1	Prostate carcinoma	28
4.1.2	Paraspinal tumor	30
4.1.3	Head tumor	31
4.2	Comparison of tomotherapy and AMCBT	33
4.2.1	Patient selection	34
4.2.2	Treatment planning	35
4.2.3	Results	36
4.3	Comparison of AMCBT and "idealized IMRT"	43
5	Stability of AMCBT treatment plan quality	47
5.1	Hardware limitations	47
5.2	Beam flattening filter	52
5.3	Variation of optimization and delivery parameters	56
5.3.1	Number of beam directions	59
5.3.2	Collimator angle	61
5.3.3	MLC leaf width	63
5.3.4	Constant dose rate	64
5.4	Sensitivity of rotational therapy to dose delivery errors	65

5.4.1	MLC	65
5.4.2	Dose rate	68
5.4.3	Gantry position	70
6	Hardware solution for AMCBT	73
6.1	Dose rate modulation	73
6.1.1	Dose rate modulation board	73
6.1.2	Experimental verification of dose rate modulation	74
6.2	MLC control	80
6.3	Gantry Rotation	82
6.4	Dosimetric verification of AMCBT delivery	85
6.4.1	Methods and materials	85
6.4.2	Results 1: multi-ionization chambers	86
6.4.3	Results 2: film measurement	90
6.5	Discussion	93
7	Discussion and conclusions	95
	Bibliography	101
	List of Figures	107
	List of Tables	109

1 Introduction

Radiotherapy is a widely used approach for the treatment of cancer patients. In Germany, the number of patients diagnosed with cancer is almost half a million every year [2]. Besides cardiovascular diseases cancer is the most common cause of death. Radiation therapy is employed to treat malignant tumors either as the primary therapy or in combination with other treatment modalities such as surgery or chemotherapy. Whether the intent of the treatment is curative or palliative depends on many factors, e.g. the tumor type, the tumor stage or the tumor location. Ionizing radiation damages the DNA of the cells, which might lead to cell death. The aim of a curative radiation therapy treatment is to destroy all cancerous cells. The delivery of a lethal dose to the target volume will always result in an irradiation of healthy tissue and organs at risk (OAR) in close proximity to the tumor. The objective for planning a radiation therapy treatment is the optimization of treatment parameters to achieve a high and homogenous dose in the tumor and to spare the surrounding tissues and OARs as much as possible from dose.

Developments in treatment planning and dose delivery techniques resulted in methods that allow dose shaping to highly complex geometries. In particular the introduction of intensity modulated radiotherapy (IMRT) significantly increased the number of degrees of freedom (DOFs) available for the dose delivery process. In standard cone beam IMRT techniques a few beam directions are selected for which the modulation of the fluence fields is optimized in the treatment planning process. Before starting the mathematical optimization initial field shapes are determined by a projection of the radiation target on to the isocentric plane perpendicular to the beam. Next, this field shape is subdivided into numerous fluence bixels. The relative fluence weights of those bixels are optimized by inverse planning. Finally, the optimized fluence profiles are converted into leaf-sequences for dose delivery with a multi-leaf collimator (MLC) - a procedure that often deteriorates the plan quality and leads to an unnecessary high number of beam segments.

To avoid this final step in the planning process which impairs the optimized dose distribution the method of direct aperture optimization (DAO) was developed [50]. In DAO the shape of individual beam segments and their corresponding fluence weights are determined simultaneously. This leads to the same plan quality with less segments and less monitor units (MU) compared to the standard two-step planning approach [51]. A reduction of the number of MUs needed for a specific treatment is beneficial since this reduces the scattered and leakage radiation that is unintentionally delivered to a patient. A consequence of an increased number of MUs is a higher risk to induce secondary malignancies with radiotherapy [21].

Besides fixed field IMRT techniques also rotational dose delivery techniques were developed and used to treat cancer patients. A rotational dose delivery technique which delivers highly conformal dose distributions is helical tomotherapy [29]. In helical tomotherapy the patient is moved through the gantry bore while the treatment is performed with rotating

fan beams, resulting in a helical dose delivery curve. The treatment machine for this technique is equipped with a fast pneumatically driven binary MLC to modulate the radiation during dose delivery.

Another rotational intensity-modulated irradiation technique performed with a conventional linear accelerator (linac) is intensity modulated arc therapy (IMAT) [75]. The required fluence modulation is achieved by superimposing the dose from several arcs of the rotating gantry with different weighting factors. A disadvantage of this technique is the long treatment time which is needed for the delivery of several arcs.

A dose delivery within a single rotation of the gantry would decrease the treatment time in comparison to other intensity-modulated radiotherapy techniques. To increase the flexibility in treatment planning the additional DOF to vary the dose rate during irradiation is introduced. This thesis project deals with a dose delivery technique which employs variable dose rate and variable field shapes during irradiation: arc-modulated cone beam therapy (AMCBT).

The objectives for the PhD thesis were

- the development of the optimization algorithm for arc-modulated cone beam therapy
- the assessment of achievable plan quality based on the developed optimization algorithm
- the development of a hardware solution for the delivery of dynamic arc therapy with variable dose rate.

The first publication of an optimization method for an intensity modulated treatment technique that is restricted to a single arc with the possibility to vary the dose rate was published in 2005 [10], called sweeping-window arc therapy (SWAT). The optimization algorithm for AMCBT was published in 2007 [61]. At that time there was no dose delivery hardware for dynamic arc therapy with variable dose rate available.

Based on the optimization algorithm described in [40] Varian developed a product for single arc therapy called RapidArcTM. This delivery method was introduced in some reference clinics in 2008 and by now there is a huge increase in the number of centers using RapidArcTM. Elekta also offers a dynamic arc product called VMATTM. The last year showed a rapid increase in publications dealing with dynamic arc techniques. In chapter 2.3.2 several of the different optimization algorithms are introduced, a summary of the results from different treatment plan comparisons is given in chapter 4.

This thesis is structured as follows: it starts with a short introduction of the basics of radiotherapy, the focus of chapter 2 is on treatment planning and dose delivery techniques. The optimization algorithm that was developed and tested during this work is described in detail in chapter 3. The next two chapters show results obtained with this direct aperture optimization algorithm. First, the dose distribution quality that is achievable with AMCBT is assessed in comparison to fixed field IMRT and helical tomotherapy. These studies show advantages and disadvantages of the new single arc dose delivery technique with variable dose rate in comparison to state-of-the-art dose delivery techniques. Chapter 4 closes those investigations with a comparison of AMCBT with an idealized form of IMRT. In chapter 5 the stability of the treatment plan quality was analysed for several hardware and optimization related aspects. In particular the influence of the following

factors on the final dose distribution were considered: hardware limitations, primary fluence, number of beam directions, employed collimator angle, MLC leaf width, variable vs. constant dose rate. Moreover, the sensitivity of rotational therapy to dose delivery errors was examined.

Besides the work on treatment planning a part of this thesis project is concerned with the realization of a dose delivery hardware for dynamic arc therapy with variable dose rate. The hardware solution for AMCBT that was implemented at the DKFZ is described in chapter 6. First measurements have shown the feasibility to perform dynamic rotation therapy with variable dose rate with a Siemens ArtisteTM linac.

Parts of this work have been previously presented at international conferences [60], [62], [63], [65] and were published in peer-reviewed journals [61], [64].

2 Basics of Radiotherapy

The aim of radiotherapy is the delivery of a lethal dose to the tumor while sparing the surrounding healthy tissue from dose as much as possible. In this chapter the steps of the radiation therapy treatment process are introduced, with a focus on the components that are most relevant for this thesis: treatment planning and dose delivery.

In radiation therapy, cancerous cells are killed by the deposition of dose by ionizing radiation. Energy dose is defined as the energy that is absorbed by the irradiated mass ($D = \frac{dE}{dm}$). Naturally, the deposition of dose does not only kill cancerous cells but also healthy cells. To avoid severe side effects caused by irradiation it is important to spare the surrounding tissue and radiation sensitive organs at risk (OARs) from dose as much as possible. To achieve this goal dose delivery techniques were developed that utilize a high number of degrees of freedom to shape the dose to the target volume.

Radiotherapy utilizes different types of radiation, e.g. photons, electrons, protons or heavy ions. Even though protons and heavier charged particles offer preferable depth dose characteristics, the majority of treatments are still performed with high energy photons. Within this thesis only treatments with high energy photons are considered.

2.1 Course of radiotherapy

A typical radiation therapy treatment consists of a number of steps, of which an overview is given in figure 2.1.

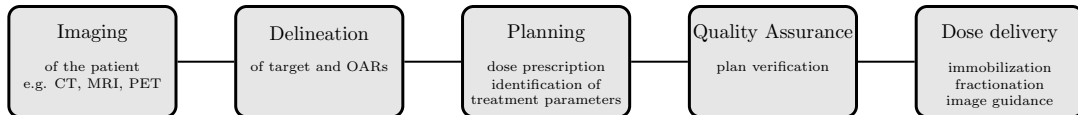


Figure 2.1: *Overview of the workflow of radiation therapy.*

To be able to deliver a high dose to the tumor the first step is the localization of the target volume. 3D imaging modalities, e.g. computer tomography (CT), magnetic resonance imaging (MRI) or positron emission tomography (PET) are used to obtain images of the tumor. On these images the target and OARs are delineated for planning of the radiation therapy treatment. The nomenclature used for target delineation is based on the ICRU report [23],[22]. The gross tumor volume (GTV) is the macroscopic extent of the tumor, as visible on the images. To account for microscopic tumor infiltration in the healthy tissue, the clinical target volume (CTV) is delineated around the GTV. The internal target volume (ITV) encompasses CTV plus a margin to account for movements of the tumor. To

account for positioning and other treatment technique related errors an additional margin is added, resulting in the planning target volume (PTV).

The next step is to plan the therapy. In forward planning the treatment parameters such as beam angle, field shape, field weight etc. are manually adjusted until the desired dose distribution is obtained. For a good tumor control probability together with a low normal tissue complication probability a high and homogeneous dose to the target and a low dose to OARs and normal tissue are needed. For more complex radiation therapy techniques with many degrees of freedom (DOF), forward planning does not result in optimal treatment plans any more and inverse planning is performed. A detailed description of inverse planning follows in section 2.3.

Another important issue in radiation therapy is quality assurance to ensure a safe and correct delivery of the planned dose distribution. Therefore regular checks are performed to test all functions of the linear accelerator (linac), e.g. the correct positioning of multi-leaf collimator (MLC) leaves or dosimetric tests. Moreover measurements are carried out to assure the feasibility to deliver the optimized treatment plan and to verify the dose distribution calculated by the treatment planning software.

After all these steps to prepare the treatment the next step is the dose delivery. In most cases the dose is not delivered in a single session but in a number of fractions. This is done to improve the ratio of healthy to cancerous cells that survive the irradiation. Because healthy cells have better repair mechanisms than cancerous cells, the time between two fractions is used to remove reparable damage of healthy cells and thus increase the number of surviving cells.

It is important that the patient is positioned during treatment exactly as during imaging. Otherwise the high dose region would not hit the tumor but instead the OARs and therefore the patient would not be cured and instead suffer from side effects. To ensure the same positioning the patient is immobilized for imaging and treatment. Modern image guided radiation therapy techniques utilize imaging during the course of treatment to ensure the correct positioning of the tumor during irradiation.

2.2 Treatment delivery techniques

For the treatment of a cancer patient with ionizing radiation different techniques are available. In brachytherapy the radiation source is inserted into the patient either inside or very close to the tumor. This delivery method is not discussed in this thesis as the focus is only on teletherapy techniques in which the radiation is delivered from a source outside of the patient.

A common machine for the generation of high energy photons is a linear electron accelerator. As the name already suggests, electrons are accelerated on a linear path with electromagnetic waves. After leaving the waveguide these high energy electrons are directed onto a X-ray target, usually made of tungsten, where they interact and generate bremsstrahlung photons. These photons pass through a primary fixed collimator which determines the maximum field size of the radiation field. The next component is a beam flattening filter which is designed to generate a uniform lateral dose profile. Basically, this filter is a cone-shaped material that absorbs more radiation in the center of the field and thus flattens the radiation field. Afterwards, secondary collimators such as jaws or

a multi-leaf collimator (MLC) are used to form individual field shapes for the respective treatment.

After entering a medium (e.g. a water phantom or the patient), the number of photons in the tissue decreases exponentially with increasing depth of penetration (Lambert-Beer law). The main interaction of photons in the energy range of 6 MV to 20 MV with tissue is the Compton effect. The incoming photon is interacting mainly with electrons in the tissue, thus transferring part of its energy to this electron. These secondary electrons then pass their energy by Coulomb scattering to the tissue. This results in a depth dose curve, as shown in figure 2.2, which is characterized by an initial build-up to a maximum dose in the entrance region of the medium and then an exponential decrease with depth.

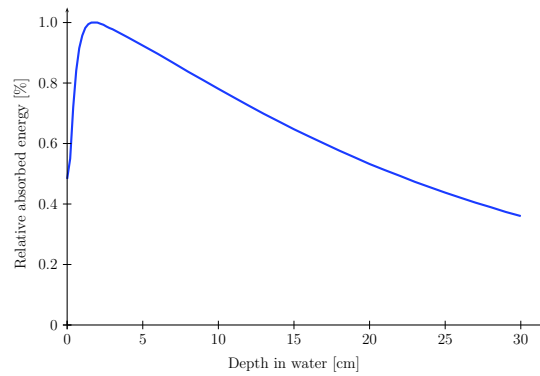


Figure 2.2: *Percentage depth dose curve for 6 MV photons.*

The goal of radiation therapy is to deliver a high and homogeneous dose to the tumor without delivering a high dose to organs at risk (OAR) or the normal tissue. Considering the depth dose curves for photons this is not possible for deep seated tumors with a single beam direction. Therefore, cancer treatment with photons employs several beam directions that overlap in the tumor volume. Rectangular fields from many beam directions would lead to a cylindrical dose distribution around the tumor. Since tumor shapes are quite complex in most cases, the next step is to conform the field shape to the contour of the tumor. For shaping the radiation fields MLCs might be used. MLCs consist of metallic plates, so called leaves, that can block the radiation field. The leaves are arranged in two opposing banks and each leaf can move independently.

With this conformal radiation therapy (CRT) technique, it is not possible to shape the dose distribution exactly to concave indentations in the target volume. The solution to this problem is to use intensity-modulated techniques. In IMRT, non-uniform fluence fields are used to conform the dose distribution closely to the volume of the tumor. This technique was proposed by Brahme in 1982 [9]. Since the first IMRT treatment 15 years ago in Houston, Texas, many different intensity-modulated techniques were developed and are frequently-used in clinical routine. A review on IMRT can be found in [7]. In the following section, an overview of different intensity-modulated treatment techniques is given.

2.2.1 Fixed-field intensity-modulated radiation therapy

Fixed field techniques are characterized by a static radiation source during irradiation. The number of beam directions for fixed field IMRT might vary for different treatment modalities and also treatment times vary in a wide range depending on the complexity of the respective case. For the two techniques described in this section the number of beam directions typically varies between 5 and 9 beams. An example of a dose delivery technique that uses more beam directions is the cyberknife (Referenz). The cyberknife is a robotic system equipped with a compact 6 MV linac which can irradiate the tumor from arbitrary beam directions with circular fields of different sizes. Here, two widely used techniques are described that are performed with a conventional linac equipped with a MLC.

Step-and-shoot IMRT

In Step-and-shoot IMRT a sequencing algorithm is used to translate the optimized fluence profile into a set of deliverable fluence fields with different weights and shapes, so called segments. The superposition of all these segments adds up to the desired fluence profile. During dose delivery, a MLC is used to block radiation outside the field shape. After all leaves were positioned correctly, the radiation is switched on to deliver the number of monitor units determined for the first segment. This is repeated for all segments from all beam directions. Therefore, the treatment time depends on the number of segments. The more segments are used, the closer the superposition of all segments matches the optimized non-uniform fluence field, but also the treatment time increases. Moreover the scatter radiation to the patient increases if more segments are used, which leads to a higher integral dose in the patient.

Dynamic IMRT

In dynamic IMRT the leaves of the MLC are moved during irradiation. To deliver the optimized fluence profile, the speed of the leaves varies while they cross the radiation field. If the gradient of the fluence profile is positive, the leading leaf is moving with the maximum achievable speed and the trailing leaf is used for fluence modulation. The speed of both leaves can be calculated according to the Stein equations [53]:

$$I'(x) \geq 0 : \quad v_L(x) = v_{max} \quad \text{and} \quad v_T(x) = \frac{v_{max}}{1 + v_{max} * I'(x)}$$

$$I'(x) < 0 : \quad v_T(x) = v_{max} \quad \text{and} \quad v_L(x) = \frac{v_{max}}{1 - v_{max} * I'(x)}$$

The treatment time needed for dynamic IMRT depends on the maximum speed of the MLC leaves.

2.2.2 Dynamic rotational treatment techniques

In rotational therapy techniques the radiation source moves around the patient during dose delivery. The large number of beam directions allows for delivery of highly conformal dose distributions. Compared to fixed field techniques, the dose to the normal tissue is spread over a larger volume.

Tomotherapy

The concept for tomotherapy was introduced in 1993 [29]. This technique employs a rotating fan beam to deliver the dose to the patient. To modulate the dose delivery a fast, pneumatically driven binary collimator is used. In serial tomotherapy the patient is shifted for the width of the fan beam after each rotation of the radiation source. So the dose distribution is made up of dose slices delivered to the patient, which explains the name tomotherapy which literally means "slice therapy".

Serial tomotherapy was the first IMRT technique, with its first patient treatment in 1994 in Houston, Texas. The dose delivery in slices bears the risk of an under- or overdosage between the slices if the patient positioning is not absolutely correct. Moreover, the treatment time for this technique is very long. To solve these helical tomotherapy was developed. In this technique the patient is moved through the gantry bore while the radiation source rotates, resulting in a helical dose application. For helical tomotherapy a specifically designed treatment machine is necessary, which has been available for clinical use since 2002.

Arc therapy

Arc therapy is performed with a conventional C-arm shaped linear accelerator. The dose is delivered by rotational cone beams of varying shapes. The idea for arc therapy with dynamic field shaping was first described in 1965 by Takahashi, called conformation radiotherapy. Instead of using fields with a predefined width, the shape of the fields conforms to the shape of the treatment volume [58].

To achieve dose distributions with conformality equal to that of IMRT or tomotherapy, Yu proposed in 1995 intensity-modulated arc therapy (IMAT) [75]. In IMAT, dose delivery is performed in several superimposing arcs. Each arc can have a different weighting factor, but within one arc the dose rate is constant. The shape of each aperture can vary within the limitations set by the MLC during dose delivery.

Since treatment times for IMAT are long and the treatment planning process is complicated, IMAT was not widely used in clinics. An idea was proposed to decrease the treatment time by the delivery of the complete dose in a single rotation of the gantry with variable dose rate and/or gantry speed. The first paper showing the feasibility of this approach to achieve conformal dose distributions was published in 2005 [10]. At the same time, the optimization algorithm presented in this work was developed and published in 2006 [59], [61]. Recently, many approaches for single arc therapy optimization were proposed, some of them will be reviewed in section 2.3.2. The clinical implementation of single arc techniques started in 2008. The first commercially available system was advertised with the trade name RapidArcTM by Varian and is in clinical use since January 2008 [1]. Not long after the announcement of RapidArcTM Elekta also marketed a product with dynamic MLC and variable dose rate named VMATTM. By now there is a wide adoption of these techniques for the treatment of cancer patients. Throughout this thesis, arc-modulated cone beam therapy (AMCBT) will be used as acronym for dynamic rotational therapy with variable dose rate.

Reasons for the fast implementation of single arc techniques into clinics are presumably the fast treatment times together with the ability to deliver highly conformal dose dis-

tributions. Compared to helical tomotherapy, arc therapy has the advantage that it is performed with a conventional linac, and therefore it is possible to use the same treatment unit for different treatment techniques. The use of a conventional linac also offers the possibility to use non-coplanar beams.

2.3 Inverse treatment planning and dose optimization

2.3.1 Principle of inverse planning for IMRT

Inverse treatment planning was developed for the optimization of treatment plans for complex treatment techniques that employ many degrees of freedom. Before the invention of intensity-modulated radiotherapy, the degrees of freedom for therapy planning were the beam directions, the field shapes and field weights. Manual adjustment of these parameters to find an acceptable dose distribution was possible within a reasonable time. With IMRT, the number of DOF is rapidly increased by adding the flexibility to vary the fluence from each beam direction. The fluence field is subdivided into so called bixels and the weight of each bixel can have an arbitrary weighting factor. The total number of DOF is the number of beam directions times the number of bixels per beam. Depending on the size of the bixels and the size of the target volume, the number of DOFs is in the order of several hundred and therefore it is not feasible to adjust the plan parameters manually.

In inverse planning, the order of planning is interchanged: instead of adjusting the treatment parameters by a trial and error process to get an acceptable dose distribution, the user specifies dose constraints and an inverse planning program is used to find the treatment parameters which result in a dose distribution that most closely matches the given constraints. A review of inverse planning can be found in [72].

For this work the research version of the inverse planning system KonRad was used [37] [39] [38]. Therefore, the explanations given in this section are oriented towards the implementation of the KonRad inverse planning software. Other inverse planning systems may adopt different parameters to specify the desired dose distribution (i.e. biological objectives instead of physical dose objectives), other measures to define the difference between the actual and the planned dose constraints or other optimization algorithms.

The basic information required by KonRad for treatment planning is a CT image of the patient anatomy with contoured volumes of interest (VOI). The three dimensional data set of the patient is divided into voxels with a resolution of 2.62 mm^3 and each voxel is allocated to a specific VOI. Based on this data, a pencil beam algorithm is used to determine the dose matrices D_{ij}^k for the predefined field shapes Z_k irradiated with a uniform fluence. The element D_{ij}^k of this matrix stores the dose that is deposited in voxel i by bixel j from beam direction k for unit fluence. The total dose d_i in voxel i from the field shapes Z_k of all beam directions contributing with the bixel weights w_{jk} is given by:

$$d_i = \sum_{k=1}^{N_k} \sum_{j=1}^{N_{jk}} D_{ij}^k w_{jk}$$

with N_k the number of beam directions and N_{jk} the number of bixels j from beam direction k .

The first step in inverse planning is the definition of dose constraints. In KonRad, for each VOI a minimum and a maximum constraint is defined as well as a penalty factor that determines the importance of this constraint. For organs at risk the minimum dose constraint is set to 0. These standard dose constraints can be formulated in terms of a ‘prescribed’ dose d_i^{pres} and a penalty factor s_i for each voxel i as:

$$d_i^{pres} = \begin{cases} d_{VOI}^{max} \\ d_{VOI}^{min} \\ d_i \end{cases}, \quad s_i = \begin{cases} s_{VOI}^{max} & \text{if } d_i > d_{VOI}^{max} \\ s_{VOI}^{min} & \text{if } d_i < d_{VOI}^{min} \\ 1 & \text{if } d_{VOI}^{min} < d_i < d_{VOI}^{max} \end{cases}$$

The goal of the optimization process is the minimization of an objective function. The objective function in KonRad is a weighted sum of the square of the deviations from the given constraints:

$$F = \sum_i^{N_i} s_i (d_i - d_i^{pres})^2$$

here N_i is the number of considered voxels.

Standard 2-step planning approach

The standard approach for IMRT planning consists of two steps: (1) Optimization of the bixel weights, followed by (2) sequencing the fluence profiles into deliverable MLC segments.

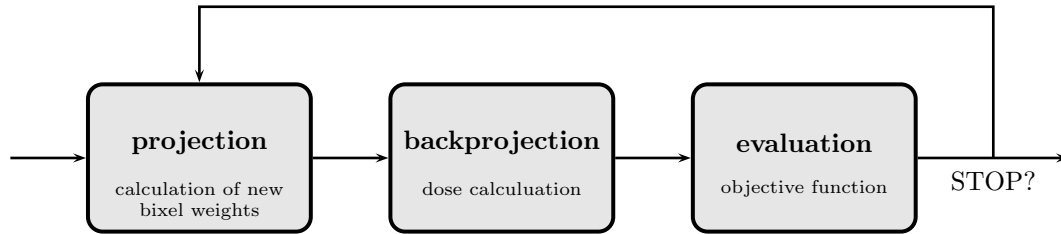


Figure 2.3: *Optimization loop*

In this approach the bixel weights are the parameters that are varied to minimize the difference between the actual dose distribution and the predefined treatment goals. The only constraint on the weights for a physically feasible solution is that all fluence weights need to be positive. For the optimization of bixel weights, different optimization algorithms were proposed and reported in the literature, most of them iterative search algorithms. For this work a modified Newton-gradient method was used [37]. The flowchart in figure 2.3 shows the optimization cycle. Based on the mathematical optimization method used for treatment planning a new set of bixel weights w_{jk} is calculated (projection). In the next step the dose d_i in each voxel i is calculated for the new set of bixel weights (back-projection). In the last step the new dose distribution is evaluated with the objective

function. If any pre-defined abort criterion is fulfilled the optimization stops, otherwise a new set of bixel weights is calculated.

The result from this optimization is a fluence map for each beam direction used for treatment planning. There is not a single set of fluence maps that represents the optimal solution, but due to the degeneracy of the related inverse planning problem there are a number of different fluence maps that lead to almost the same dose distribution. During the optimization the fluence weights can have arbitrary values. For the delivery of a treatment plan it is necessary to convert these optimized fluence maps into a set of deliverable apertures. Based on the number of intensity levels allowed in the final fluence distribution, the bixel weights are modified to fixed values (stratification) and with a leaf-sequencing algorithm translated into deliverable beam segments.

This second step can lead to a degradation of the dose distribution quality that was achieved during the optimization process. The stratification of the bixel weights causes a change of the optimized fluence map and therefore a change in the final dose distribution. Different attempts have been made to reduce the complexity of a fluence distribution, e.g. setting intensity limits or applying smoothing filters.

Direct aperture optimization

A single step treatment planning method was proposed in 2002 [50], called direct aperture optimization (DAO). Instead of optimizing the bixel weights, the segment weights and shapes are optimized. This approach directly generates a deliverable treatment plan and thus eliminates the sequencing step. Since the number of segments per beam direction is chosen prior to the optimization the user can control the complexity of the treatment plan.

It was shown in several studies comparing DAO and 2-step planning for IMRT, that the number of segments and also the number of monitor units can be significantly reduced with DAO [51], [17], [66], [3], [13], [24].

2.3.2 Optimization concepts for arc therapy with variable dose rate

The first publication of an optimization concept for arc therapy with a variable dose rate was published in 2005. In the last four years there were a number of publications of different optimization approaches for this dose delivery technique, but not all of them will be reviewed here. The optimization concepts of the first three publications on this topic are based on a DAO algorithm, as described in the sections on sweeping window arc therapy, arc-modulated cone beam therapy and volumetric modulated arc therapy. To show the alternative of a 2-step planning approach for single arc therapy the concept of arc-modulated radiation therapy is also introduced.

Sweeping window arc therapy

The concept of sweeping-window arc therapy (SWAT) was developed for the optimization of treatment plans for IMAT, but with the ability to vary the dose rate during rotation [10]. For the optimization, a direct aperture optimization is used that optimizes the field shapes with simulated annealing and the weights are calculated analytically. The name SWAT

originates from the initialization of the field shapes: a leaf sequence of sweeping windows that move back and forth across the target as the gantry rotates. Target conformal fields are not close to an optimal solution and therefore a successful optimization starting with target conformal fields is difficult. By imposing more variation in the field shapes it was shown that a successful optimization of dose distributions is possible.

Arc-modulated cone beam therapy

Arc-modulated cone beam therapy (AMCBT) is the optimization algorithm that was developed during this project. A detailed description of the algorithm follows in chapter 3. The optimization concept is also based on a direct optimization of field shapes and field weights. The main differences to other optimization algorithms are the choice of the initial solution and the use of a tabu search algorithm to optimize the field shapes [61].

Volumetric modulated arc therapy

The key feature of the algorithm for inverse planning of volumetric modulated arc therapy (VMAT) [40] is the increasing angular sampling rate during the optimization. At the beginning of the optimization only a few beam directions (or control points) are included in the optimization. For these control points the field shapes and weights are optimized with a stochastic algorithm that is similar to simulated annealing. Since the angular interval between two consecutive control points is large, the restrictions imposed by the hardware are not severe. Moreover the algorithm converges faster because of the limited number of DOF. After a predefined number of iterations, the number of control points is doubled. This increases the dose modeling accuracy during the optimization.

The treatment planning software used for RapidArcTM (Varian) is based on this optimization algorithm.

Arc-modulated radiation therapy

This approach for the optimization of single arc treatments was proposed by Wang in 2008 [71]. In contrast to the approaches described so far this algorithm is not a direct aperture optimization but uses a two step approach similar to conventional IMRT planning. The first step is an optimization of the fluence profiles for a fixed number of beam directions, e.g. separated by 10° . In this optimization no hardware restrictions are considered and therefore the resulting dose distribution is of the same quality that any IMRT plan could possibly achieve. In conventional IMRT planning the leaf sequencing step is used to find aperture shapes that closely match the ideal intensity profile. In AMRT the focus is on finding apertures that can deliver the same dose as the optimized intensity pattern. With graph algorithms an optimal set of aperture shapes is calculated considering restrictions given by the maximal speed of the MLC leaves. In a post-optimization step the weights of the apertures for each beam angle are determined based on a least-square optimization. For the next step the following assumption was made: the dose delivered from a given intensity profile at a fixed gantry angle could also be delivered through apertures from neighboring beam angles. The stack of apertures at a fixed angle is moved to neighboring angles and a geometrical adjustment of the shifted aperture shapes is performed.

2.4 Challenges in high precision radiotherapy

The description of the radiotherapy workflow in section 2.1 gives an overview of issues that are important for a successful treatment and the last two sections reviewed in more detail treatment delivery and inverse planning. High-precision radiation therapy is only possible if all essential steps in the course of the treatment are performed accurately. For example, the better dose shaping capabilities of modern dose delivery techniques also require a more exact localization of the tumor.

The first source of error in the localization of the tumor occurs in the delineation of the target. Even though developments in imaging have improved the quality of images there are still uncertainties in the exact delineation of the target. Several studies were performed to compare the delineation of a target on the same image data by different physicians. These studies showed a large inter observer variability in the delineation, e.g. a recent study on lung cancer patients [70].

Another issue that needs to be considered in high-precision radiation therapy is motion of the target or deformations of the patient anatomy during the course of treatment. For example, tumors in the lung might move due to respiration or in prostate cancer the position of the tumor depends on the filling of the bladder. Motion of the tumor during dose delivery is called intra-fraction motion and between two radiation fractions it is called inter-fraction motion. To detect changes in the patient anatomy between two fractions an image of the patient prior to each treatment could be performed. For this purpose in-room CTs or imaging devices included in the medical linear accelerator, e.g. kV or MV cone beam CTs, could be used. A possible disadvantage of imaging the patient each day is the additional dose that is delivered to the patient.

There are various approaches to account for motion during dose delivery and this is currently an active research area. It would go beyond the scope of this work to give a detailed overview of motion effects in radiotherapy and techniques to account therefore, a review can be found in [73]. As one possibility to account for motion the concept of tumor tracking should be introduced here. The idea of tumor tracking is to follow the movements of the target with the irradiation beam during dose delivery. Therefore it is necessary to monitor the target during irradiation. This could, for example, be done with x-ray imaging (MV or kV), with electromagnetic transponders implanted in the tumor (e.g. Calypso beacons), or with optical imaging of the patient surface (e.g. ExacTrac, BrainLab or RPM (real-time position monitor), Varian). If the position of the tumor changes during treatment, the radiation field moves to follow the movement of the target.

The improved dose shaping capabilities that are possible due to the large number of degrees of freedom also lead to drawbacks in the dose delivery. The field sizes used for irradiation in IMRT are much smaller than for conventional techniques, and thus the ratio of MUs per Gy is higher than for conventional techniques. This leads to an increase in leakage radiation and the patient receives more scattered radiation. This widespread additional dose might cause radiation-induced secondary cancer.

Another disadvantage of fixed field IMRT or tomotherapy compared to conventional treatment techniques is the increase in treatment time. This leads to a decrease in the number of patients that could be treated at one treatment machine. For the patient it implies a longer time on the treatment couch and movements might occur more often.

3 Optimization concept for arc-modulated cone beam therapy

This chapter deals with the optimization concept for AMCBT. The first implementation of this concept was accomplished during my diploma thesis and is reported in [59]. The optimization for AMCBT has been integrated into the research version of the inverse planning system KonRad [39]. In section 3.1 the algorithm is described including several enhancements made during the course of the PhD. The most important extension of the algorithm was the inclusion of constraints that are imposed by the delivery hardware. Section 3.2 describes which hardware constraints are important for rotation therapy, how they were considered in the frame of the optimization and how they influence the dose distribution.

3.1 The optimization concept

The degrees of freedom (DOF) for the optimization are the field shapes Z_k and the beam weights w_k for a predefined number of beam directions N_k . The field shapes are made up of small beam elements called bixels j , i.e. $Z_k = \{j | j \text{ is an open bixel from beam direction } k\}$. Altogether the number of DOFs is in the same order of magnitude as for an IMRT optimization.

The explanations given in section 2.3 for dose calculation and dose prescription for IMRT are the same for AMCBT. In contrast to standard IMRT all bixels from one beam direction k will have the same weight for AMCBT: $w_{jk} \rightarrow w_k$. This leads to a simplification in the matrix multiplication needed to calculate the dose in each voxel i . The dose contribution in voxel i from field shape Z_k is the sum of the dose values from all respective bixels j :

$$D_i(Z_k) = \sum_{j \in Z_k} D_{ij}^k$$

The total dose d_i in voxel i is then:

$$d_i = \sum_{k=1}^{N_k} D_i(Z_k) w_k$$

The bixel concept is used to have a fast method to update the dose distribution after changing the field shapes or beam weights. The disadvantage of this approach is that it is only possible to alter the field shapes in steps of at least one bixel. The other set of variables, the beam weights, can have arbitrary positive values.

During the optimization the objective function F is minimized:

$$F = \sum_i^{N_i} s_i (d_i - d_i^{pres})^2$$

In the following sections the new optimization concept is introduced step by step. The first section describes the generation of the initial field shapes. Next, the optimization loop is introduced by first explaining the optimization of the beam weights and the field shapes separately. At the end of section 3.1.2 both methods are combined to one optimization loop for the beam weights and the field shapes.

3.1.1 Automated generation of initial field shapes

A key feature of this algorithm is the selection of the initial set of field shapes Z_k . Target conformal field shapes usually lead to unnecessarily long optimization times and to solutions of limited quality. Therefore the OARs are already considered in the generation of the initial field shapes.

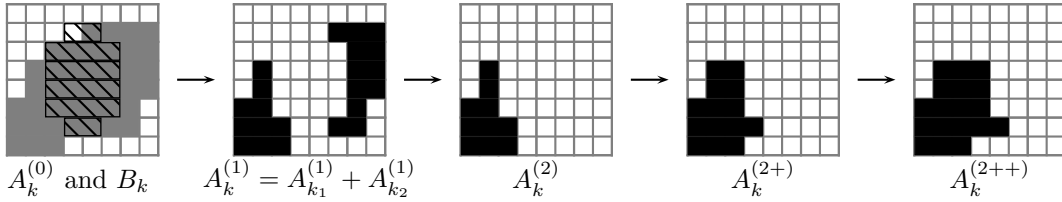


Figure 3.1: Generation of the initial field shapes: On the left side of the figure the projections of the target (grey) and an OAR (dashed) to the isocenter plane are shown together with the bixel grid. The method by which the initial field shapes are determined from these projections is explained in the text.

Figure 3.1 shows how the initial field shapes are determined from the projection of the target and an OAR to the isocenter plane. The bixels that are covered by the projection of the target are shown in grey and the ones for the projection of the OAR are labeled by dashed lines. All bixels that belong to the target are included in the bixel set $A_k^{(0)}$, the bixels in the projection of the OAR in the set B_k . The first step is to open all bixels that belong to $A_k^{(0)}$, except the ones that belong to B_k , i.e.,

$$A_k^{(1)} = A_k^{(0)} - (A_k^{(0)} \cap B_k)$$

If this set of bixels is not continuously connected, e.g. $A_k^{(1)} = A_{k_1}^{(1)} + A_{k_2}^{(1)}$, it is not possible to shape this field with an MLC. In this case all subsets $A_{k_i}^{(1)}$ that are smaller than a predefined number N_c of bixels are closed. If there are still more subsets than one, only the first subset $A_{k_1}^{(1)}$ is opened:

$$A_k^{(2)} = A_{k_1}^{(1)}$$

In this case, only one part of the tumor volume is irradiated. After a gantry rotation of 180° , the projections of the target and the OAR will look very similar, and then the remaining part of the tumor is irradiated. So after a full rotation of the gantry a homogeneous dose distribution in the tumor volume usually can be achieved.

The thus determined bixel set $A_k^{(2)}$ as initial field shape would naturally lead to low doses

in the target volume next to the OAR. Therefore some additional bixels are opened. Starting from $A_k^{(2)}$ the algorithm checks which adjacent bixels belong to $A_k^{(0)}$ and adds them to the set $A_k^{(2+)}$. This could be performed by adding more classes of neighboring bixels which creates the corresponding bixel sets $A_k^{(2++)}$, $A_k^{(2+++)}$ and so on. The initial field shapes Z_k consist of all bixels that belong e.g. to the set $A_k^{(2++)}$:

$$Z_k = \{j | j \in A_k^{(2++)}\}$$

How many additional bixels are needed clearly depends on the size of the bixels, the geometry of the patient anatomy and the beam quality of the employed treatment modality. The approach to spare OARs from dose with the initial fields is only useful if the geometrical projections of the OARs separate the target volume for at least some beam directions. Example beam's eye view (BEV) projections of different patient geometries are shown in figure 3.2.

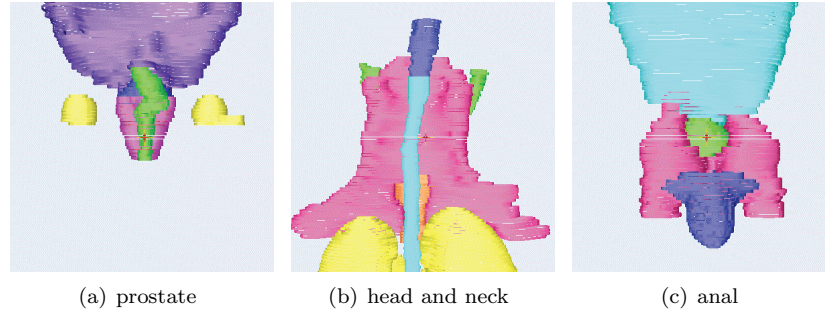


Figure 3.2: *Beams Eye View of different tumor types.*

For the prostate case, the rectum is separating the tumor in two separate BEV projections and was therefore used for the generation of the initial field shapes. In case of the head and neck tumors this role was assigned to a combination of brain stem and spinal cord. To employ, for example, the parotids as the separating OAR for initial field generation does not help the algorithm to find a better and faster solution. For the anal carcinoma cases there are no OARs that naturally separate the target volume in the BEV for any beam direction. Therefore help VOIs might be generated for the generation of the initial field shapes.

A boost volume is a challenge for arc therapy, because the fluence is not modulated within one field and therefore it is complicated to have two dose levels within one arc. To improve the dose gradient between PTV and boost, the boost volume might also be considered in the generation of the initial set of field shapes. To give an example, for some beam directions, e.g. all beams in the angular interval between 310° and 360° gantry angle, only bixels covering the boost (and not the PTV) might be opened in the initial field shapes.

3.1.2 Optimization loop

The optimization loop starts after the calculation of the dose matrices for the initial field shapes Z_k . At first the beam weights w_k are optimized for these field shapes with a

gradient algorithm until a stopping criteria is fulfilled. Then the tabu search algorithm, which optimizes the field shapes, starts.

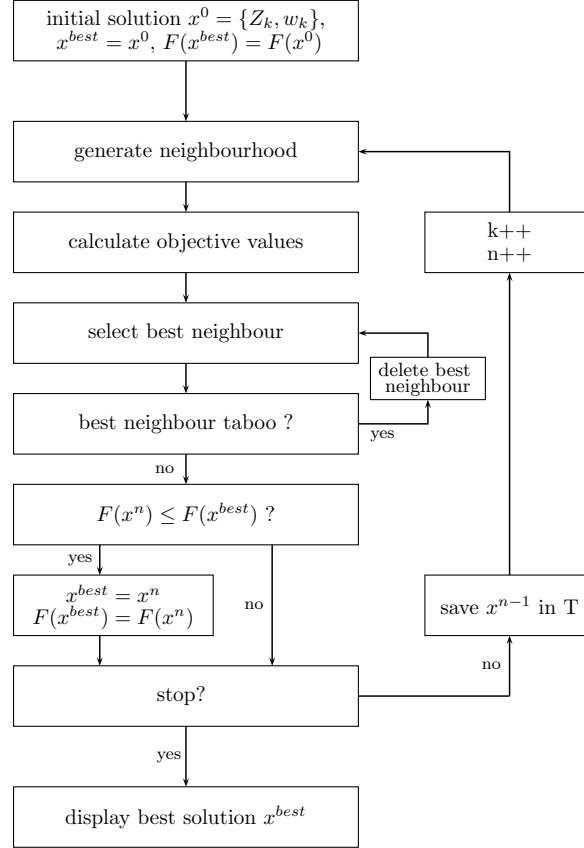


Figure 3.3: Flowchart of the tabu search algorithm, which is used to optimize the field shapes. All steps are explained in the text.

Optimization of beam weights

The first optimization loop is a modified Newton gradient method to optimize the beam weights w_k for a given set of field shapes [6]. This gradient algorithm is commonly used for the optimization of treatment plans for IMRT. It was already implemented in the treatment planning system KonRad to optimize the bixel weights for an IMRT treatment, so only minor changes were necessary to use it for AMCBT.

After the generation of the initial field shapes this gradient algorithm is called for the first time. Optimization of field weights is performed until the percentage difference between the current and the previous objective function value is smaller than a predefined threshold. Later on it is combined with the tabu search algorithm to optimize the beam weights together with the field shapes.

Optimization of field shapes

The optimization of the field shapes is not possible with a gradient algorithm, because the search space is not convex. To overcome local minima a tabu search algorithm was used. Tabu search is an iterative neighborhood method that was developed by Glover [19] in 1986. In this subsection the implementation of the algorithm for the optimization of the field shapes is described. An overview of the procedure is given in figure 3.3.

The input data for the tabu search is the initial solution $x^0 = \{Z_k, w_k\}$, which is the set of the initial field shapes Z_k and the optimized beam weights w_k . The optimal set x^{best} is determined by an iterative approach where x^n represents the solution derived in iteration n . The beam weights w_k are not changed in this part of the optimization loop and therefore are not considered explicitly.

The initial solution x^0 and the value of the objective function $F(x^0)$ are stored as best solution $x^{best} = x^0$ and best objective value $F(x^{best})$.

Generation of neighborhood

The first step in the tabu search is the generation of the so called "neighborhood" of one single field shape Z_l at angle l . In general, the neighborhood $N(Z_k)$ of a field shape Z_k consists of all field shapes $N_{\pm j}(Z_k)$ which have one additional bixel j opened or closed at the edge of the field, i.e.

$$N_{\pm j}(Z_k) = Z_k \pm j$$

The plus or minus sign indicates whether the bixel j was opened or closed.

To create a neighbor one leaf of the MLC must be opened or closed for one bixel width. As an example, figure 3.4 shows a field shape and four neighbors of this field. The maximum number of neighbors is four times the number of open leaf pairs, but usually the number is lower because a field shape can only be enlarged if the dose matrix of the adjacent bixel was calculated. In the first iteration the number of neighbors is only twice the number of leaf pairs, because no dose matrix outside the initial field shapes is calculated.

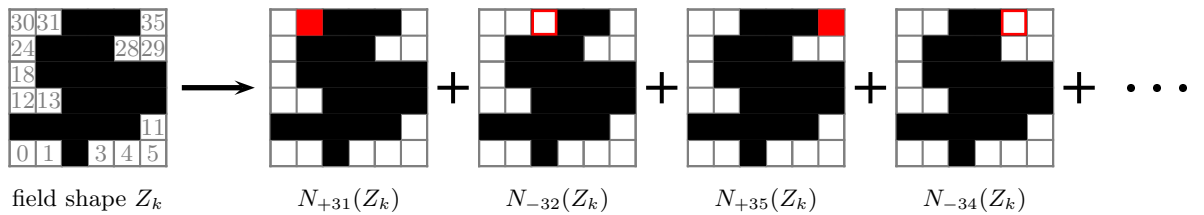


Figure 3.4: Generation of a neighborhood. On the left side an arbitrary field shape Z_k is shown together with the bixel numbers. The other four pictures show neighbors of this field shape, the changed bixel is highlighted in red.

Ranking of new neighborhood field shapes

The next step in the tabu algorithm is the calculation of the objective function for each neighbor. By opening or closing a bixel j , the dose information for the field shape changes:

$$D_i(N_{\pm j}(Z_k)) = D_i(Z_k) \pm D_{ij}^k$$

Thus the dose d_i in some voxels is different and the value of the objective function changes accordingly. A calculation of the objective function for many neighbors is very time consuming, therefore only the difference from the actual objective function $F(x^0)$ is calculated and added to $F(x^0)$. This is only possible if we assume that the weights of the beams w_k do not change.

In this calculation only the dose values for voxels which are influenced by the opened or closed bixel j from beam direction k are recalculated:

$$d_i^{new} = d_i^{old} \pm D_{ij}^k w_k$$

The dose value d_i is changed in all voxels i with $D_{ij}^k \neq 0$. These voxels are indicated with i' in the following. The new value of the objective function is then determined by subtracting the old contributions from the changed voxels and adding the new contributions of these voxels to the old objective function $F(x^{n-1}) = F(\{Z_1, \dots, Z_l, \dots, Z_N; w_1, \dots, w_N\})$.

$$F(\{Z_1, \dots, N_{\pm j}(Z_l), \dots, Z_N; w_1, \dots, w_N\}) = F(\{Z_1, \dots, Z_l, \dots, Z_N; w_1, \dots, w_N\}) + \Delta F$$

with

$$\Delta F = \sum_{i'} s_{i'}^{new} (d_{i'}^{new} - d_{i'}^{pres,new})^2 - \sum_{i'} s_{i'}^{old} (d_{i'}^{old} - d_{i'}^{pres,old})^2$$

The result of the first two steps in the tabu search is the neighborhood $N(Z_l)$ of the field shape Z_l and the corresponding values of the objective function

$$F(\{Z_1, \dots, N_{\pm j}(Z_l), \dots, Z_N; w_1, \dots, w_N\}):$$

$$N(Z_l) = \{N_{\pm j}(Z_l)\}$$

Selection of a non-tabu new field shape

In the next step the best neighbor $N_{best}(Z_l)$ - that means the one with the lowest objective value $F(\{Z_1, \dots, N_{\pm j}(Z_l), \dots, Z_N; w_1, \dots, w_N\})$ - is selected from the neighborhood $N(Z_l)$. The new solution x^n consists of the same field shapes Z_k and weights w_k like the last solution x^{n-1} , except for the field shape Z_l which is substituted by $N_{best}(Z_l)$. Next, the algorithm checks if the new solution x^n is in the tabu list. The tabu list T contains all solutions that were visited in the last t iterations, here t denotes the maximum length of the tabu list:

$$T = \{x^n | n_{act} - n < t\}$$

with n_{act} the number of already performed iterations. If less than t iterations were performed yet, the length of the tabu list is n_{act} .

If a solution is already contained in the tabu list it is not allowed to be visited again, thus the solution is said to be "taboo". The purpose of this list is to prevent the algorithm from oscillating between a few solutions. The algorithm allows solutions with a higher value of the objective function in order to escape from local minima in the non-convex objective function. However, an unlimited tabu list bears the risk that the algorithm can not find the global minimum because too many restrictions block the way to the optimum.

If the neighbor for one iteration is tabu, it is deleted from the neighborhood and the second best neighbor is chosen. The first neighbor that is not tabu is selected as the new field

shape at angle l .

Next, for the new solution x^n with field shape $N_{best}(Z_l)$ instead of Z_l , the objective function is calculated. If this value is lower than the best one so far, x^n is stored as the best solution x^{best} .

If no exit condition is met, the last solution x^{n-1} is stored in the tabu list and the neighborhood of the next field shape is calculated. After changing one bixel in all field shapes Z_k the algorithm starts again with changing one bixel in the first field shape until a stopping criteria is fulfilled.

Optimization of beam weights and leaf positions

So far the optimization of the beam weights and the leaf positions has been discussed separately. But the optimal beam weights w_k will change by optimizing the field shapes and thus both classes of DOFs need to be considered during the optimization loop. The modification of one bixel in one field shape does not change the beam weights w_k very much. That is why we could use the fast method to calculate the objective functions for the neighbors. But as more field shapes are changed the beam weights will begin to deviate from the new optimal weight factors.

The combination of both optimization loops is shown in figure 3.5. Starting with the initial field shapes Z_k and optimized beam weights w_k the tabu algorithm is used to find the best solution in the neighborhood of the field shape from the first beam direction.

The new solution x^n is generated from the last solution x^{n-1} by replacing the old field shape Z_k with the new one $N_{best}(Z_k)$, even if this leads to a higher value of the objective function.

As already mentioned, the beam weights do not change very much with the modification of one field shape. For this reason the next three steps are not obligatory for each iteration step as indicated also in figure 3.5. But after modifying several field shapes, the difference between the optimal beam weights and the actual beam weights will increase and a recalculation is required.

Before the start of the optimization process the user has to schedule how often the beam weights should be recalculated, e.g., in every p -th step of the iteration. Moreover it is possible to define the number of gradient optimization iteration steps q , e.g. $p = 3$ and $q = 4$ means a recalculation of beam weights w_k in every third iteration with four gradient iteration steps for the beam weight optimization.

The next step in the optimization loop is the query if the actual value of the objective function $F(x^n)$ is lower than the best one $F(x^{best})$. If this is true, the actual solution is stored as the best one. In this case the counter for the number of iterations since the last improvement n_{best} is set to zero. Otherwise n_{best} is incremented.

The optimization stops if either a maximum number of iterations n^{max} was performed, or the algorithm did not find a better solution for more than n_{best}^{max} iterations. If one of the stopping conditions is met, the algorithm stores the optimal field shapes and weighting factors. Otherwise the number of iterations n is incremented and the tabu algorithm searches for the best bixel in the next field shape.

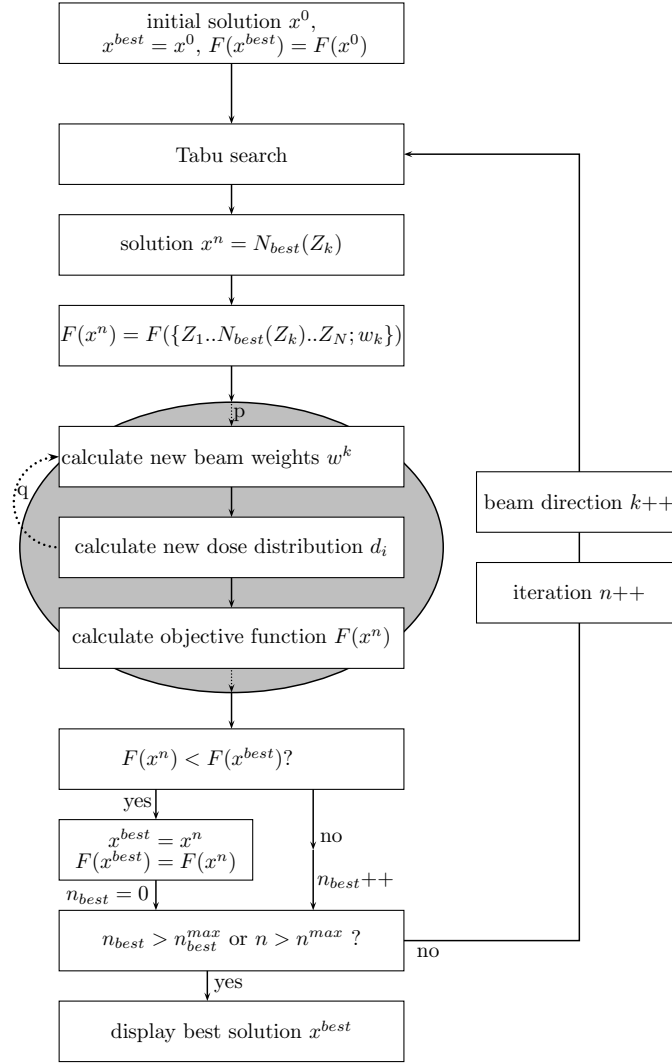


Figure 3.5: Optimization loop for AMCBT. It is shown how the tabu search (field shapes) and the gradient algorithm (beam weights) are working together. All steps are explained in the text.

3.2 Hardware limitations

In the last section the limitations that are imposed by the hardware were not considered during the optimization process. The hardware limitations for dynamic arc therapy are:

- the rotation speed of the gantry
- the dose rate of the accelerator
 - minimum and maximum dose rate
 - maximum variation of the dose rate
- and the maximum leaf speed of the MLC

For AMCBT the gantry rotation speed is assumed to be constant for a single treatment, but it can change for different cases. Since the other constraints depend on the rotation speed of the gantry - e.g. a faster rotation speed results in less time for the leaves to move between consecutive angles - this value is determined first in the optimization. The initialization of the optimization starts without constraints - the initial field shapes are generated according to the description in 3.1.1 and the optimization of the beam weights for these shapes is performed until the first stopping criteria is fulfilled. At this point in the optimization the "optimal" gantry rotation speed for the treatment is determined. The field weights comply with the number of monitor units for a 10*10 cm field, but also for irregular field shapes, as present for AMCBT, an estimation of the number of MUs from the field weights is possible. With this approximated number of MUs per beam a mean value MU_{mean}^{beam} of the number of MUs per beam could be calculated. Taking also the mean dose rate $DR_{mean} = \frac{DR_{min} + DR_{max}}{2}$ of the linac into account, the gantry rotation speed is calculated according to the following formula:

$$v_{gantry} = \frac{DR_{mean}}{MU_{mean}^{beam}} * \frac{\varphi_{stop} - \varphi_{start}}{N_{beams}}$$

with φ_{start} , φ_{stop} the start and stop angle of the gantry rotation and N_{beams} the number of beams. If the calculated gantry rotation speed exceeds the limitations physically achievable with the employed hardware, it is set to the respective value.

There are several assumptions that led to this approach to consider the hardware constraints, however it is not claimed that this approach is the best one. The reason to choose the number of monitor units instead of the maximum leaf travel distance to determine the gantry rotation speed is based on a study of how hardware limitations influence the quality of the dose distribution. As shown in the results of section 5.1, for AMCBT with the hardware constraints that are based on the performance characteristics of a Siemens ArtiseTM linac equipped with a 160MLCTM, it was seen that only the dose rate constraints led to a degradation of the plan quality. Therefore, the rotation speed was chosen as to best match the requirements of the respective plan on the dose rate. To simplify the insertion of hardware constraints into the optimization concept the gantry rotation speed is kept constant for the optimization. Moreover the beam directions are assumed to be evenly spaced between the start and stop angle.

After fixing the gantry rotation speed, the calculation of all other limitations that need

to be considered during the optimization process is straightforward. The time between consecutive apertures is:

$$t_{field} = \frac{\varphi_{stop} - \varphi_{start}}{N_{Beams} * v_{Gantry}}$$

With the minimum (DR_{min}) and the maximum dose rate (DR_{max}) of the linac the number of MUs or the field weight, respectively, are determined:

$$MU_{min}^{field} = DR_{min} * t_{field}$$

$$MU_{max}^{field} = DR_{max} * t_{field}$$

The maximum change of the number of monitor units between consecutive beam directions is:

$$MU_{change} = DR_{change} * t_{field}^2$$

with DR_{change} being the maximum achievable change of the dose rate per minute. The limitations of the beam weights were included into the backprojection of the gradient algorithm. If any beam weight exceeds the maximum or minimum value, it is set to the respective value. If the difference between the beam weights of the actual beam and the former beam is more than MU_{change} , the new weight is modified to stay within the limitations.

The last hardware limitation that needs to be considered is imposed by the MLC that is used to shape the radiation fields. With the gantry speed v_{gantry} and the maximum physical achievable leaf speed v_{leaf} of the MLC, the maximum distance that the leaves can move between consecutive beam directions is:

$$x_{Leaf} = v_{Leaf} * t_{field}$$

Since this limitation was not considered in the generation of the initial field shapes the first step is to detect all leaf positions that violate this constraint. Therefore consecutive apertures are compared and if for any leaf the distance of the movement is too large both apertures are changed to fulfill the constraint. If possible, the leaf positions that are too far apart are moved towards each other. If this would lead to a violation of the limitation with the neighboring apertures, only the aperture shape that stays within the limits is changed. During the optimization all changes which violate the MLC limitations are rejected.

A flowchart summarizing the insertion of hardware constraints into the optimization concept for AMCBT is shown in figure 3.6.

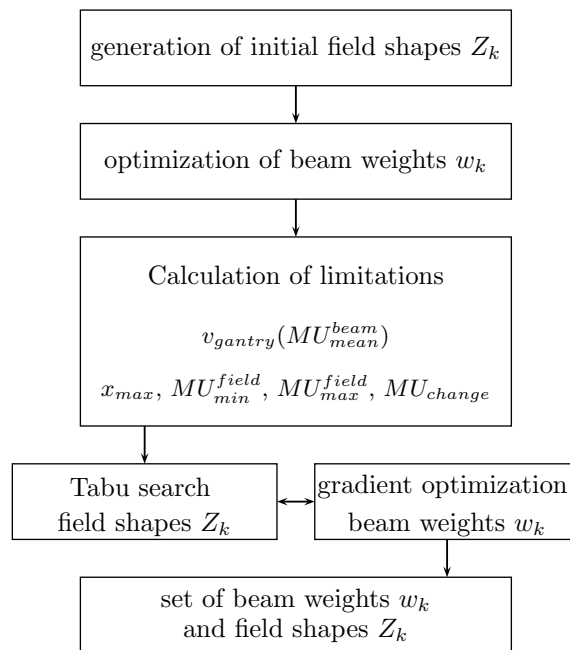


Figure 3.6: Flowchart of the optimization algorithm with the inclusion of hardware limitations.

4 Treatment plan comparisons

In this chapter the dose distribution quality that is achievable with arc-modulated cone beam therapy is examined. For different tumor sites single arc treatment plans are compared to fixed-field IMRT and helical tomotherapy plans and the advantages and disadvantages of the techniques are discussed. Moreover, a comparison of AMCBT and an "idealized IMRT" technique is performed to investigate possible dosimetric advantages of arc therapy in several rotations (section 4.3).

Since the clinical implementation of single arc techniques several treatment plan comparison were published. Studies have shown a good plan quality for prostate tumors [42], benign intracranial tumors [16] and tumors of the cervix uteri [11]. The investigation of prostate carcinoma cases showed a more favorable dose distribution for VMAT with a variable dose rate compared to five-field IMRT or VMAT with a constant dose rate. Moreover, the number of MUs was lower for VMAT compared to IMRT. The plan comparison for small intracranial tumors with a mean PTV volume of 4.22 cm^3 showed a similar target coverage and sparing of OARs. The conformity index, CI_{95} , for RapidArcTM was lower compared to IMRT and higher compared to helical tomotherapy. The integral dose for RapidArcTM was higher compared to IMRT, but lower compared to tomotherapy. The comparison for cervix uteri radiotherapy between RapidArcTM and fixed field IMRT showed an improved sparing of OARs and healthy tissue for RapidArcTM with the same target coverage.

A recent dosimetric comparison of RapidArcTM and helical tomotherapy between two institutions in the US for four different cancer sites - brain, head-and-neck, lung and prostate - arrived at the same conclusion: the treatment time and number of MUs is reduced with RapidArcTM, while the target dose uniformity and coverage is better with helical tomotherapy. Moreover, helical tomotherapy provided a slightly better dose sparing of most OARs [46].

RapidArcTM dose delivery is just beginning to be used in the clinic, and therefore no outcome data from treated patients is available yet. All comparisons between single arc therapy and other intensity-modulated treatment techniques are based on treatment plan comparisons. The comparison of helical tomotherapy and RapidArcTM, two competing technologies manufactured by different commercial vendors, led to a controversy on the advantages and disadvantages of both dose delivery techniques. Triggered by statements made in a paper on the commissioning and quality assurance of RapidArcTM [28], there was a discussion of beam-on-times and the impact of MLC leaf width and slice thickness on the dose conformity for RapidArcTM and helical tomotherapy ([30], [33], [27]). It should be noted that all statements concerning the quality of dose distributions or the performance of any dose delivery technique naturally depend on the current implementation of the techniques. Delivery parameters such as leaf width, pitch etc. used for the treatment plan comparisons in this chapter were chosen to be consistent with typical clinical settings.

The influence of several delivery parameters on the final dose distribution obtained with AMCBT is further examined in chapter 5.

4.1 Comparison of IMRT and AMCBT

The three selected clinical cases are typical indications for a treatment with intensity modulated fluence fields - a radiation sensitive organ is enclosed by a concave shaped target. For all calculations the bixel resolution was set to $(5\text{ mm})^2$, the voxel size to $(2.62\text{ mm})^3$ and the photon beam energy was 6 MV. The optimization process for AMCBT was performed with $N_k = 36$ beam directions. As an initial solution, the bixel sets A_k^{2++} were taken (see 3.1.2) with a minimum field size of $N_c = 5$ bixels. The length of the tabu list was set to $t = 100$, but actually no tabu event occurred. A re-calculation of the beam weights was performed once in every iteration step ($p = 1, q = 1$). The dose constraints were the same for the IMRT and the AMCBT optimization processes.

4.1.1 Prostate carcinoma

The first example considered is a prostate carcinoma which is shown in figure 4.1. The dose was delivered in 38 fractions of 2 Gy. For the gross tumor volume (GTV) the maximum and minimum dose constraint was 76 Gy. The GTV is surrounded by the clinical target volume (CTV) with a margin of 5 mm without overlapping any OARs and the planning target volume (PTV) with a margin of 5 mm to the CTV with possible overlap of OARs. The maximum and minimum dose constraints for these two volumes was 66 Gy.

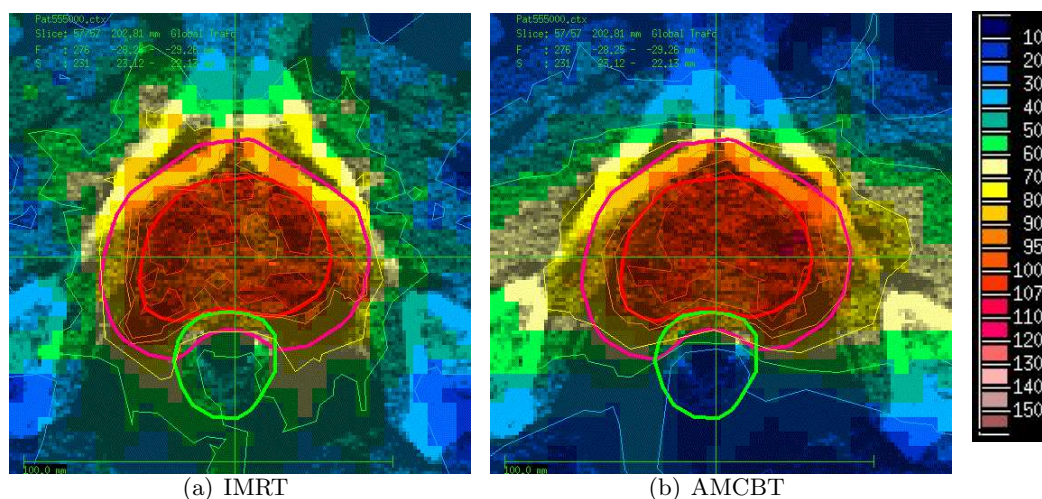


Figure 4.1: Comparison of the dose distributions in a transversal slice for IMRT and AMCBT for the prostate case. A dose of 100% in the dose scale equals 76 Gy. The rectum is contoured in green, the PTV in pink and the GTV in red.

The following OARs were considered during the optimization loop: the rectum with a dose limit of 45 Gy, the bladder with a dose limit of 30 Gy and the femurs with a dose limit of 30 Gy. For the IMRT optimization, dose volume constraints were used to achieve a better sparing of the rectum and the normal tissue was included in the optimization with a maximum dose of 20 Gy.

For the IMRT treatment plan seven equidistant beam directions were selected. The number of intensity levels for the subsequent stratification of the fluence maps was four, which resulted in 43 IMRT segments to be delivered.

A comparison of the dose distributions for the AMCBT and IMRT treatment plans is shown in the dose volume histogram (DVH) in figure 4.2. The curves are normalized so that 50% of the GTV receive at least 100% of the prescribed dose.

In the GTV the maximal dose is lower for AMCBT (solid line) and the minimal dose is higher, which results in a more homogeneous dose distribution in the target volume.

In the rectum the mean dose is much lower for AMCBT than for IMRT, i.e., $\bar{D}_{IMRT} = 35.8\%$ of the prescribed dose and $\bar{D}_{AMCBT} = 27.2\%$. However, in the high dose region of the rectum the dose distribution is slightly better for IMRT, although the respective maximal dose is higher for IMRT, i.e., $D_{IMRT}^{max} = 102.1\%$ compared to $D_{AMCBT}^{max} = 100.1\%$.

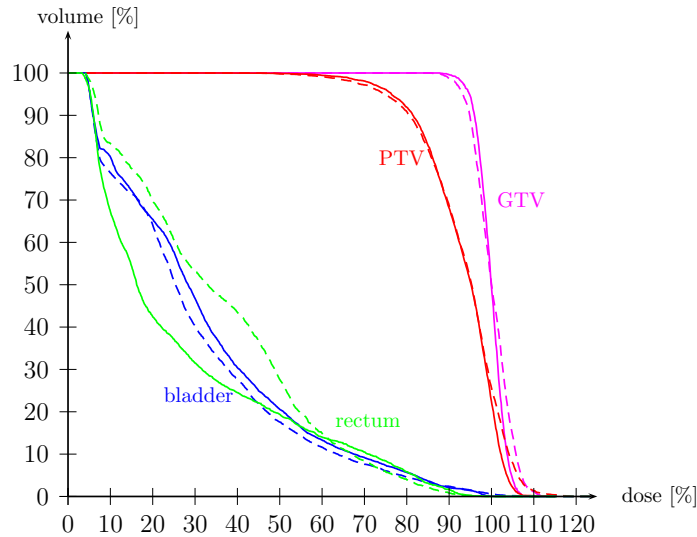


Figure 4.2: Comparison of the DVH curves for IMRT (dashed) and AMCBT (solid) for the prostate case.

Figure 4.1 displays the dose distributions on a transversal CT-slice. The conformation of the dose distribution to the target volume and the sparing of the rectum is visible for both treatment plans. AMCBT is especially good in the region of the rectum not directly adjacent to the target.

Another notable difference between the treatment plans for AMCBT and IMRT is the number of MUs to be delivered. For the IMRT treatment the total number of MUs was 1100 MUs in comparison to 639 MUs for AMCBT.

	case 1		case 2		case 3	
	IMRT	AMCBT	IMRT	AMCBT	IMRT	AMCBT
GTV min	85.9	87.9	56.4	71.8	76.7	78.4
GTV max	115.7	109.4	115	110.6	115.7	106
Rectum mean	35.8	27.2	53.4	36.1	45.5	28.7
Rectum max	102.1	100	98.2	98.1	92.4	96.9
MUs	1100	639	1202	580	1190	549

Table 4.1: Dose values (in % of the prescribed dose for the GTV) and number of monitor units (MUs) for three different prostate carcinomas. The dose distribution on a transversal slice for case 1 is shown in figure 4.1

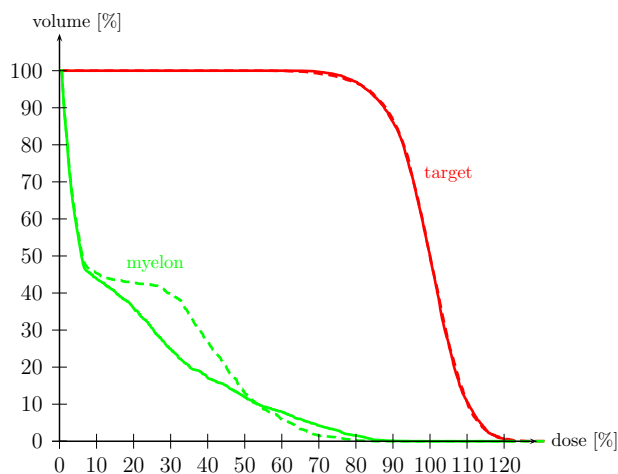
Calculations for other prostate carcinomas showed similar results: a reduction of the number of MUs, a similar dose distribution in the target, which was mostly slightly better for AMCBT, and a much lower mean dose in the rectum for AMCBT accompanied by a somewhat better sparing in the high dose region (see table 4.1).

4.1.2 Paraspinal tumor

The second example considered is a paraspinal tumor. In this case the spinal cord is enclosed by the tumor volume, as shown in figure 4.4. Therefore, the spinal cord was chosen as the most important OAR for the generation of the initial field shapes. For the tumor the maximum and minimum dose constraint was 60 Gy. A maximum dose constraint of 35 Gy was set for the spinal cord, the kidney and the intestine. The normal tissue was only considered for the IMRT treatment plan with a constraint of 20 Gy.

For the IMRT treatment, five equidistant coplanar beam directions were chosen and the number of intensity levels was six which results in 51 IMRT segments for this treatment. To optimize the AMCBT treatment plan 1000 iterations were performed. The resulting DVHs and the transversal views for this example are shown in figures 4.3 and 4.4.

Figure 4.3: Comparison of the DVH curves for IMRT (dashed) and AMCBT (solid) for the paraspinal case. Displayed are the target (red) and spinal cord (green).



The dose distribution in the target volume is very similar for IMRT and AMCBT. The mean dose in the most important OAR, the spinal cord, is $\bar{D}_{IMRT}^{spinalcord} = 21.7\%$ of the prescribed dose for the IMRT treatment plan and $\bar{D}_{AMCBT}^{spinalcord} = 18.8\%$ for AMCBT. But for this case the maximal dose is higher for AMCBT ($D_{IMRT}^{spinalcord,max} = 85.7\%$, $D_{AMCBT}^{spinalcord,max} = 95.2\%$). The difference in the number of MUs is not as pronounced as for the prostate cases, but nevertheless the number of MUs could be reduced from 592 MUs for IMRT to 512 MUs for AMCBT.

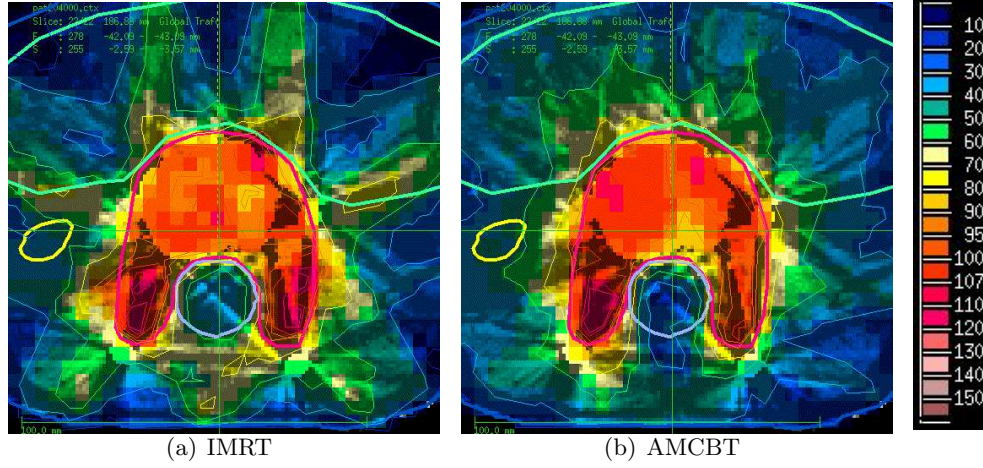


Figure 4.4: Comparison of the dose distributions in a transversal slice for IMRT and AMCBT for the paraspinal case. A dose of 100% in the dose scale equals 60 Gy. The following VOIs are shown in this slice: Target (pink), spinal cord (purple), intestine (green) and kidney (yellow).

4.1.3 Head tumor

The geometry of the anatomical structures for this clinical case is more complicated than the two cases considered before. The irregularly shaped target is in close proximity to the optical nerves and other organs at risk such as brainstem, spinal cord and optical chiasm that all have to be spared from unacceptable dose burden. This geometry is not appropriate for the generation of initial field shapes, as explained in section 3.1.2, due to the high number of sensitive structures. Instead, the optimization started with target conformal field shapes.

The clinical IMRT plan was calculated with 7 beam directions and a bixel size of 2.75 mm. The voxel size was 1.6 mm. To generate the treatment plan for AMCBT the number of beam directions was 36 and the same bixel and voxel size as for the IMRT plan were used. The number of optimization steps was increased to 5000 due to the higher complexity of this case. Moreover, the declaration of the neighbourhood was changed for the first 2000 iteration steps. Instead of changing the field shapes by opening or closing 1 bixel, the neighbourhood was calculated for field changes of 3 bixels.

A comparison of the DVHs for the IMRT and AMCBT treatment plans is shown in figure 4.6. Besides the target volume the DVH is shown for the right and left optical nerve,

the right and left eyes, the brainstem, the spinal cord and the optical chiasm. For this patient the dose coverage of the target volume and the dose conformity is better for IMRT. The sparing of the OARs is similar for both treatment techniques. Some OARs receive less dose with the IMRT treatment plan, e.g. a mean dose of 18.4 Gy in the brain stem compared to 21.6 Gy for AMCBT. Other OARs are better spared with AMCBT, e.g. the left optical nerve and eye and also the chiasm. The dose to the normal tissue is higher for AMCBT. The possibility of a very conformal dose distribution with both delivery methods is demonstrated in the transversal slices in figure 4.5.

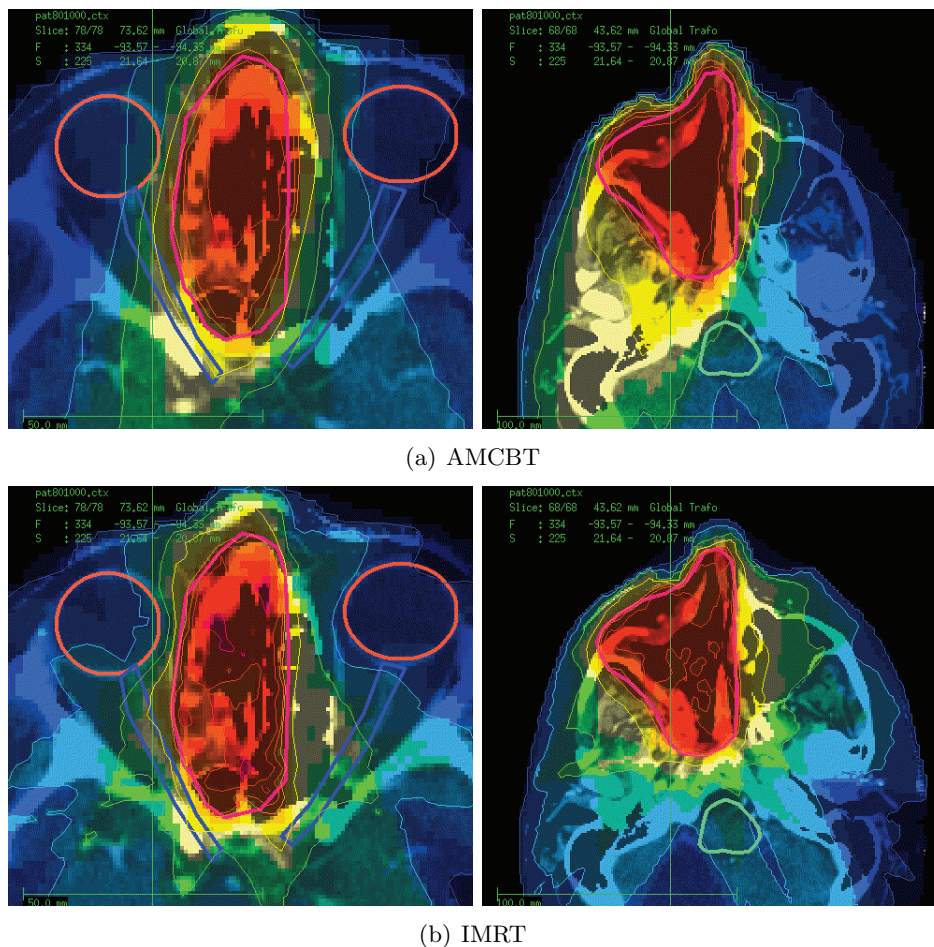


Figure 4.5: Comparison of the dose distributions in a transversal slice for AMCBT and IMRT. The target is contoured in pink, the eyes in orange, the optical chiasm in turquoise and the optical nerves in blue.

The left side of the figure shows a CT-slice where the target is close to the optical nerves and the eyes. A sparing of the OARs and a good coverage of the target is visible for both treatment plans. The other CT-slice display shows a higher dose to the normal tissue for the AMCBT treatment plan.

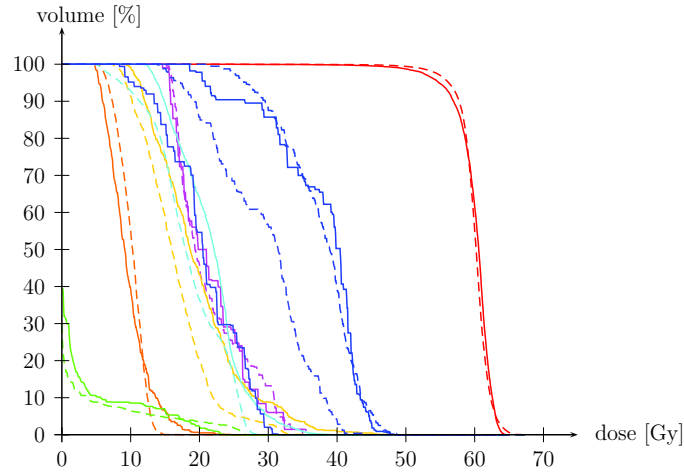


Figure 4.6: Comparison of the DVH curves for IMRT (dashed) and AMCBT (solid). Displayed are the target (red), the optical nerves (blue), the eyes (orange), the optical chiasm (pink), the brainstem (turquoise) and the spinal cord (green).

The required number of MUs for a prescribed dose of 60 Gy that is to be delivered in 30 fractions is 231 MUs per fraction for AMCBT and 1026 MUs for IMRT.

4.2 Comparison of tomotherapy and AMCBT

Tomotherapy can produce distributions with a good target coverage and homogeneity together with individualized sparing of organs at risk (OARs) in a variety of tumors [[56], [55], [43], [44], [12]]. Several planning studies for the treatment of head-and-neck cancer showed that helical tomotherapy can realize sharper dose gradients and a better sparing of parotid glands compared with step-and-shoot IMRT or stereotactic radiotherapy [[67], [15], [52], [49]]. In addition, new treatment possibilities were realized by the means of tomotherapy, for example the delivery of whole abdominal irradiation [45].

In the present study three different types of cancer with varying position, geometry and boost concepts were used to compare the two planning methods in different clinical settings. The rationale for IMRT of anal cancer is the sparing of the genitals, bladder and small bowel and, consequently, an improvement of the efficacy-toxicity ratio [31]. Combined radiochemotherapy is the standard treatment of anal carcinoma and has proven to be highly effective in sphincter preservation [[18], [36]]. However, radiation associated toxicity can cause treatment interruptions and thereby diminish the tumor control probability [14]. Low genitourinary and gastrointestinal toxicity rates were reported when using IMRT by several groups [[47], [32]].

The motivation of using IMRT in head-and-neck cancer has been outlined in numerous articles and reviews and is mainly based upon the need for dose reduction to parotid glands, spinal cord, esophagus and larynx [20]. Besides the improvement of local control IMRT has a huge impact upon quality of life by reducing long term toxicity as xerostomia and

dysphagia [54].

Similar to the background of the two previously described tumor types the main motivation for the use of IMRT in the management of prostate cancer is to enable a safe dose escalation while sparing the rectum and thereby reducing gastrointestinal toxicity [76].

The aim of this study is the evaluation of single arc therapy in comparison to helical tomotherapy.

4.2.1 Patient selection

To cover a wide variety of different geometries with different complexity and different objectives we compared treatment plans for tomotherapy and single arc therapy for three different tumor sites. The total number of patients was nine, all of which had been previously treated with helical tomotherapy.

Prostate carcinoma:

Three patients with histologically proven intermediate risk localized prostate cancer were chosen for this planning comparison.

Patient 1: T2cN0M0, Gleason score 7(4+3), PSA-level 5.3 ng/ml

Patient 2: T1cN0M0, Gleason score 6(3+3), PSA-level 18 ng/ml

Patient 3: T1cN0M0, Gleason score 7(4+3), PSA-level 4.9 ng/ml

A dose of 76 Gy was prescribed to 95% of the volume of the prostate itself. This volume was extended by 6 mm and modified to include the seminal vesicles and exclude the rectum. A median dose of 70 Gy was prescribed to this volume. In a third step this volume again was extended by 6 mm and a median dose of 66 Gy was prescribed. The treatment was performed in 35 fractions. The organs at risk included the bladder, rectum and femoral heads. For the OARs no specified dose limits were used, instead the dose was minimized as much as possible.

Anal carcinoma:

Three patients with histologically confirmed anal cancer that had previously undergone combined radiochemotherapy were chosen for the study. The patients' characteristic were as follows:

Patient 1: T2N2M0

Patient 2: T3N1M0

Patient 3: T2N1M1 (single bone metastasis)

The CTV included the tumor region plus the draining lymphatics in the perirectal, internal and external iliac and inguinal region. A safety margin of 5 mm was added to create the PTV to account for setup uncertainties. A median dose of 45 Gy was prescribed in 25 fractions. The organs at risk were genitals, bladder and small bowel.

Oropharynx carcinoma:

Three patients with squamous cell carcinoma of the oropharynx with a postoperative status were chosen.

Patient 1: pT3pN1M0, with extracapsular tumor extension and positive resection margins

Patient 2: pT3cN2M0, the patient had refused lymph node dissection, only marginal tumor resection was performed

Patient 3: pT2mpN2cM0L1, with positive resection margins

The boost region was defined as the preoperative tumor region detected on contrast enhanced CT and MRI scans plus a 5 mm margin. The CTV encompasses the draining lymphatics. A median dose of 70.4 Gy in 32 fractions was prescribed to the primary tumor region and to the involved lymph nodes within a simultaneous integrated boost concept. A median dose of 57.4 Gy in 32 fractions was prescribed to the cervical and supraclavicular lymphatics. Organs at risk were spinal cord, brain stem, parotis, larynx, esophageal sphincter and lungs.

4.2.2 Treatment planning

Tomotherapy

Helical tomotherapy planning was done with the Hi-Art Tomotherapy planning system version 2.2.1.55 (Madison, Wisconsin, USA). Contouring was performed with the Oncologist software by Siemens. The dose delivery was accomplished with a longitudinal field width of 2.5 cm and a pitch of 0.287 with 6 MV x-rays.

Arc-modulated cone beam therapy

Single arc treatment plans were optimized with the algorithm described in section 3. For dose delivery of rotational treatment plans the following constraints of the dose delivery hardware were considered. The gantry rotates with a constant speed ranging between $50^\circ/\text{min}$ and $360^\circ/\text{min}$. The speed of the rotation is determined by the total number of MUs required for the treatment. During the rotation the dose rate can be varied between $30 \text{ MU}/\text{min}$ and $300 \text{ MU}/\text{min}$. The maximum speed of the MLC leaves is restricted to $3 \text{ cm}/\text{s}$.

All treatment plans were optimized with a voxel size of $(2.62\text{mm})^3$, a bixel size of $(5\text{mm})^2$ and a beam energy of 6 MeV. The number of beam directions used during the optimization was 51 for the prostate and head and neck cases, which is the same number as used for tomotherapy planning. Due to limited memory of our optimization hardware the number of beam directions for the optimization of the anal carcinoma cases was limited to 36.

In a post-optimization step the number of beam directions was increased from 51 or 36 beams to 360 beams by linear interpolation of the determined MLC positions and MUs. The final dose distributions for these treatment plans were then calculated with a clinically approved pencil beam algorithm.

Treatment plan comparison

Treatment plans, structure sets and CT data were imported in Dicom format from the HT planning system to the treatment planning system VIRTUOS. Consequently, the AMCBT optimization process could be based on the same CT data and the same VOIs that were used for tomotherapy. The evaluation of the treatment plans was done by the same physician for AMCBT and helical tomotherapy.

For plan comparison we used dose-volume based parameters. For OARs the mean dose and $D_{1\%}$ are calculated. For the target we compared $D_{1\%}$, $D_{99\%}$, mean dose, dose coverage, e.g.

the ratio of the target volume receiving 95% of the prescribed dose and the total target volume, and conformity, e.g. the ratio of target volume receiving 95% of the dose and the total volume receiving 95% of the dose. Moreover, the integral dose was calculated as the product of the mean dose delivered to the volume bounded by the patient body contour.

4.2.3 Results

Prostate carcinoma

In table 4.2 the mean dose values for the three patients involved in this study are listed. The mean dose-volume histogram is shown in figure 4.8, and examples of the dose distributions for helical tomotherapy and arc-therapy in a transversal and a sagittal slice for one patient are displayed in figure 4.7.

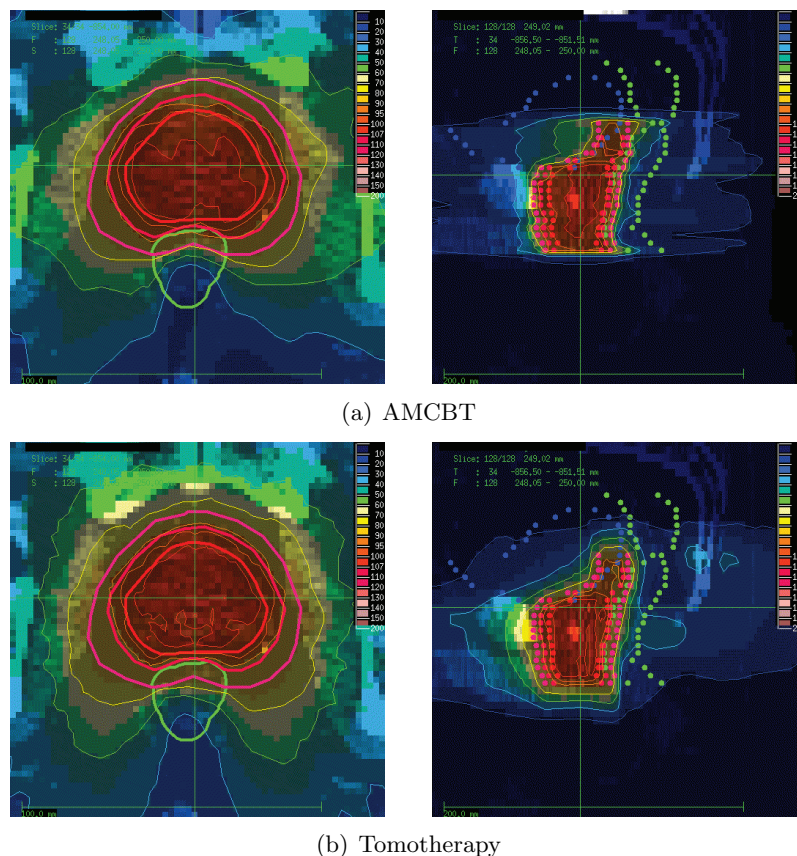


Figure 4.7: Dose distribution for prostate patient 1. The left column shows a transversal slice, the right column a sagittal slice. The 100% isodose line refers to 78 Gy.

With single arc therapy a very good dose sparing of the rectum is possible. Also the mean dose to the bladder is lower for arc therapy. The conformity of the dose to the target is

organ	Tomo	AMCBT
GTV		
$D_{99\%}$	72.8	73.2
$D_{1\%}$	80.4	81.9
mean	78.0	78.0
CTV		
$D_{99\%}$	68.0	66.3
$D_{1\%}$	80.1	81.5
mean	74.9	75.3
PTV		
$D_{99\%}$	59.6	58.3
$D_{1\%}$	79.8	81.7
mean	71.4	72.2
coverage	0.68	0.75
conformity	1.00	0.99
Rectum		
$D_{1\%}$	67.5	72.1
mean	24.4	21.7
Bladder		
$D_{1\%}$	72.8	75.1
mean	25.2	23.6
Integral dose	172.0	145.8

Table 4.2: Mean dose values for tomotherapy (Tomo) and AMCBT for three patients with prostate cancer (dose values in Gy, integral dose in Gyl).

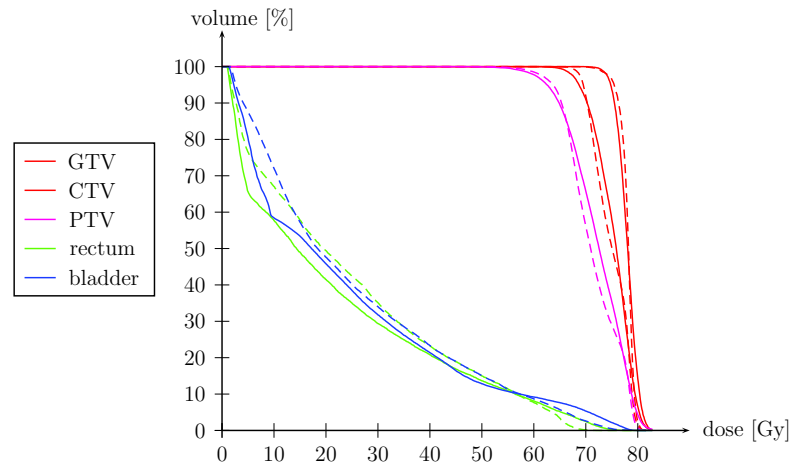


Figure 4.8: Mean dose volume histogram for the three prostate cancer patients. The solid lines represent the arc therapy plan, the dashed lines refer to the tomotherapy plan.

slightly enhanced for tomotherapy, whereas arc-therapy yields better results for the dose coverage. A comparison of the mean dose in the patient contour shows lower values for arc therapy. The integral dose, i.e. the sum of the dose values in all voxels, is 15% lower for AMCBT compared to tomotherapy.

The dose distribution in the sagittal slices shows a very steep dose gradient in the longitudinal direction for arc therapy, whereas for tomotherapy there is a relatively high dose in the normal tissue above and below the tumor. This phenomenon is caused by the helical delivery of tomotherapy. For arc therapy, the projection of the target determines the maximum size of the fluence field, and therefore the dose above and below the target decreases very rapidly. In helical tomotherapy the leaves of the binary MLC start to open as soon as the top of the target is in the field of view of the radiation source. Therefore a higher dose is also delivered to the normal tissue that is within the range of the MLC field width to the target.

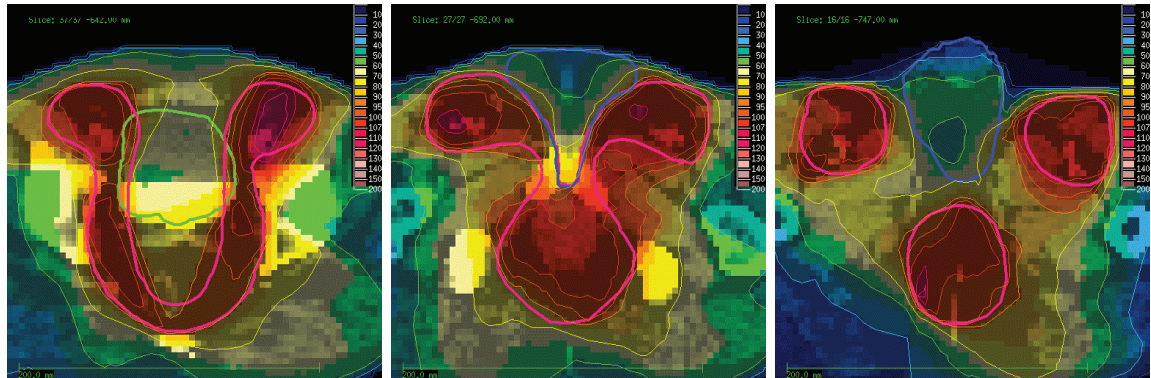
The delivery time for tomotherapy was 382s, 368s and 285s for patient 1, 2 and 3, respectively, with an average of 5.75 minutes. Since arc therapy was not performed, only an estimation of the treatment time is possible. This estimation depends on the hardware limitations, e.g. the gantry rotation speed, the velocity of the MLC leaves and the dose rate. For a maximum dose rate of 300 MU/min and a MLC leave velocity of 3 cm/s, we estimate a treatment time between 2 and 3 minutes for single rotation therapy. With higher dose rates the treatment time could be further reduced.

Anal carcinoma

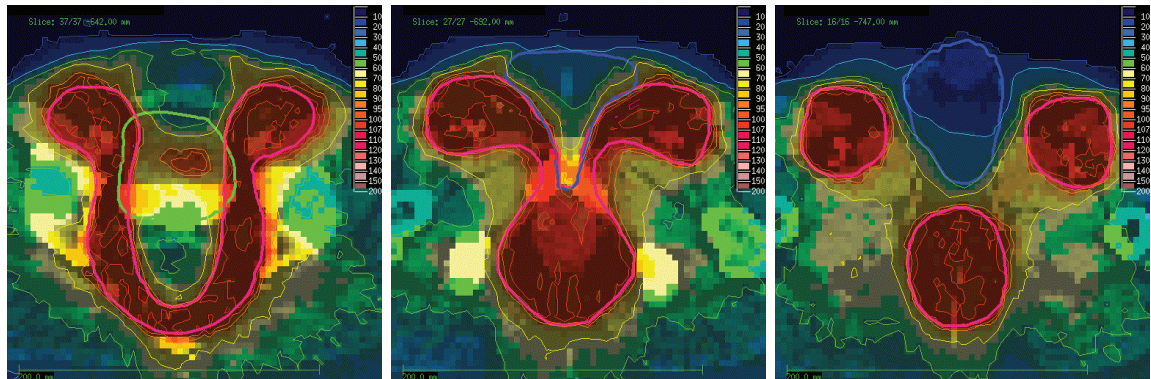
The group of patients with anal cancer is characterized as having very large target volumes (mean PTV volume = 1905 cm^3) and a high degree of concavity. Several transversal slices shown in figure 4.9 point out the high geometrical complexity for this class of cases.

In table 4.3 the averaged dosimetric parameters are listed for the three patients. For this patient group the dose distribution in the target is better for tomotherapy. The dose coverage of the PTV is higher for tomotherapy and also the conformity is slightly improved. In bladder and bowel the dose distributions of AMCBT and tomotherapy lead to similar mean doses. The mean dose to the genitals is slightly lower for tomotherapy, in the high dose region AMCBT delivers less dose. The mean dose to the patient contour is again lower for arc therapy.

The dose-volume histogram for patient 1 (figure 4.10) points out the better dose distribution in the PTV for tomotherapy. The dose distribution in figure 4.9 shows a good conformity to the tumor for both techniques. Even the separation of the target volume in several parts is very well possible with single arc therapy. The larger volume of the PTV compared to the prostate cases naturally leads to a longer treatment time for tomotherapy, on average the dose delivery takes 10 minutes. In arc-modulated cone beam therapy the treatment time depends on the rotation speed of the gantry. For the dose rate and MLC limitations stated previously the gantry rotation speed for these case will be approximately $140^\circ/\text{min}$ resulting in a treatment time of 2.5 minutes.



(a) Arc-modulated cone beam therapy



(b) Tomotherapy

Figure 4.9: Dose distribution in 3 transversal slices for patient 1 with anal cancer. The isodose line with 100% dose corresponds to 45 Gy. Displayed are the target (red), bladder (green) and genitals (blue).

organ	Tomo	AMCBT
PTV		
$D_{99\%}$	39.6	35.7
$D_{1\%}$	47.5	50.3
mean	45.0	45.0
coverage	0.97	0.82
conformity	0.88	0.86
Genitals		
$D_{1\%}$	45.6	42.1
mean	17.5	19.5
Bowel		
$D_{1\%}$	40.2	43.2
mean	6.7	6.7
Bladder		
$D_{1\%}$	46.7	44.9
mean	28.0	29.3
Integral dose	316.7	290.8

Table 4.3: Mean dose values for tomotherapy (Tomo) and AMCBT for three patients with anal cancer (dose values in Gy, integral dose in Gyl).

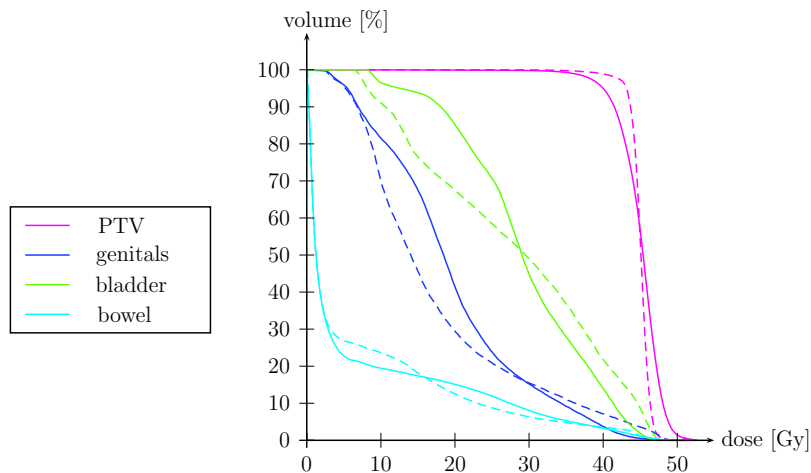
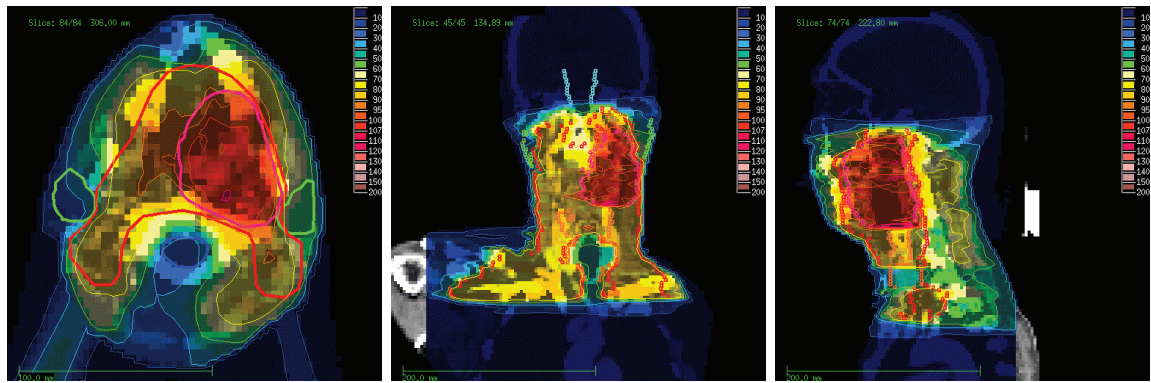


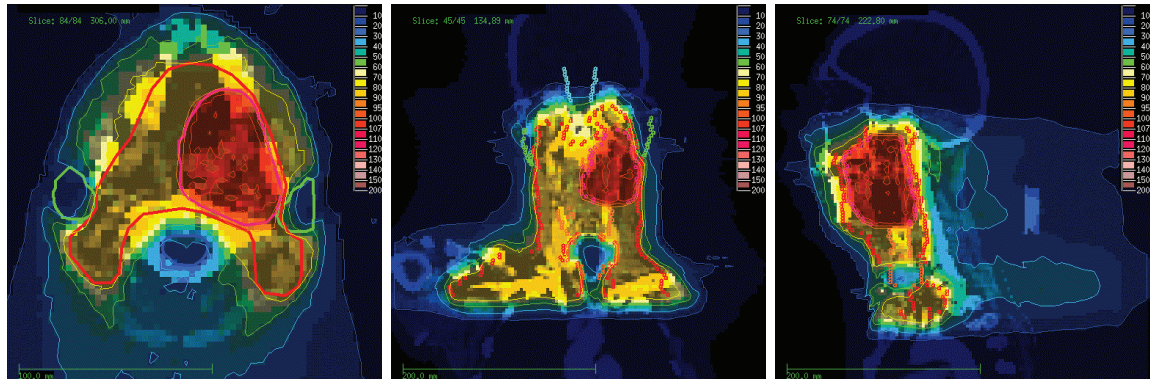
Figure 4.10: Mean dose volume histogram for three patients with anal carcinoma. The solid lines represent the treatment plan for AMCBT, the dashed lines refer to the tomotherapy plan.

Oropharynx carcinoma

For this group of patients with a tumor in the head and neck region two different dose levels were prescribed, 57.6 Gy in the PTV and 70.4 Gy in the boost region(s). The parameters derived from the dose-volume information are summarized in table 4.4. In the PTV the dose coverage and conformity are improved for tomotherapy. Also in the boost region the variation of the dose is higher for AMCBT. The dose sparing for most OARs is better possible with tomotherapy, especially the dose to the parotids, which are very close to a boost volume, is lower with this technique. With arc-therapy a very good sparing of the brain stem was possible. As seen for the other cases as well, the integral dose is lower for arc therapy compared to tomotherapy, for this patient group by 10%.



(a) Arc-modulated cone beam therapy



(b) Tomotherapy

Figure 4.11: Dose distribution for patient 1 with oropharynx cancer. The upper row represents arc-therapy, the lower row tomotherapy. The 100% isodose line equals 70.4 Gy. Displayed are the target (red), parotid glands (green), brain stem (light blue) and spinal cord (blue).

The DVH (figure 4.12) shows the better coverage of the PTV for tomotherapy, and also the lower dose to most OARs. In the transversal slice of the dose distribution (figure

organ	Tomo	AMCBT
Boost		
$D_{99\%}$	65.4	60.7
$D_{1\%}$	71.0	73.7
mean	68.9	68.3
PTV		
$D_{99\%}$	49.4	43.8
$D_{1\%}$	69.9	71.6
mean	57.6	57.6
coverage	0.81	0.69
conformity	0.94	0.88
Parotid glands		
$D_{1\%}$	54.2	51.0
mean	20.1	28.5
Brain stem		
$D_{1\%}$	24.7	29.5
mean	9.2	7.4
Spinal cord		
$D_{1\%}$	21.2	29.0
mean	12.0	14.5
Larynx		
$D_{1\%}$	59.1	61.4
mean	40.5	48.9
Trachea-esophagus		
$D_{1\%}$	47.4	52.0
mean	27.2	34.4
Integral dose	206.1	183.8

Table 4.4: Mean dose values for tomotherapy (Tomo) and AMCBT for three patients with oropharynx cancer (dose values in Gy, integral dose in Gyl).

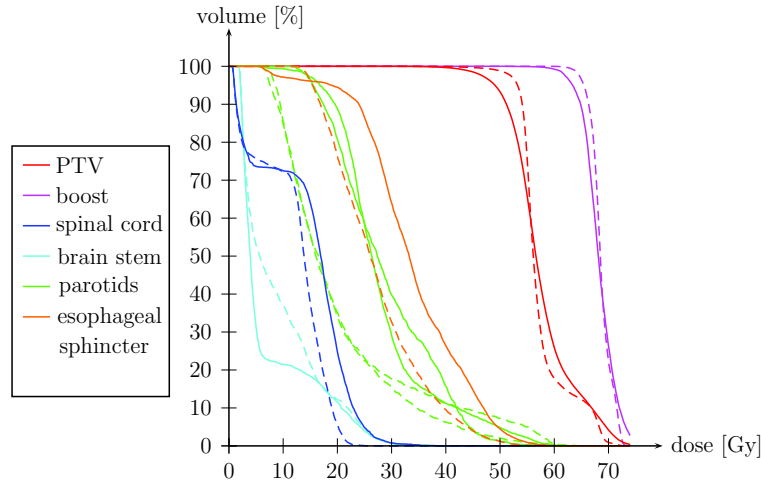


Figure 4.12: Mean dose volume histogram for three patients with oropharynx cancer. The solid lines represent the treatment plan for AMCBT, the dashed lines refer to the tomotherapy plan.

4.11) the position of the boost volume is shown and its close proximity to the parotid gland. With tomotherapy planning it was possible to spare this OAR very well from dose, but also with arc therapy a steep dose gradient between the boost volume and the left parotid gland is achievable. The sagittal view shows a better dose sparing of the neck with tomotherapy, but with tomotherapy the fall-off of the dose in longitudinal direction is not as steep as for arc-therapy.

4.3 Comparison of AMCBT and "idealized IMRT"

The comparison of AMCBT and helical tomotherapy in section 4.2 showed better dose shaping capabilities for helical tomotherapy for complex patient geometries. In this section it is examined how much the dose distributions for single arc therapy could be improved by adding additional arcs. Therefore, treatment plans with modulated fluence fields and the same number of beam directions as for AMCBT were created. The final dose distribution was calculated for the optimized fluence maps and no stratification and sequencing was performed. The dose delivery of such a treatment plan would take very long, but with an appropriate sequencing algorithm it would be possible to convert the modulated fluence fields in a set of deliverable aperture shapes. Therefore the dose distributions shown in this section represent the optimal solution for the respective dose constraints.

In the following section the treatment plans with a high number of beam directions and intensity-modulated fluence fields are referred to as "idealized IMRT" treatment plans. The dose constraints and penalty factors used for the optimization were the same as for AMCBT treatment plans. It should be noted that a comparison of "idealized IMRT" and

helical tomotherapy is not intended, since the dose constraints were chosen to find the best AMCBT treatment plan instead of the "idealized IMRT" treatment plan.

Prostate cancer

For the group of patients with a prostate carcinoma the differences in the dose distribution between AMCBT and helical tomotherapy were small. Table 4.13 displays the dose values for AMCBT and "idealized IMRT" for one example case. The corresponding dose volume histogram for AMCBT and "IMRT" is shown in figure 4.14. Differences in the dose distributions for the three different techniques are small. The higher dose in the rectum in the low dose region for "IMRT" is due to the dose constraint used for this OAR, which only penalizes dose values above 42 Gy. Besides the higher dose to the rectum, the dose values listed in table 4.13 are very similar for AMCBT and "IMRT". This indicates that a dose delivery in several rotations would not improve the quality of the dose distribution that is achievable within a single rotation.

organ	AMCBT	"IMRT"
GTV		
$D_{99\%}$	74.2	76.0
$D_{1\%}$	81.4	80.0
mean	78.0	78.0
CTV		
$D_{99\%}$	67.7	68.4
$D_{1\%}$	80.9	81.6
mean	75.2	75.3
PTV		
$D_{99\%}$	60.3	60.4
$D_{1\%}$	80.5	80.6
mean	72.3	72.4
Rectum		
$D_{1\%}$	70.1	72.4
mean	21.1	23.6
Bladder		
$D_{1\%}$	74.4	74.1
mean	26.3	26.2
Contour		
$D_{1\%}$	50.4	50.1
mean	4.7	4.7

Figure 4.13: Dose values for AMCBT and "ideal IMRT" for a patient with prostate cancer (values in Gy).

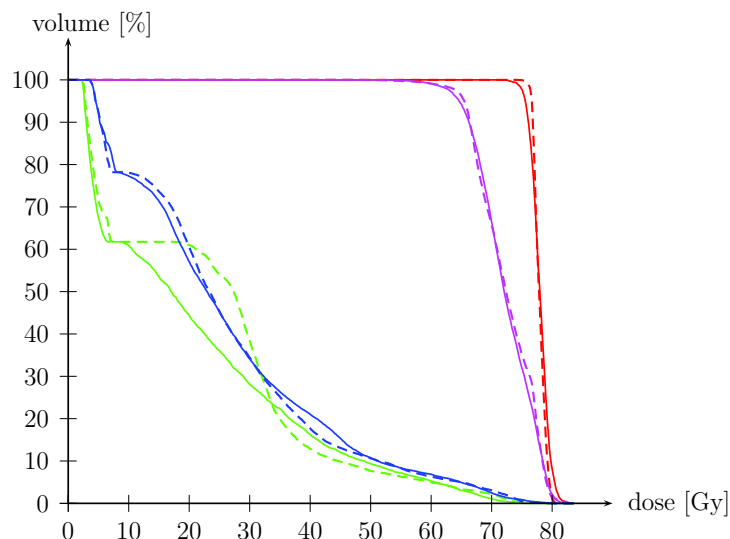


Figure 4.14: Dose volume histogram for a patient with prostate cancer. The solid line represents the dose distribution for AMCBT, the dashed line for "idealized IMRT".

Oropharynx cancer

The comparison of AMCBT and helical tomotherapy for oropharynx cancer patients showed a better dose distribution for helical tomotherapy. Table 4.5 summarizes the dose values for one example case for AMCBT, tomotherapy and "idealized IMRT". For the complex geometry present for oropharynx cancer it was possible to improve the dose distribution with intensity modulated fields compared to AMCBT. The dose to all OARs was reduced, in the target volume the dose coverage and conformity were improved. The integral dose for this treatment plan is not higher compared to the AMCBT treatment plan (203 Gyl for AMCBT, 204 Gyl for IMRT, 250 Gyl for tomotherapy).

organ	Tomo	AMCBT	"IMRT"
PTV			
$D_{99\%}$	49.0	45.5	50.8
$D_{1\%}$	71.6	69.7	70.9
mean	57.6	57.6	57.6
Boost			
$D_{99\%}$	67.6	63.1	66.2
$D_{1\%}$	72.8	71.7	73.7
Parotid glands			
$D_{1\%}$	53.0	52.7	50.3
mean	22.3	29.9	22.3
Brain stem			
$D_{1\%}$	20.9	28.7	17.8
mean	6.6	6.0	5.3
Spinal cord			
$D_{1\%}$	22.6	30.8	21.7
mean	12.3	15.5	12.9
Larynx			
$D_{1\%}$	58.4	58.2	58.9
mean	29.3	38.8	31.9
Trachea-esophagus			
$D_{1\%}$	39.7	43.7	37.5
mean	24.6	28.9	20.4
Lung			
$D_{1\%}$	42.9	54.6	45.9
mean	7.5	7.0	6.2
Contour			
$D_{1\%}$	59.8	62.7	60.4
mean	15.6	12.6	12.7

Table 4.5: Dose values for helical tomotherapy, AMCBT and "ideal IMRT" for a patient with oropharynx cancer (values in Gy).

For this patient a dose delivery in more than a single rotation would lead to an improved quality of the dose distribution. The question of how many arcs are needed to achieve the same quality as possible with helical tomotherapy is not answered with the comparison performed in this section. Another open issue is the treatment time needed for a dose delivery in several rotations.



(a) Constant fluence - AMCBT



(b) Modulated fluence - IMRT

Figure 4.15: *Comparison of the fluence distributions for intensity-modulated fields and AMCBT.*

Figure 4.15 shows examples of the fluence maps for AMCBT and IMRT for a few beam directions. The fluence maps are displayed for gantry angles of 194° , 201° , 208° and 215° . The different gray values symbolize a different number of MUs per field or bixel. For AMCBT the fluence within each field is constant, but the number of MUs varies between beam directions. For IMRT the field shape conforms to the beam's eye view of the target and within the field the fluence is modulated. The fluence maps for IMRT clearly show the much lower intensity in areas where the beam hits an OAR.

5 Stability of AMCBT treatment plan quality

The quality of treatment plans for radiotherapy is influenced by many factors. The stability of the treatment plan quality is investigated for several aspects that have an impact on the final dose distribution achievable with AMCBT. First, the influence of hardware limitations is examined in section (5.1). The next section (5.2) deals with the influence of different primary fluence profiles on the final dose distribution. For a variety of parameters, e.g. the MLC leaf width, the number of beam directions used for treatment planning or the collimator angle, the effect on the treatment plan is investigated (section 5.3). In the last section of this chapter the stability of the dose distribution for imposed dose delivery errors is examined (section 5.4).

5.1 Hardware limitations

To account for the limitations imposed by the dose delivery hardware the following constraints were included into the optimization: a minimum and maximum beam weight (depending on the dose rate of the linac), a maximum change of consecutive beam weights (depending on the achievable variation of the dose rate) and a maximum change of consecutive aperture shapes (depending on the speed of the MLC leaves). All these limitations depend on the gantry rotation speed, which is calculated based on the total number of MUs to be delivered and is assumed to be constant for one treatment. A detailed description how the constraints were included into the optimization concept was given in section 3.2.

For a Siemens ArtisteTM linac equipped with a 160MLCTM gantry speeds between $50^\circ/min$ and $360^\circ/min$ are possible and the dose rate can vary between $30 MU/min$ and $300 MU/min$ with a maximum variation rate of $20 MU/min$ per second. The maximum physically achievable leaf speed of the 160MLCTM is $4 cm/s$, but during the optimization it was set to $3 cm/s$. The restriction of the leaf speed to a value that is lower than the maximum speed offers the possibility to perform arc therapy together with tumor tracking.

In this section, treatment plans for AMCBT which were optimized with or without considering limitations imposed by the hardware are compared. To further examine the influence of the different hardware limitations on the quality of the dose distribution, treatment plans for which only a part of the limitations are considered were calculated. This was done for a total of four different tumor types. The treatment plan generated with an unconstrained optimization was defined as the optimal dose distribution for the respective case.

Results

The first case under investigation is a prostate cancer patient. Treatment planning was performed for 36 fixed beam directions. During the optimization loop the "optimal" gantry rotation speed was determined to be $120^\circ/\text{min}$. If the hardware limitations are not considered in the optimization, the dose rate varies between $0 \text{ MU}/\text{min}$ and $624 \text{ MU}/\text{min}$. Figure 5.1 shows the influence of the dose rate limitation on the number of MUs per beam direction. For the given gantry rotation speed and a dose rate between $30 \text{ MU}/\text{min}$ and $300 \text{ MU}/\text{min}$, the number of MUs per beam is limited between 2.5 MU and 25 MU , as visible for the green curve in figure 5.1. The red curve shows the number of MUs per beam for the treatment plan in which the maximum variation of the dose rate was also considered. Differences of the three curves are only visible for very low or high dose rates, for all other angles the number of MUs is very similar for the three different optimization runs.

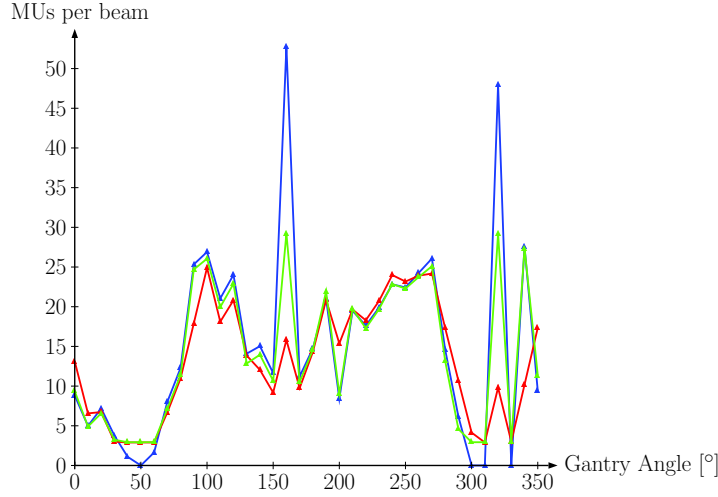


Figure 5.1: Number of monitor units per aperture for treatment plans optimized without considering hardware limitations (blue), considering a minimum and maximum dose rate (green) and considering also a maximum variation of the dose rate (red).

With a gantry rotation speed of $120^\circ/\text{min}$ the maximum distance the MLC leaves can move in a 10° interval is 15 cm . Figure 5.2 shows an example of the movement of three leaf pairs for a treatment plan that was generated without considering the limitations imposed by the hardware and a plan in which all hardware limitations were included. All leaf movements clearly stay within the limit of 15 cm . Small differences in the leaf movements between the treatment plans are presumably caused by the different beam weightings imposed by the dose rate limitations. Figure 5.2 shows the leaf pairs 44, 45 and 46 from a total of 80 leaf pairs, these leaf pairs are situated in the middle of the open field. None of the leaves exceeded the maximum movement of 15 cm , therefore limitations imposed by the MLC do not alter this treatment plan.

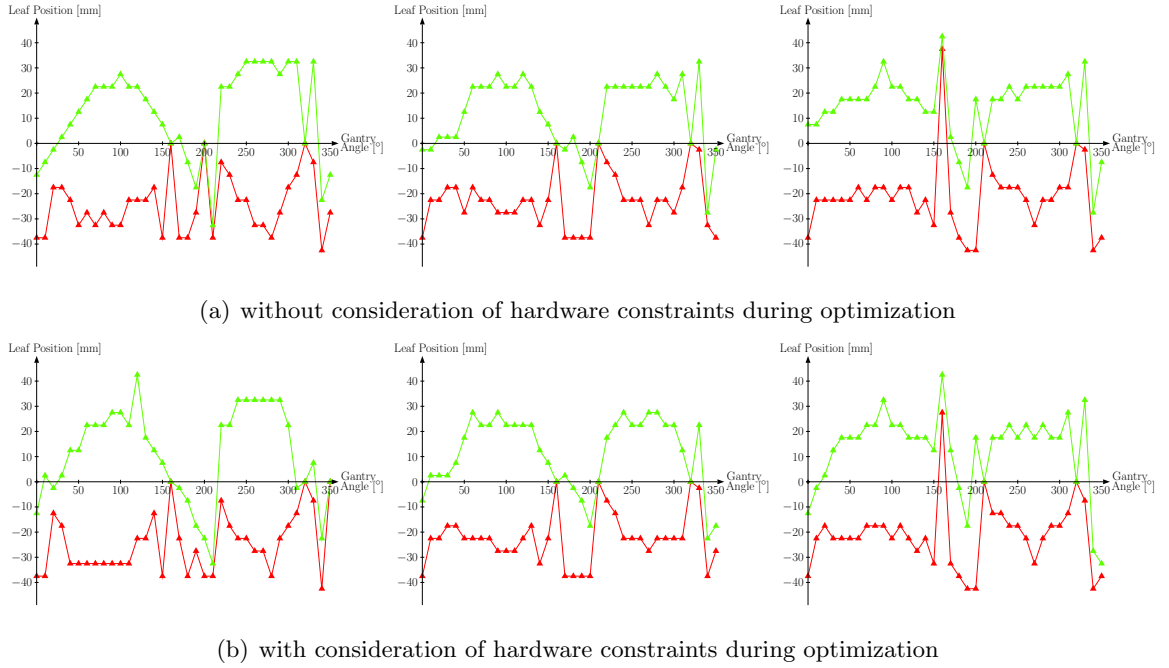


Figure 5.2: Example for the movement of three leaf pairs for the prostate cancer treatment plan. The movement of the right leaf is displayed in green, for the left leaf in red.

The dose distributions calculated for treatment plans that were optimized with and without considering hardware constraints during the optimization show almost no differences for this patient (see figure 5.4).

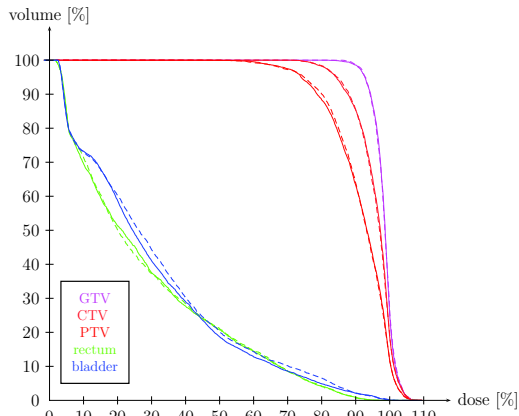


Figure 5.3: Dose volume histogram for treatment plans that were optimized without (solid line) and with (dashed line) consideration of limitations imposed by the dose delivery hardware.

For the second example under investigation - a meningioma - there are bigger differences in the number of MUs per beam direction (see figure 5.5). For this case the total number

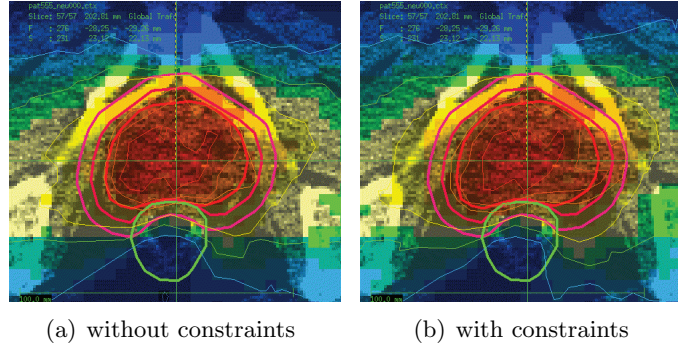


Figure 5.4: Influence of hardware constraints on the dose distribution for a prostate cancer case. Displayed are the PTV (pink), CTV (red), PTV (red) and rectum (green).

of monitor units is lower and therefore a faster rotation speed was calculated for dose delivery. For a gantry rotation speed of $214^\circ/\text{min}$ the number of MUs per 10° interval is limited between 1.4 MUs and 14 MUs. Without considering this limitation in the optimization the maximum number would exceed 28 MUs per beam, which corresponds to a dose rate of $600 \text{ MU}/\text{min}$.

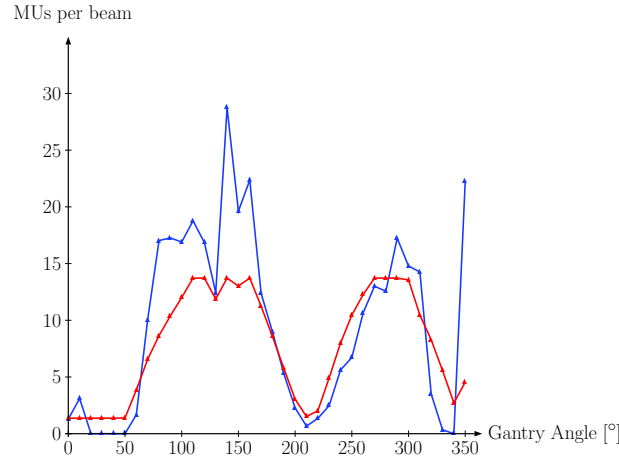


Figure 5.5: Influence of hardware limitations on the number of monitor units for a meningioma cancer patient. The blue curve represents a treatment plan that was optimized without constraints in the optimization, the red curve a treatment plan for which all hardware limitations were considered in the optimization.

For this example case the limitations imposed by the hardware lead to differences in the dose distribution. In the transversal slice of the dose distribution displayed in figure 5.7 the better sparing of the eyes and optical nerves for an unconstrained optimization is visible. Also the dose to other OARs is increased and the dose coverage of the target is decreased for the treatment plan that considers the dose rate limitations (see DVH in figure 5.6).

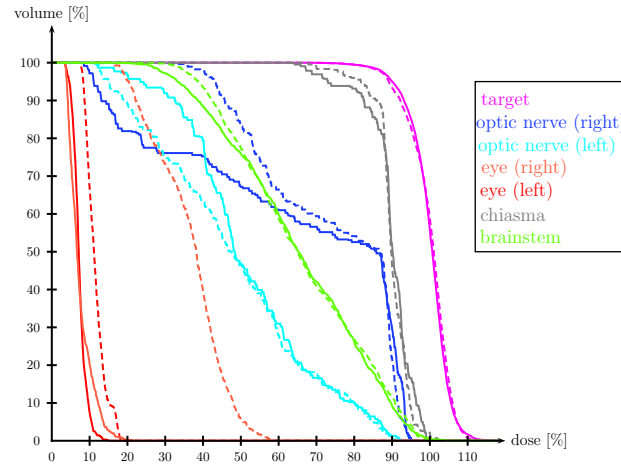


Figure 5.6: Dose volume histogram for a meningioma patient. The solid lines represent a treatment plan that was optimized without consideration of hardware limitations during the optimization, the dashed lines represent a treatment plan generated with consideration of limitations imposed by the hardware.

Even though the gantry rotation speed is faster for this example case, the inclusion of MLC limitations in the optimization did not lead to an increase in the final objective function value or differences in the dose distribution.

An investigation of the influence of hardware constraints on the objective function value for two more cases (head, pancreas) also showed increasing values for an optimization with hardware constraints. In table 5.1 the objective function values for the four cases for all optimization runs are summarized. All values were normalized to the objective function value for an optimization without hardware constraints.

	prostate	meningioma	head	pancreas
without constraints	1.00	1.00	1.00	1.00
with all constraints	1.01	1.43	1.22	1.19
only MLC constraints	1.00	1.01	1.13	1.01
only DR constraints	1.01	1.22	1.05	1.18
only min/max DR	1.00	1.11	1.05	1.14

Table 5.1: Objective function for optimization runs with different hardware limitations

In the current implementation of the optimization algorithm the gantry rotation speed is determined at the beginning of the optimization based on the expected number of MUs. For the meningioma case shown above, the influence of different gantry rotation speeds on the plan quality was examined. Both a faster and a slower rotation speed led to an

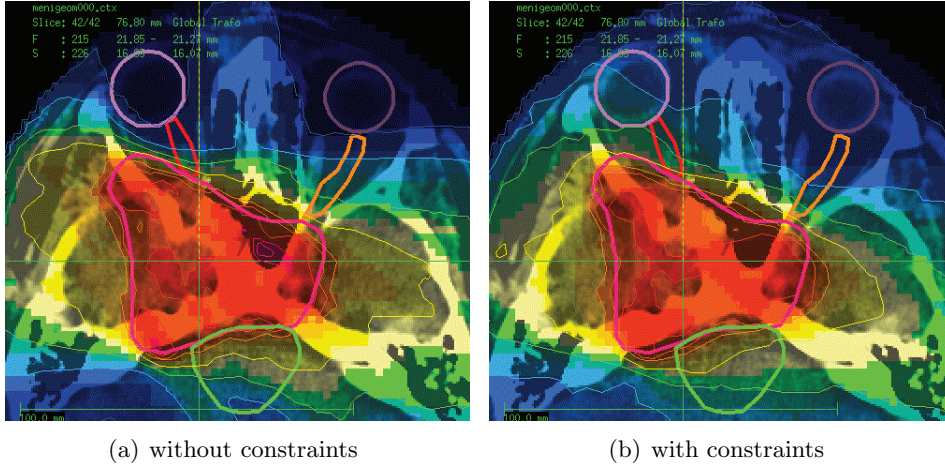


Figure 5.7: Dose distribution for a meningioma treatment plan optimized with and without hardware constraints. Displayed are the PTV in pink, the eyes in purple, the optical nerves in orange and red and the brainstem in green.

increase of the objective function value compared to the optimization run with $214^\circ/\text{min}$. With a rotation speed of $180^\circ/\text{min}$ or $280^\circ/\text{min}$ the final value of the objective function increases by approximately 10%.

5.2 Beam flattening filter

The basic idea of a beam flattening filter was explained in section 2.2. The advantage of a laterally flattened beam profile is an almost constant intensity throughout the radiation field. For conformal treatment techniques this results in a more homogenous dose distribution within the tumor. However, in IMRT there is the possibility to increase the weight of bixels at the edge of the radiation field and therefore a homogeneous dose distribution is also possible without flattening the beam profile. In this section the influence of different primary fluences on the quality of dose distributions for rotation therapy was examined. The advantage of removing the flattening filter is a higher dose rate and therefore potentially a shorter treatment time.

Beam profiles with and without the flattening filter were measured with a Siemens accelerator. Figure 5.8 shows the profiles for both situations for a 6 MV beam. Both curves were normalized to 1 at the center of field. The figure shows a much steeper off-axis dose decrease for the non-flattened beam. By removing the beam flattening filter the maximum dose rate of 300 MU/min could be increased to 1000 MU/min.

To investigate the treatment plan quality achievable with an unflattened beam profile treatment plans for both primary fluences were calculated. Hardware constraints, e.g. the MLC leaf speed or the dose rate limits, were not considered in the optimization. The same planning constraints and optimization concept were used for the optimization of treatment plans for both primary fluences.

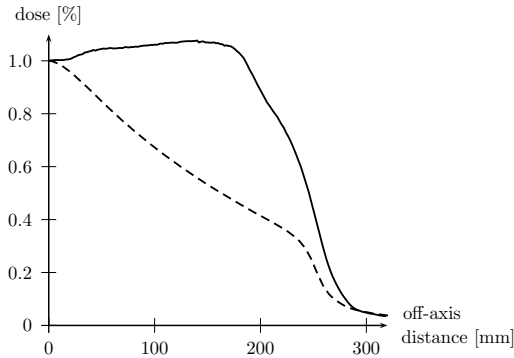


Figure 5.8: *Normalized primary fluences with (solid line) and without (dashed line) a flattening filter in the beam.*

Treatment plans were generated for three cancer types with different target sizes and geometries. The prostate cancer case had a relatively small target volume of 262 cm^3 which was prescribed a dose of 78 Gy in 35 fractions. For the anal cancer case the target structure was concave in shape with a volume of 1917 cm^3 and the genitals and bladder were in close proximity. The prescribed dose was 45 Gy in 25 fractions. The most complex geometry is represented by an oropharynx cancer case with two boost volumes within the PTV with dose levels of 56.4 Gy and 70.4 Gy for a dose delivery in 32 fractions.

Results

The final value of the objective function was approximately 10% worse if the flattening filter was not in the beam. Also increased is the total number of monitor units by 11%, 35% and 42% for prostate cancer, anal cancer and oropharynx cancer, respectively. Figure 5.9 shows the number of monitor units per beam for both treatment plans optimized for a prostate cancer case.

The dose distributions for the different primary fluences are similar in terms of target coverage, target conformity and OAR sparing for the prostate and anal cancer case. The final dose distribution is shown in figure 5.13 for the anal cancer patient. DVHs comparing both dose distributions for all cases are shown in figure 5.10, 5.11 and 5.12. The only case showing visible difference for the two beam profiles was the oropharynx cancer patient with an increased exposure to some OARs. Table 5.2 summarizes the results for the three patients. For all cases the mean dose to the patient contour is higher for the non-flattened beam profile.

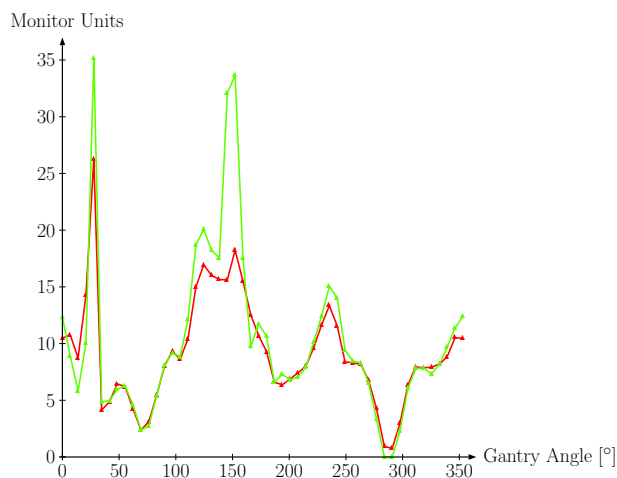


Figure 5.9: Number of monitor units per beam direction for a treatment plan optimized for a flattened beam profile (green) and a non-flattened beam (red).

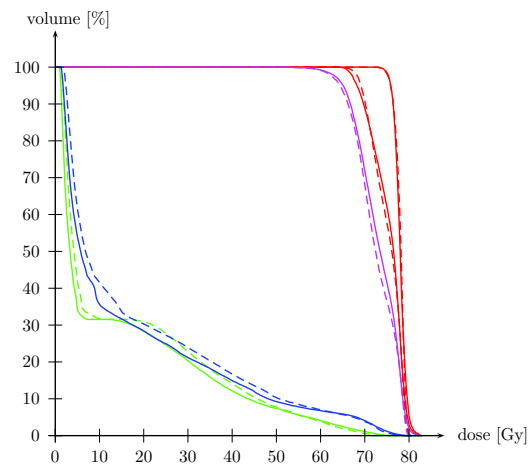


Figure 5.10: DVH for a treatment plan optimized with a flattened (solid lines) or non-flattened (dashed lines) beam profile for prostate cancer. The color code used for the VOIs in all DVHs in this section is the same as in section 4.2

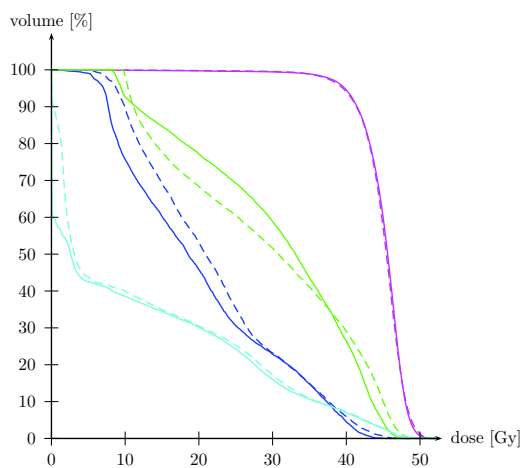


Figure 5.11: DVH for a treatment plan optimized with a flattened (solid lines) or non-flattened (dashed lines) beam profile for an anal cancer patient. The color code used for the VOIs in all DVHs in this section is the same as in section 4.2

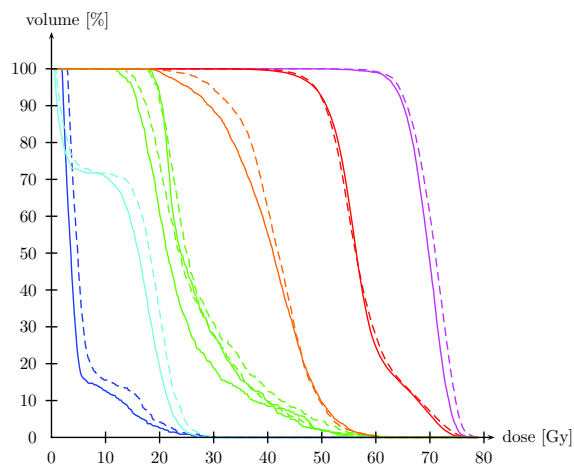


Figure 5.12: DVH for a treatment plan optimized with a flattened (solid lines) or non-flattened (dashed lines) beam profile for an oropharynx cancer patient. The color code used for the VOIs in all DVHs in this section is the same as in section 4.2

	prostate cancer		anal cancer		oropharynx cancer	
	flattened	non-flattened	flattened	non-flattened	flattened	non-flattened
PTV						
coverage	0.98	0.97	0.83	0.83	0.67	0.63
conformity	0.89	0.90	0.90	0.93	0.96	0.95
oar 1						
$D_{1\%}$	70.5	68.3	42.5	44.3	53.1	54.8
mean	13.9	15.1	20.3	22.1	25.8	27.5
oar 2						
$D_{1\%}$	75.4	74.3	46.3	47.6	23.5	25.4
mean	16.5	18.0	30.5	29.2	5.2	6.8
oar 3						
$D_{1\%}$			46.8	46.8	25.7	27.7
mean			11.8	12.6	13.3	15.0
contour						
mean	5.8	6.2	16.5	16.9	12.9	13.6
Monitor Units	479	534	450	606	483	687

Table 5.2: Comparison of treatment plans optimized with a flattened and non-flattened beam profile. OAR 1, 2 and 3 are rectum and bladder for prostate cancer, genitals, bladder and bowel for anal cancer and parotid glands, brain stem and spinal cord for oropharynx cancer, respectively. Dose values are in Gy.

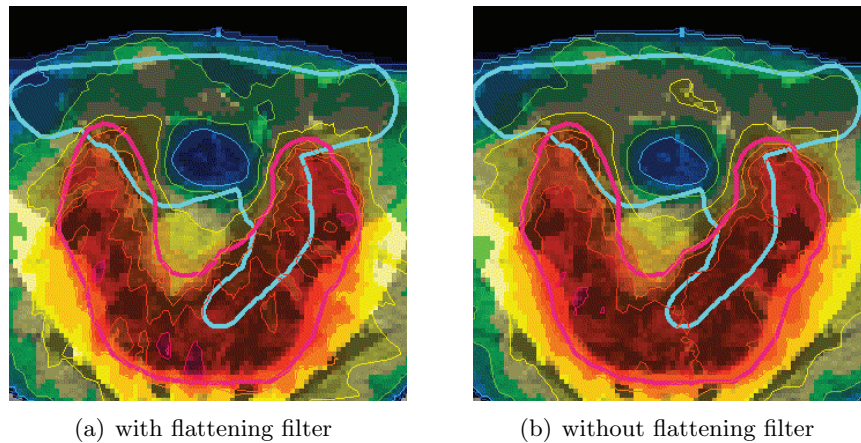


Figure 5.13: Dose distribution in a transversal slice for a flattened beam profile (left) and a non-flattened beam profile (right) for an anal cancer patient

5.3 Variation of optimization and delivery parameters

In this section the influence of a variety of parameters on the dose distributions is examined. The quality of an AMCBT treatment plan depends upon other terms on the parameters chosen for the optimization and on settings chosen for dose delivery. For a few of these parameters it was investigated how they influence the final dose distribution. In particular, the influence of the number of beam directions, the collimator angle, the leaf width, a constant dose rate and the rotational interval for dose delivery were studied.

Naturally the quality of the dose distribution improves with increasing number of iterations. Figure 5.15 shows the improvement of the objective function and the dose distribution during the direct aperture optimization. This chart starts after the gradient optimization of the field weights for the initial field shapes has finished, thus 0 iteration steps means the first iteration within the DAO part of the optimization. Therefore the first display of the dose distribution after 5 iterations shows the dose distribution that is achievable for the chosen initial field shapes if no direct aperture optimization would be performed. A comparison of the dose distributions after 5 and 1000 direct aperture optimization steps is shown in the dose volume histogram in figure 5.14. The much better target coverage together with a better sparing of the bladder is clearly visible within this DVH.

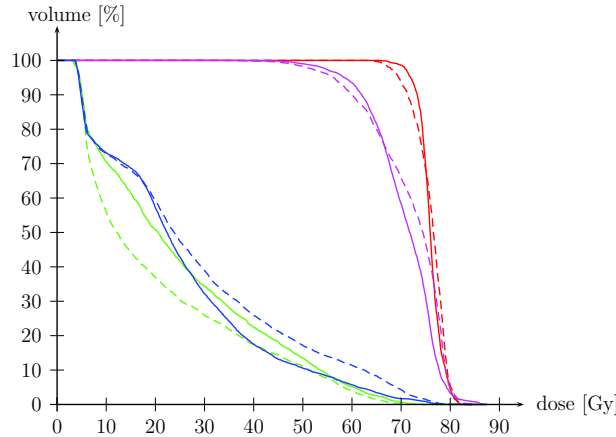


Figure 5.14: Dose volume histogram for treatment plans optimized in 1000 iteration steps (solid line) and 5 iteration steps (dashed line).

To get an impression of typical treatment fields for an AMCBT treatment figure 5.16 displays the fluence maps for a prostate cancer patient. Beside the shape of the field the weight is displayed by different shades of gray. The beam's eye view of the patient geometry is shown for gantry angles of 45° , 135° , 225° and 315° . This treatment was optimized without the consideration of hardware limitations during the optimization. The treatment fields at 50° , 300° and 310° are not displayed because their weight was 0.

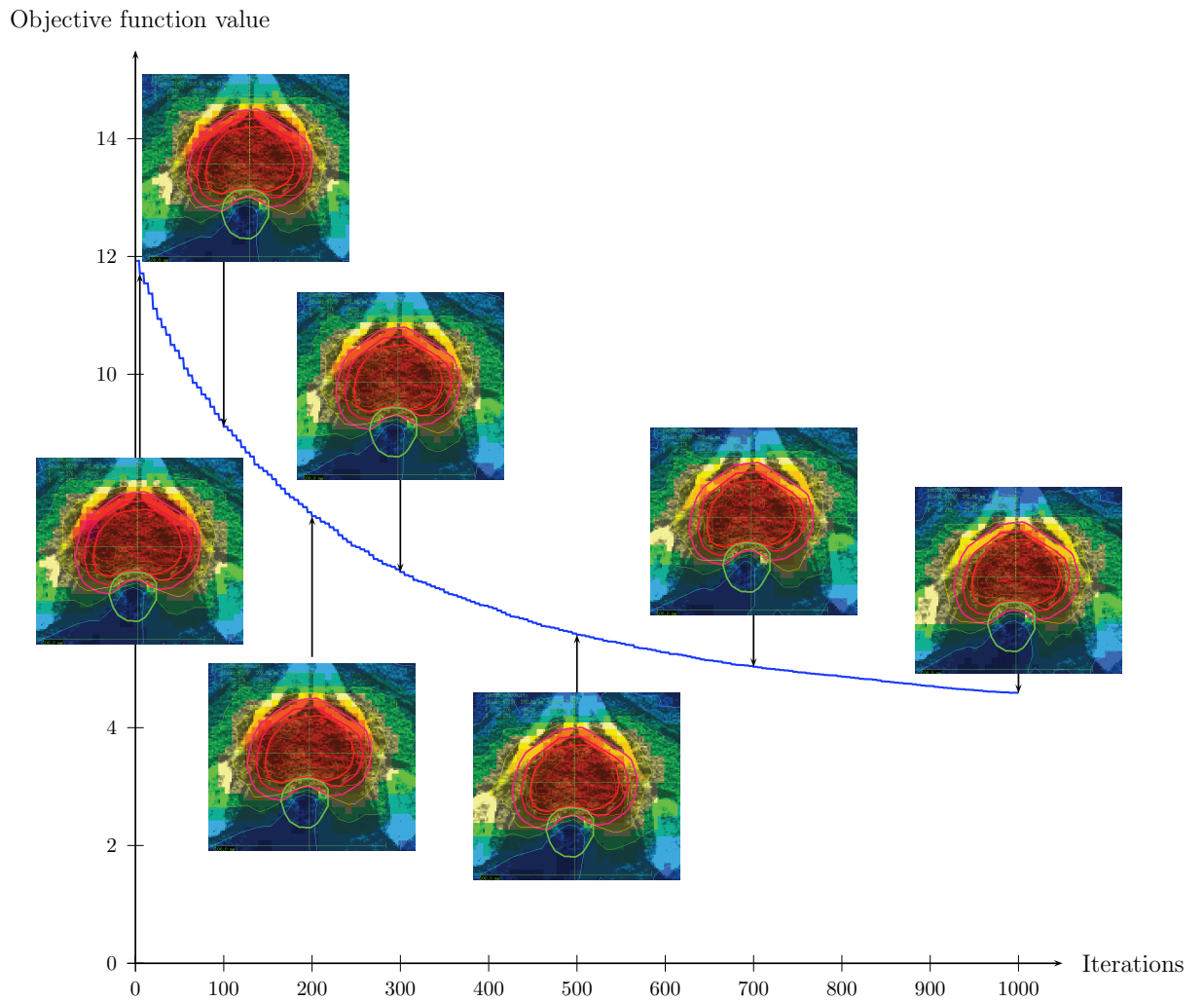


Figure 5.15: Progression of the objective function and the quality of dose distributions during the direct aperture optimization. Displayed VOIs are the PTV (pink), CTV (red), PTV (red) and rectum (green).

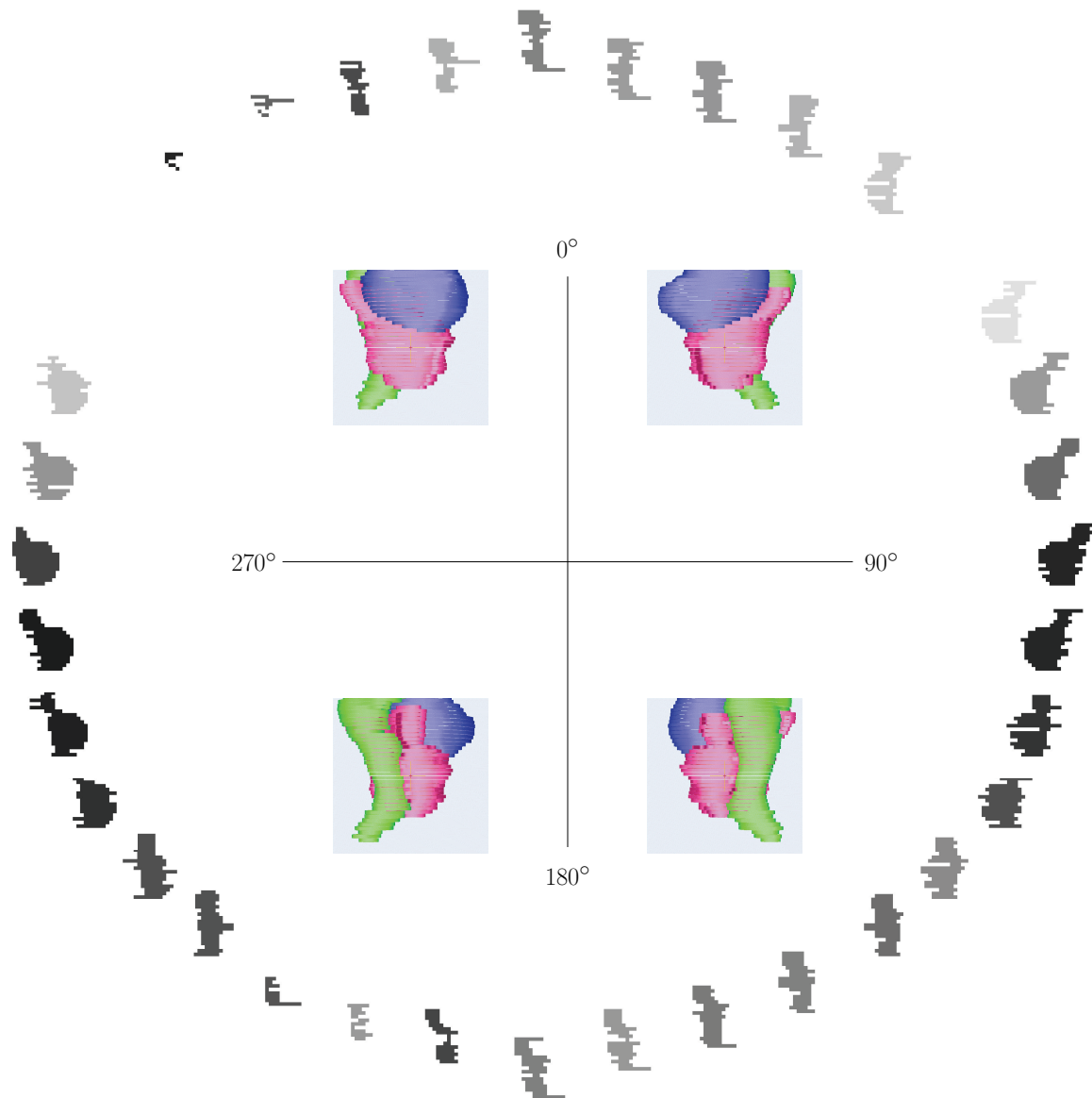


Figure 5.16: Treatment fields for AMCBT for a prostate cancer patient. The beam's eye view is shown for gantry angles of 45° , 135° , 225° and 315° . The target is displayed in pink, the rectum in green and the bladder in blue.

5.3.1 Number of beam directions

The number of beams used for treatment planning influences the results of the dose optimization. With a small number of beam directions the sampling of the continuous rotational delivery is poor and the number of DOF for optimization is low. On the other hand treatment planning with a small number of beam directions is very fast and limitations that are imposed by the delivery hardware do not restrict treatment planning if the angular distance between beam directions is large. With a high number of beam directions treatment planning becomes much slower and the limitations imposed by the delivery hardware become more severe. Moreover the treatment planning hardware needs a high memory capacity to store the dose information for a large number of beams.

Most plans shown in this thesis were optimized with 36 or 51 beam directions. For one example it will be shown that 36 beams are sufficient to explore the full advantage of dynamic rotational therapy and that the sampling rate is sufficient to reproduce the dynamic delivery.

Treatment plans with different numbers of beam directions were optimized for a prostate cancer patient. The dose constraints and penalty factors were the same for all treatment plans, but the number of iterations was increased for the optimization with 72 beam directions due to the larger number of DOF.

A comparison of treatment plans optimized with 18, 36 and 72 beam directions is shown in figure 5.17. The reduction to 18 beam directions resulted in a worse coverage of the target and a higher amount of dose to the rectum. For treatment plans optimized with 36 and 72 beam directions there are no visible differences for this patient anatomy.

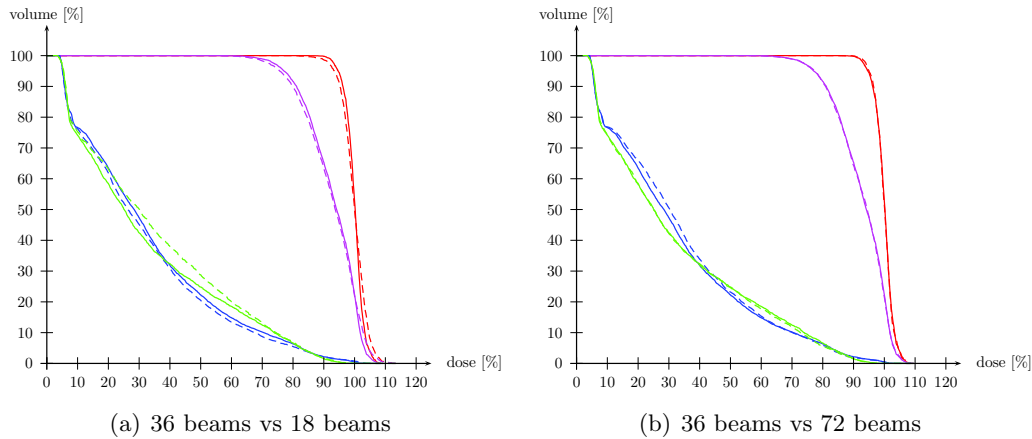


Figure 5.17: Dose volume histogram for treatment plans optimized with 18, 36 or 72 beam directions. Displayed are the GTV (red), PTV (pink), rectum (green) and bladder (blue). The solid line represents the treatment plan which was optimized with 36 beam directions.

This example shows that increasing the number of beam directions for treatment planning to 72 does not improve the quality of the dose distribution. Still, 36 beam directions might not be sufficient to be consistent with the continuously delivered dose distribution. The dose will be delivered while the gantry rotates and therefore the fixed beam directions

used for planning will be smeared over 10° intervals (for the 36 beam plan). For a better approximation of the dynamic delivery the field shapes and weights that were optimized for 36 beams are interpolated to 360 beams. For this case there was no difference between the DVHs for 36 and 360 beam directions.

For most beam directions the interpolation of MLC leaf positions is done linearly. If the leaves have to move across an OAR this would lead to an increased dose to this OAR. To reduce the dose to the OAR, all leaf pairs are closed before they move across the OAR. The maximum leaf speed was considered in this step. An example showing this effect is presented in figure 5.18 for a paraspinal tumor. At a gantry angle of 230° the open field is on the left side of the target in the beam's eye view. The next open field at 240° is on the right side of the target. If the leaf positions are linearly interpolated, the open radiation field would irradiate the spinal cord instead of the target. This leads to an increased dose to the spinal cord, as shown in the DVH. If the leaves are closed before they move across the OAR the differences in the DVH are much smaller. There is a slight decrease of dose coverage in the target volume, but the dose to the spinal cord is even lower compared to the original treatment plan.

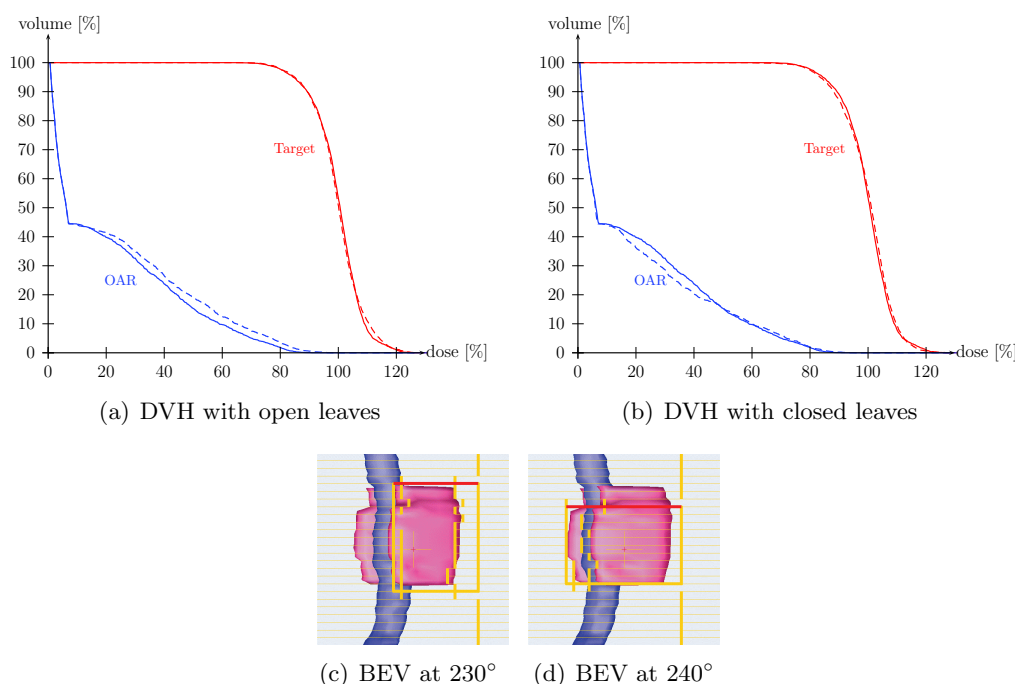


Figure 5.18: Effect of closing the leaves while they have to cross an OAR during dose delivery. The solid line represents the original treatment plan optimized with 36 beam directions, the dashed line the treatment plan that was interpolated to 360 beam directions.

5.3.2 Collimator angle

For AMCBT a constant collimator angle is assumed during dose delivery, but each treatment could be performed with a different collimator angle. By rotating the collimator the direction of leaf movement could be changed.

Currently there is no optimization of the collimator angle included in the optimization concept. To consider different collimator angles during the treatment plan optimization it would be necessary to calculate an influence matrix for each collimator angle, which would be too slow and too memory intensive. That the collimator angle has an effect on the final dose distribution is shown in figure 5.21.

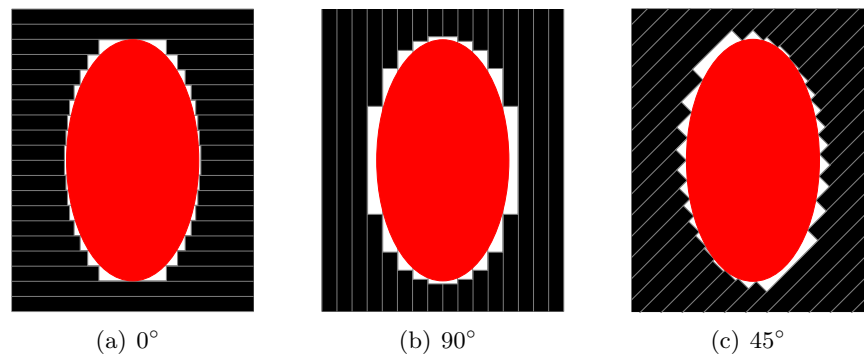


Figure 5.19: Schematic illustration of target conformal leaf positions for different collimator angles.

There are several aspects that have an influence on the choice of the optimal collimator angle. By rotating the collimator the number of open leaf pairs and therefore the number of degrees of freedom available for planning might vary, as pointed out in the schematic illustration of a tumor and MLC leaves for different collimator angles (see figure 5.19). For this elliptical shaped target geometry the number of open leaf pairs for a collimator angle of 0° is higher compared to a collimator angle of 90° . Another aspect is the matching of the leaves to the target volume and therefore the amount of normal tissue that is unnecessary irradiated to high doses. As visible in figure 5.19 there is much more unnecessary irradiated tissue for a collimator angle of 90° compared to 0° . Other aspects that might have an influence on the final dose distribution but were not yet investigated are interleaf leakage or the tongue and groove effect.

A promising approach to determine the collimator angle was to calculate the number of open leaf pairs for each collimator angle and to define the "optimal" collimator angle as the one with the highest number of open leaves. Based on the contoured volumes for the respective case an algorithm calculates the initial field shapes for all gantry angles and counts the number of open leaf pairs for each collimator angle in steps of 10° . In figure 5.22 the mean number of open leaf pairs per beam direction is displayed as a function of the collimator angle. As expected, by rotating the collimator for 180° the number of open leaf pairs is approximately the same.

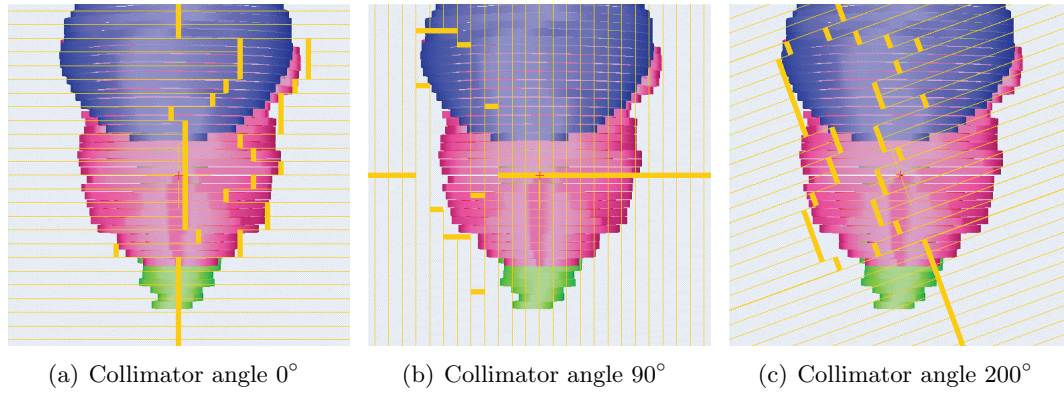


Figure 5.20: Beam's eye view at 0° gantry angle showing the MLC leaf positions after optimization for different collimator angles.

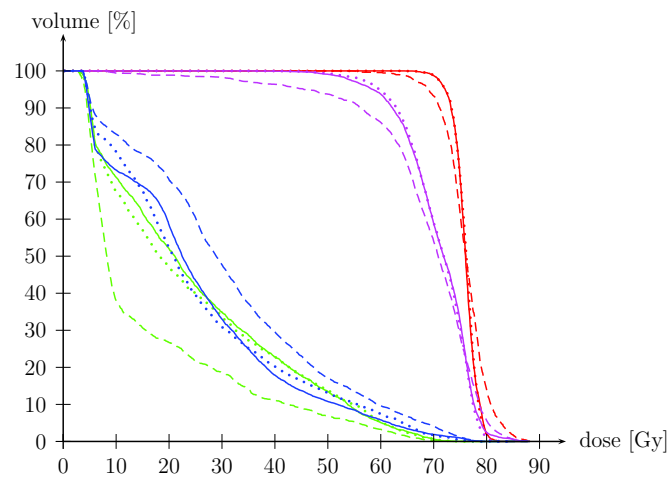


Figure 5.21: DVH for different collimator angles. The solid line represents a collimator angle of 0° , the dashed line 90° and the dotted line the "optimal" collimator angle of 200° .

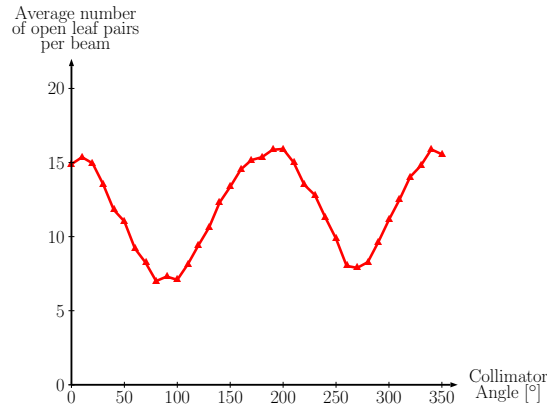


Figure 5.22: Average number of open leaf pairs per beam direction for different collimator angles.

For the prostate patient the "optimal" collimator angle is 200° with on average 15.9 open leaf pairs per beam direction. But for this case the number of open leaf pairs for a collimator angle of 0° is almost the same and both collimator angles lead to the same dose distribution. The beam's eye view for different collimator angles in figure 5.20 shows that for a collimator angle of 90° the number of open leaf pairs is much lower compared to a collimator angle of 0° or 200° . Treatment planning with a collimator angle of 90° leads to a worse dose distribution, as shown in the DVH in figure 5.21.

Even though the approach to calculate the collimator angle based on the number of open leaf pairs is not very sophisticated, it can help to find a good collimator angle. Most plans in this work were optimized with a collimator angle of 0° .

5.3.3 MLC leaf width

The MLC leaf width determines the size of the bixels used for treatment planning. KonRad works with square bixels, where the bixel size corresponds to the MLC leaf width. The current planning approach with a precalculated influence matrix storing dose contributions for all bixels has the disadvantage that a dose calculation is only possible for field shapes that are made up of a multiple of the bixel size. Therefore, all field shape changes are at least one bixel in size even though in leaf movement direction smaller steps might lead to better dose distributions.

Treatment plans were calculated for $(2.75 \text{ mm})^2$, $(5 \text{ mm})^2$ and $(10 \text{ mm})^2$ bixels. For the generation of the initial field shapes the number of bixels overlapping with the projection of the most important OAR increases with decreasing bixel size. The initial field shapes for 10 mm, 5 mm and 2.75 mm bixels consists of the bixel sets $A_k^{(2+)}$, $A_k^{(2++)}$ and $A_k^{(2++++)}$, respectively. Figure 5.23 shows the DVHs for all three treatment plans. For a similar dose distribution in the target the dose to the OARs increases with increasing bixel size, e.g. the mean dose in the rectum is 24.7 Gy, 25.1 Gy and 30.1 Gy. The final value of the objective function for the different bixel sizes was 39036, 43026 and 54498 for $2.75 \times 2.75 \text{ mm}^2$,

$5 * 5\text{mm}^2$ and $10 * 10\text{mm}^2$ bixels, respectively.

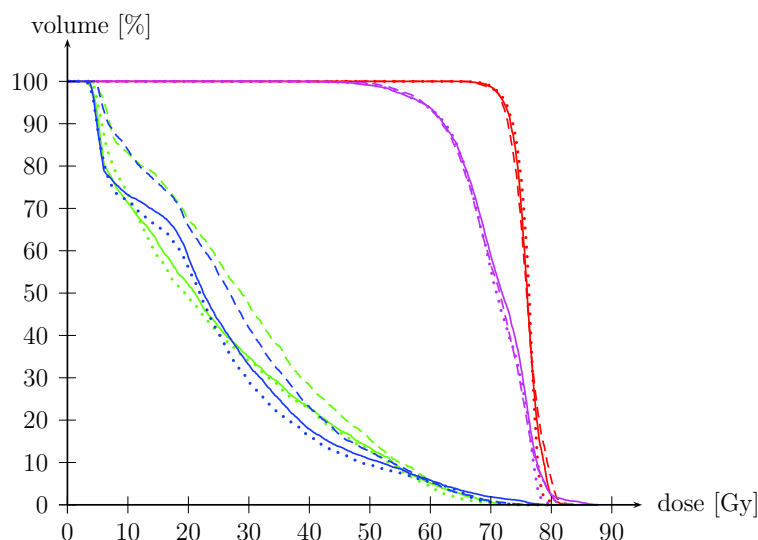


Figure 5.23: DVH for different bixel sizes. The solid line represents the dose distribution calculated with $(5\text{ mm})^2$ bixels, the dashed line $(10\text{ mm})^2$ and the dotted line $(2.75\text{ mm})^2$. Displayed are the GTV (red), PTV (pink), rectum (green) and bladder (blue).

5.3.4 Constant dose rate

In AMCBT the dose rate can vary within a specified range during dose delivery. To perform AMCBT the ability to vary the dose rate or gantry rotation speed of the linac during dose delivery is required. In this section it is investigated by how much the quality of dose distributions decreases if the dose rate is kept constant for the complete treatment. To generate treatment plans with a constant dose rate, i.e. the same field weight for each beam direction, the projection in the optimization algorithm was modified. Instead of assigning an individual weight to each field shape, the mean weight of all field shapes is calculated and the same value is assigned to all field shapes. Therefore the weight is not kept constant during the optimization process, but it is kept constant for all beam directions.

For some cases, e.g. the prostate cancer patient that was considered in the last sections, a constant dose rate does not lead to a degradation of the treatment plan quality. For this example case the dose coverage and conformity of the target volume and also the dose to OARs were almost the same for the treatment plans that were optimized with constant and variable dose rate.

In figure 5.24(a) the influence of removing the degree of freedom to vary the dose rate during dose delivery on the dose distribution for another prostate cancer case is shown. The dose coverage of the target volume is worse if no variation of the dose rate is allowed and the dose to the bladder is higher. The dose that is delivered to the rectum is lower for the constant dose rate.

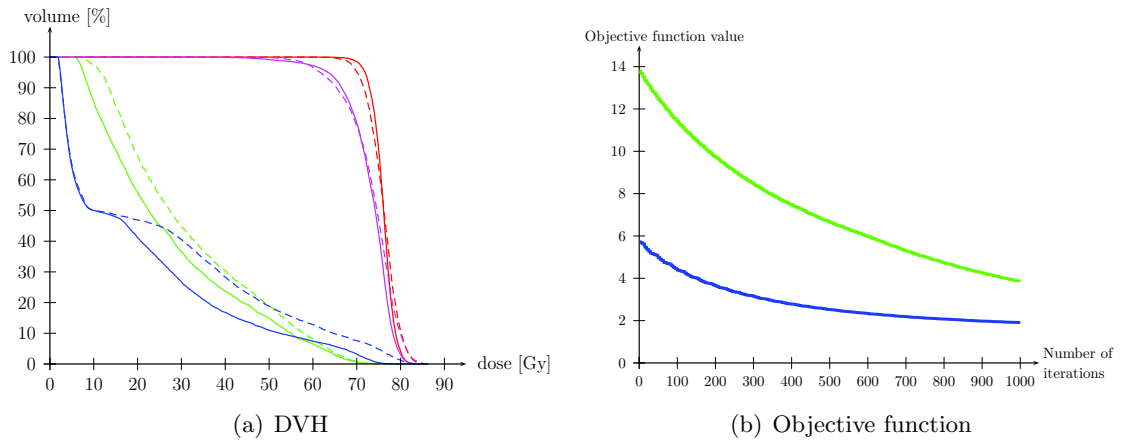


Figure 5.24: Comparison of treatment planning with constant or variable dose rate for a prostate cancer patient. In the DVH the dose distribution that was optimized with variable field weights is represented by the solid lines, the one optimized with constant dose rate is represented with dashed lines. The green curve shows the progression of the objective function for a constant dose rate, the blue one for variable dose rate.

The difference between the dose distribution and the prescribed dose values is measured with the objective function. Figure 5.24(b) shows the progression of the objective function for the optimization with variable and constant dose rate. This chart starts after the first stopping criteria in the optimization loop for AMCBT was fulfilled, thus after the field weights for the initial field shapes were optimized. This explains why the objective function at the beginning of this chart is much higher for the treatment plan with constant dose rate. By varying the field shapes it is possible to improve the dose distribution achievable with constant dose rate, but still with variable dose rate the objective function is lower.

5.4 Sensitivity of rotational therapy to dose delivery errors

The calculation of the dose distribution is based on a treatment plan that defines MLC leave positions and a number of MUs for each beam direction. For a dose delivery with fixed gantry angles the measured dose distribution will agree with the calculated distribution if all leaves are positioned correctly and the correct number of MUs is delivered per beam. Also for a dynamic dose delivery the measured and calculated dose distributions are expected to agree with each other. In this section the influence of several errors that could occur during dose delivery on the dose distribution is investigated for a prostate cancer patient. This analysis was also performed for other geometries with similar results.

5.4.1 MLC

The first possible source for dose delivery errors under investigation is the multileaf collimator. Leaves might be displaced systematically, e.g. all leaves are shifted in the same

direction, or randomly, e.g. all leaves are displaced for different distances and in different directions.

The influence of a systematic leaf shift on the dose distribution was tested for 1 mm, 2 mm and 3 mm leaf displacements for several clinical cases. For random shifts leaf displacements up to 5 mm were tested. In figure 5.25 a systematic and a random leaf displacement for 3 mm are shown in the beam's eye view. For random errors the leaf displacement was either the same distance for each leaf, as shown in figure 5.25(d), or all leaves were displaced randomly by distances between minus and plus the maximum displacement value. The influence of leaf displacements on the dose distribution is displayed in figure 5.26. For random shifts the imposed error on the dose distribution is small. Even for displacements between -5 mm and +5 mm there were only minor differences in the DVHs. For systematic leaf displacements there are much bigger differences in the dose distribution. Even for a leaf displacement of 1 mm there are small differences in the DVHs. For a leaf displacement of 3 mm the differences are clearly visible in the DVH. For both a leaf shift to the left and to the right side the coverage of the target decreases. For the initial field shapes used for this optimization the loss of dose coverage in the target is more pronounced for a shift to the right side, whereas a shift of the leaves to the left increases the dose to the rectum.

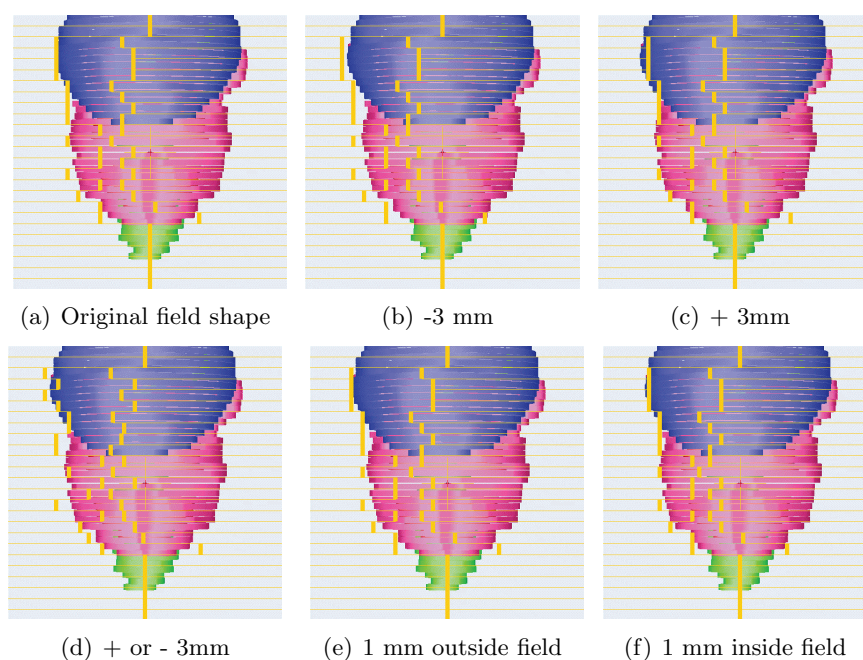


Figure 5.25: *leaf displacements in the beam's eye view.*

The size of the field was not changed in the last examples. If the field shape gets broader or more narrow there is an effect on the dose distribution even for small displacements. The DVH in figure 5.26(d) shows the influence on the dose distribution if all leaves are shifted by 1 mm outside of the field, i.e. the left leaves move to the left and the right

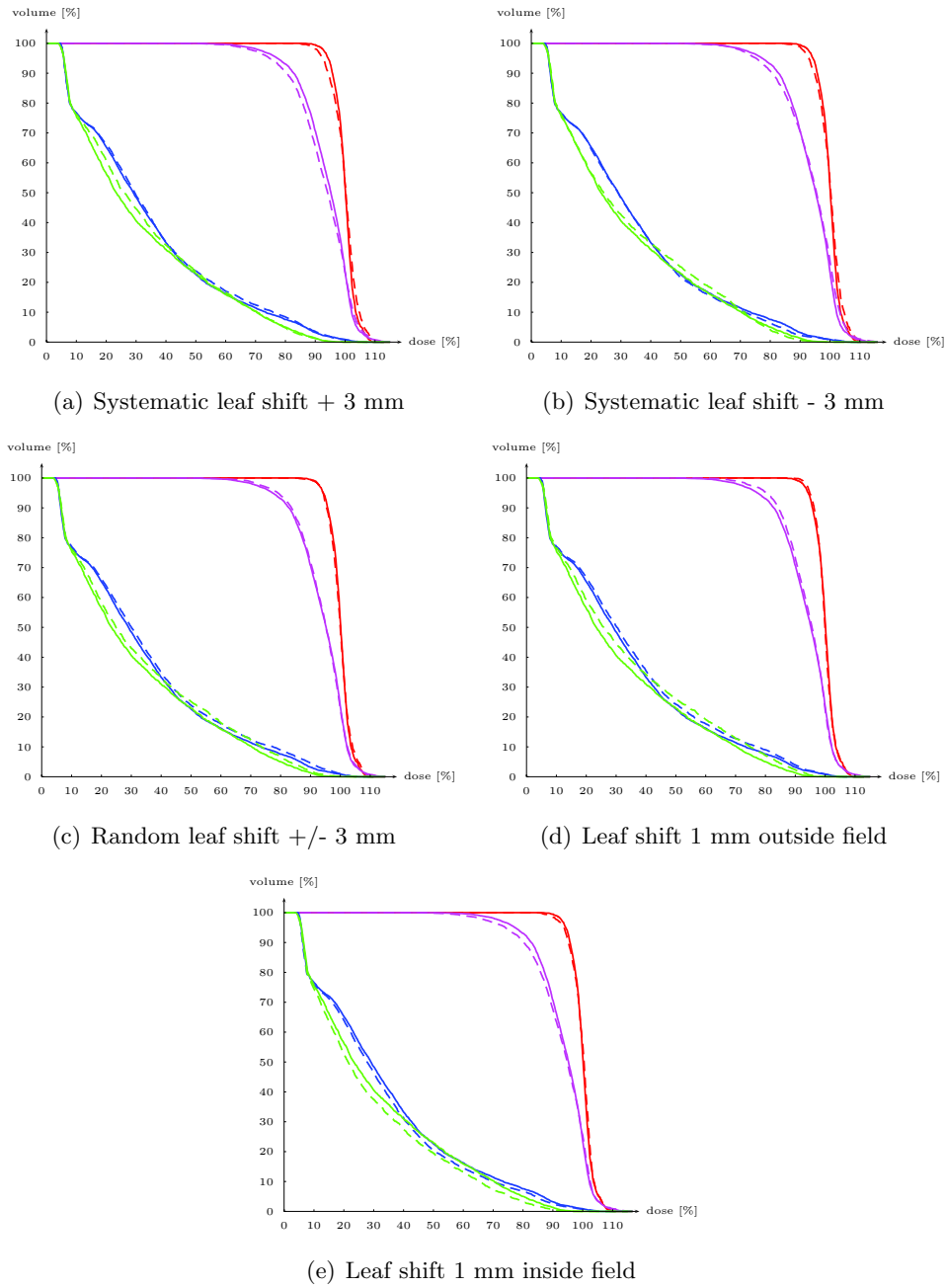


Figure 5.26: Influence of systematic and random leaf displacements on the dose distribution. The solid lines represent the original plan, the dashed lines the treatment plans with displaced leaves. Displayed are the GTV (red), PTV (pink), rectum (green) and bladder (blue).

leaves to the right. In this case the dose to the target volume and the adjacent OARs increases, e.g. the mean dose to the rectum increases from 23.8 Gy to 25.6 Gy.

For other clinical cases the results were the same - a systematic shift to one side results in a worse dose distribution and randomly shifting the leaves for up to 3 mm has only a small effect on the dose distribution.

5.4.2 Dose rate

In this section the effect of dose rate errors during dose delivery are examined. To generate treatment plans with a dose rate that differs from the original treatment plan the number of monitor units per beam was changed. The dose rate [MU/min] is calculated according to:

$$DR = \text{Number of MUs per beam} * \frac{v_{\text{Gantry}}}{\Delta\varphi}$$

with $\Delta\varphi$ as the angular interval between two beams.

At first the dose rate was increased or decreased for the complete treatment by approximately 1%. A comparison of the DVHs for the original treatment plan with 476 MU and a treatment plan with 481 MU is shown in figure 5.27(a). The increase in the number of MUs per beam is 0.14 MU, resulting in an dose rate increase of 1.6 MU/min for a gantry rotation speed of 120 $^\circ/min$.

An increased dose rate leads to additional dose in all VOIs, e.g. the mean dose that is delivered to the GTV increases from 76 Gy to 76.8 Gy and the dose to the rectum from 23.8 Gy to 24 Gy. Moreover, the dose coverage of the target volume increases, but the conformity of the dose distribution decreases. The integral dose that is delivered to the patient increases from 127.5 Gyl to 128.8 Gyl.

As a result, a systematic dose rate error of 1% would lead to visible differences in the DVH, but might not be detected in dose measurements. To account for setup errors and other uncertainties in a dose measurement typically deviations between the measured and calculated dose of up to 3% are tolerated.

In figure 5.27(a) a DVH for a treatment plan with an increased dose rate of 5% is shown. The number of monitor units for this plan adds up to 500 MU. In this case the mean dose to the GTV is increased to 80 Gy and the dose that is delivered to the rectum is 25 Gy. For the next test the number of monitor units was increased for low dose rates and decreased for high dose rates, as shown in figure 5.28. The total number of monitor units is the same for both treatment plans. The dose rate is changed by up to 23 MU/min . The influence of this dose rate error on the dose distribution is shown in figure 5.27(c).

The integral dose for the modified treatment plan is slightly lower with 126.3 Gyl compared to 127.5 Gyl. In some VOIs the dose is slightly increased for the treatment plan with imposed dose rate errors, e.g. the mean dose that is delivered to the bladder increases from 25.8 Gy to 26.3 Gy. Other VOIs receive a lower dose with the modified treatment plan, e.g. the mean dose to the rectum is decreased from 23.8 Gy to 23.4 Gy. Overall, differences between both treatment plans are small for dose rate errors of up to 23 MU/min at maximum.

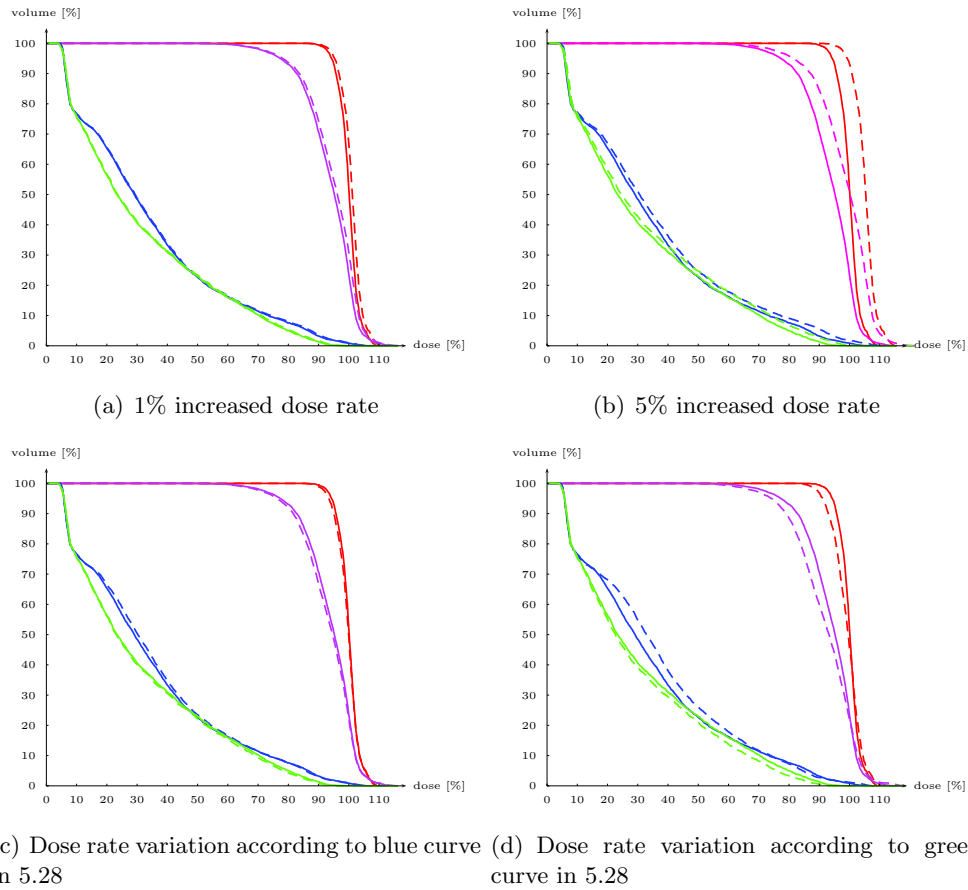


Figure 5.27: Dose volume histograms for treatment plans with imposed errors in the dose rate. The original dose distribution is displayed with solid lines, the modified with dashed lines. Displayed are the GTV (red), PTV (pink), rectum (green) and bladder (blue).

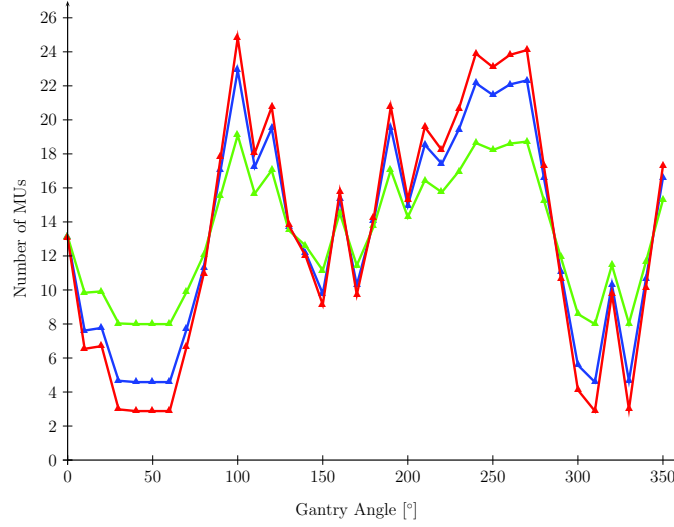


Figure 5.28: Number of Monitor Units per beam for the original treatment plan (red curve) and the modified plans (blue and green curve).

Another treatment plan with dose rate errors of up to 68 MU/min was generated and the resulting dose volume histogram is displayed in figure 5.27(d). The number of monitor units per beam in comparison to the original treatment plan is shown with the green curve in figure 5.28. In this case the integral dose is reduced to 124 Gyl and the dose coverage of the target volume decreases from 0.86 to 0.77. Most VOIs receive less dose with the modified treatment plan, only in the bladder the dose is increased to 27.2 Gy.

The effect of a constant dose rate during dose delivery on the dose distribution is shown in figure 5.29. For the field shapes that were optimized with a variable number of monitor units during optimization a dose delivery with constant dose rate would lead to an unacceptable dose distribution. It should be noted that if a constant dose rate is assumed for the treatment plan optimization a plan quality almost equal to the dose distribution achievable with variable dose rate was possible for this patient.

5.4.3 Gantry position

As a last component that could lead to errors during dose delivery the influence of the gantry position on the dose distribution is examined. AMCBT treatment plans were generated for a fixed number of beam directions and for these beams the number of monitor units and the MLC positions were optimized. In this section the gantry angle of all beams in the treatment plan is rotated for an angular interval. During dose delivery the dose rate and MLC movement are controlled by the gantry angle, therefore a delay in processing this information would lead to an angular displacement of leaf positions and dose rate.

Treatment plans with an error of the gantry angle of 1°, 5° and 10° were calculated. The

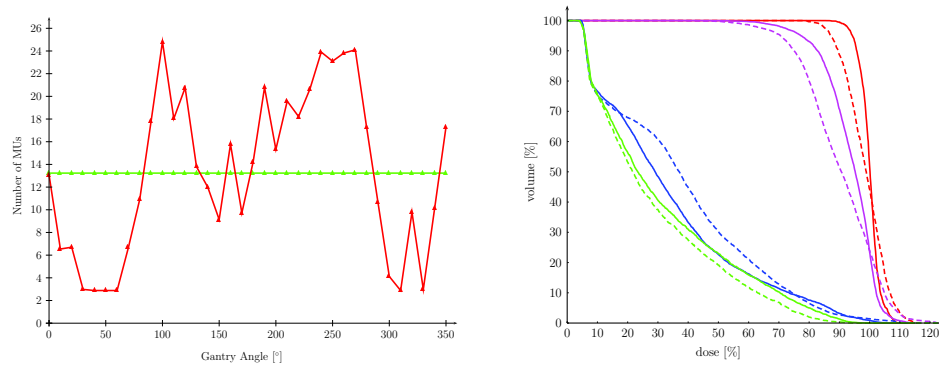


Figure 5.29: Comparison of the dose rate and dose distribution for a constant and variable dose rate.

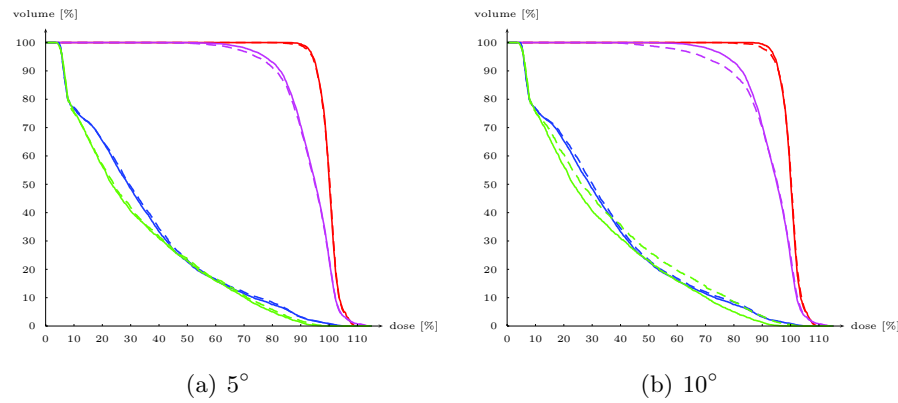


Figure 5.30: DVH for treatment plans with an angular displacement of the MLC leaf positions and dose rate. Displayed are the GTV (red), PTV (pink), rectum (green) and bladder (blue).

DVH for 5° and 10° are shown in figure 5.30. For 1° there was no visible difference in the DVH curves of the original and the modified treatment plan.

A rotation of 5° leads only to small differences. For a 10° rotation the dose coverage of the target decreases from 0.86 to 0.83 and the conformity of the dose distribution decreases from 0.82 to 0.79. The dose to the OARs increases, e.g, the mean dose in the rectum is 26.1 Gy compared to 23.8 Gy for the original treatment plan.

6 Hardware solution for AMCBT

This chapter deals with the hardware solution for AMCBT on a Siemens accelerator. For dynamic rotational dose delivery a linac with the ability to vary the dose rate during treatment and an MLC with dynamic IMRT delivery capabilities are required - two features which are not necessary for step and shoot IMRT. In this chapter the hardware solution that was implemented at DKFZ is explained and the feasibility to perform arc-modulated cone beam therapy is demonstrated.

To begin with, the components needed for dynamic rotation therapy are introduced separately. The key components are the dose rate variation, the dynamic MLC and the gantry rotation. Finally, these components are combined to perform rotation therapy with variable field shapes and variable field weights. Different measurements were performed to verify the dose distributions calculated for AMCBT treatment plans.

6.1 Dose rate modulation

Siemens accelerators normally operate with a constant dose rate, which is controlled by the dose rate control voltage (DRCV). This value is adjustable in the linac control console and depends on the selected machine parameters, e.g. the beam energy. During dose delivery the actual dose rate is adjusted to the predetermined value by changing the pulse repetition frequency (PRF). The principle of dose rate control is the following: while radiation is on, the dose pulses are detected with a measurement device and converted to a direct voltage. This voltage is compared to the predetermined DRCV. If the measured value is smaller, the dose repetition rate is increased if it is larger the repetition rate is decreased. With this circuit, the so called "closed loop", the dose rate is kept constant during delivery.

6.1.1 Dose rate modulation board

The dose rate of the linear accelerator depends on the dose rate control voltage. By changing the DRCV value during dose delivery it is possible to modulate the dose rate. To allow for a patient specific variable DRCV during treatment, an electronic board was developed in collaboration with Siemens which interrupts the DRCV signaling pathway (see figure 6.1). As input, the board needs the cumulative dose for each gantry angle for a specific treatment before starting the dose delivery. During delivery the board adjusts the DRCV value to the specified value for each gantry angle. As a result, the dose rate is modulated.

The following information is submitted to the DRCV modulation board:

- the total number of monitor units to be delivered (MU_{total})

- the gantry rotation speed (v_{Gantry})
- the start and stop angle for the arc ($\varphi_{start}, \varphi_{stop}$)
- nominal values for the dose rate (DR_{std}) and DRCV ($DRCV_{linac}$)
- the dose rate modulation as a function of the gantry angle φ (normalized cumulated dose $NCD(\varphi)$)

The DRCV for each angle between φ_{start} and φ_{stop} in steps of $\Delta\varphi = 1^\circ$ is calculated according to:

$$DRCV(\varphi) = \frac{DRCV_{linac}}{DR_{std}} * MU_{total} * v_{Gantry} * (NCD(\varphi + \Delta\varphi) - NCD(\varphi))$$

The gantry rotation speed for a treatment is calculated in the linac control console based on the total number of monitor units and the rotation interval. The correct total number of MUs would lead to a fast gantry rotation speed, since the console does not know about the dose rate modulation and assumes the maximum dose rate for dose delivery. For example, if the rotation interval is 360° and the number of MUs 500 the console sets the gantry speed to $216^\circ/min$. To slow down the gantry rotation speed an adapted number of MUs is entered to the control console which determines the correct gantry rotation speed for a specific treatment. As a result, the dose delivery is not terminated by delivering the correct number of MUs but by reaching the stop gantry angle.

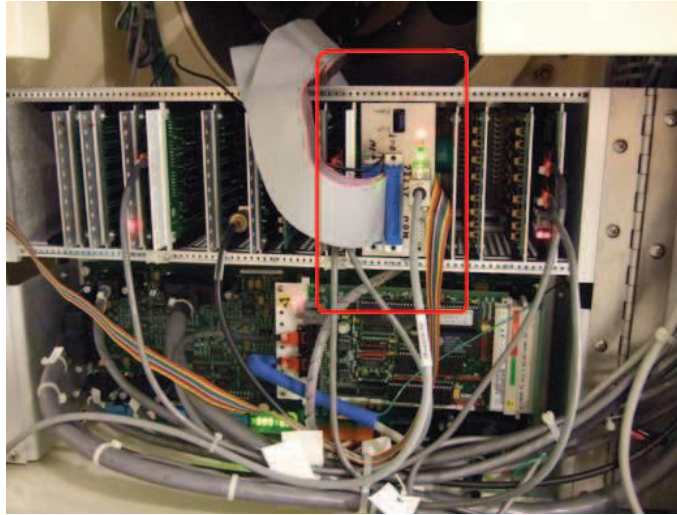


Figure 6.1: Photograph of the dose rate control board (marked with red rectangle).

6.1.2 Experimental verification of dose rate modulation

The first step was to identify the limitations of the dose rate modulation, i.e. the maximum possible change of the DRCV value. The minimum and maximum achievable dose

rates are not influenced by the DRCV board. The maximum dose rate of 300 MU/min corresponds to a DRCV value of 7570 mV. To determine the maximum possible dose rate modulation, the radiation was switched on with a constant DRCV and then this value is changed manually within the software of the DRCV board. If changing the dose rate was possible, the old DRCV value was set again and a bigger change was imposed. This was done until the linac console reports an interlock. This experiment was performed with a Siemens PrimusTM and a Siemens ArtisteTM accelerator. The results were similar, table 6.1 shows the maximum possible DRCV changes for the ArtisteTM linac. The first row displays the initial DRCV value. The minimum and maximum DRCV that this value could be changed to are denoted with $DRCV_{min}$ and $DRCV_{max}$, respectively.

DRCV	$DRCV_{min}$	$DRCV_{max}$
1000	600	3100
2000	1200	5000
3000	1700	7570
4000	2400	7570
5000	3000	7570
6000	3700	7570
7000	4400	7570

Table 6.1: Maximum possible changes of the DRCV. All values are in mV.

How much the DRCV can change depends on the value of the DRCV and if the dose rate should be increased or decreased. For an increasing dose rate bigger changes are possible. For decreasing the dose rate the DRCV value could be reduced by approximately a factor of 1.6.

For the first dosimetric measurements the field size was adjusted to $10 * 10 \text{ cm}^2$. As measurement devices a PTW Farmer-type ionization chamber and the flat panel detector of the ArtisteTM (Siemens Optivue 1000 ART) were used. The dose measured with the ionization chamber was read every 500 ms. The maximum read out frequency of the panel is 15 Hz.

For the first dosimetric measurements the dose rate was set to a constant value and a total of 100 MUs were delivered. This was done for different DRCV values and the dose was measured with an ionization chamber at the isocenter. For the chosen settings a total of 100 MUs should result in a dose of 1 Gy. Table 6.2 summarizes the results. The diagram in figure 6.2 illustrates that the dose for the same number of MUs slightly increases with higher DRCV values. Since the deviation is smaller than 0.5% this effect was not further accounted for.

The progression in time of the DRCV value for two different dose rate levels is shown in figure 6.3. The green curve shows the progression of the DRCV value without the DRCV board interrupting the DRCV signaling pathway. The reason for the larger deviations of the measured DRCV value from the specified value for the two curves with a DRCV of 7570 mV compared to the curve with a DRCV of 3000 mV are caused by an automatic switch of the measurement range and the fixed number of digits transferred by the device used to read out the ionization chamber (Unidos, PTW) over the serial interface after

delivering more than 1 Gy. The shift in time of the three curves is of no importance, because radiation was switched on at different times. After the first second the DRCV is constant in time and the curves with and without the board interrupting the DRCV signaling pathway do not show any difference. Also a lower DRCV of 3000 mV was adjusted very accurately by the DRCV board.

DRCV [mV]	dose [Gy]
1000	0.9996
2000	0.9981
3000	0.9994
4000	1.0010
5000	1.0015
6000	1.0025
7000	1.0025
7570	1.0038

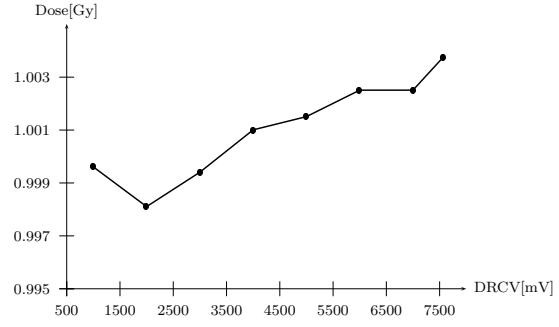


Figure 6.2: Measured dose for the delivery of 100 MUs with different DRCV values.

An eye-catching feature of figure 6.3 is the very high dose rate at the beginning of the irradiation. After turning the radiation on, the linac operates in the so called "open loop", in which the dose rate is not regulated as described before. Instead, the dose rate depends on a nominal value set in the control console for the first second of the irradiation. Therefore the DRCV values sent by the modulation board have no influence on the actual dose rate. This could result in an over dosage at the beginning of the treatment. For example, a treatment that was planned to start with a low dose rate of 60 MU/min (DRCV = 1514 mV) and instead starts with a high dose rate of 300 MU/min (DRCV = 7570 mV) would result in the delivery of 6 MUs instead of 1 MU in the first second.

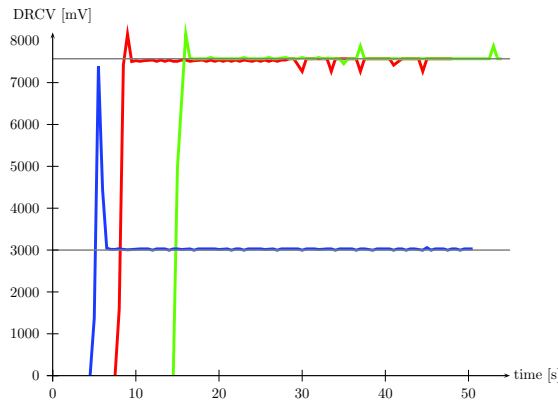


Figure 6.3: A constant DRCV value of 7570 mV and 3000 mV set by the dose rate modulation board over time. The green curve represents the progression of a constant DRCV value without the board that interrupts the DRCV signaling pathway.

To solve the problem of a high dose rate at the beginning of the treatment it is possible to adjust the DRCV value for the open loop in the control console of the linac. There are two issues that need to be respected: (1) The PRF set for the "open loop" is fixed for the first second of the treatment and therefore the dose rate is not modulated and (2) it is not possible throughout the treatment to regulate the DRCV to values that exceed the initial DRCV by more than 20%.

The first issue having no modulation of the dose rate in the first second of the treatment is neglectable. The difference to the planned dose delivery is too small to affect the dose distribution. The second issue is caused by a 20% limit control circuit within the linac control system that avoids repetition rates in the "closed loop" which exceed the value set for the "open loop" by more than +20%. Still, it is possible to change this setting during treatment, as long as the current dose repetition rate is lower than the specified value. Therefore only a treatment that would start with a low dose rate and continue with a rapidly increasing dose rate would cause difficulties.

The next topic under investigation was the behavior of the dose rate while changing the dose rate control voltage. For an accurate treatment it is necessary to examine how fast the dose rate can change and what happens while it is changing. For this analysis treatment plans starting with a constant DRCV and then changing rapidly to another DRCV value were generated. This was performed for increasing and decreasing dose rates with several different DRCV changes.

The best time resolution is possible with the flat panel detector, which was used for these measurements. An example of one single frame recorded during irradiation is displayed in figure 6.4. The stripes in the image are caused by differences in the dose pulse frequency and the read out frequency of the panel. The panel is read out every 66.7 ms but the interval between the dose pulses varies between 5 and 40 ms. During read out of the panel the next dose pulse is fired and therefore this pulse is only registered in the pixels that were not read out yet. To determine the DRCV value in each frame the mean value of all pixels in a user defined area is calculated. For the correlation of the pixel values and the DRCV values a calibration curve was measured.

The result of the image analysis is a DRCV value for each frame and thus the DRCV as a function of time. The input data for the dose rate modulation is the normalized cumulative dose against the gantry angle - and not time. To compare the measured and prescribed DRCV a constant gantry rotation speed is assumed to calculate the prescribed DRCV against time. This assumption is reasonable except for the beginning of the rotation (see section 6.3). Since the calculation of dose delivery time from the gantry angle is not accurate for the first second of the treatment there is a shift of the calculated values against time. Therefore, in the following analysis it was assumed that no delay occurs for sending the new DRCV value and the graph representing the planned DRCV value was shifted in time so that the experimental data most closely matches the prescribed DRCV curve.

Figure 6.5 shows a comparison of the planned and measured DRCV for two examples. The measurement was repeated several times with different DRCV changes. Figure 6.5 shows that changing the dose rate results in an overshoot and undershoot of the DRCV

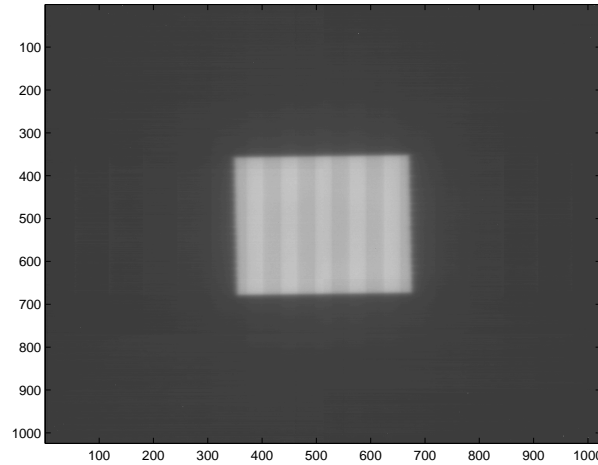


Figure 6.4: *Rectangular radiation field as measured with a flat panel detector.*

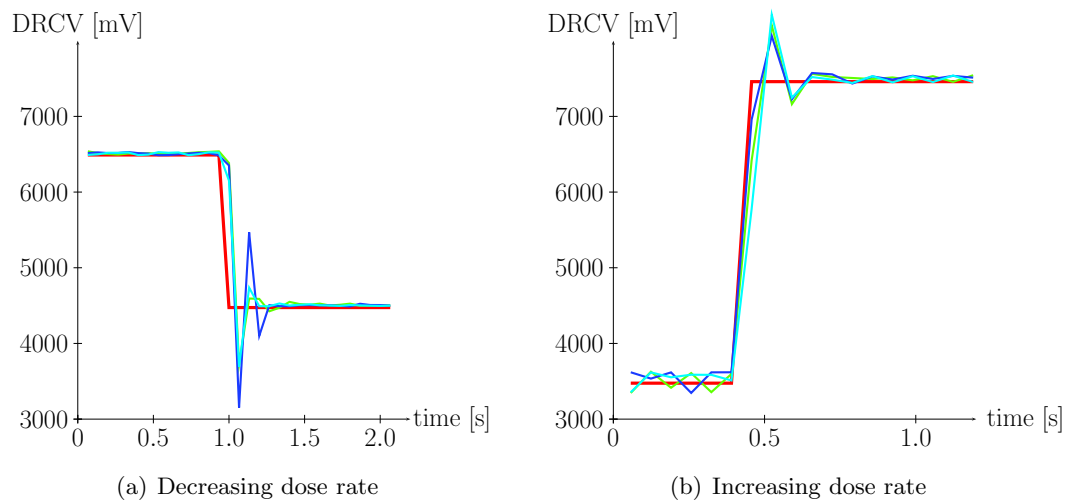


Figure 6.5: *Comparison of the planned (red) and measured (blue, green, cyan) dose rate control voltage for different DRCV changes.*

value, respectively. The amplitude of the oscillation varies for the different measurements. For changing the DRCV from 2976 mV to 6959 mV the maximum overshoot of the DRCV value is 13%, the maximum undershoot for the change from 5990 mV to 3974 mV is 30%. The oscillation of the DRCV happens in a very short time interval, in the order of 200 - 400 ms. The same measurements performed with the ionization chamber and a time resolution of 0.5 seconds do not show the overshoot or undershoot of the dose rate. This oscillation will presumably not influence the final dose distribution and was therefore not further investigated.

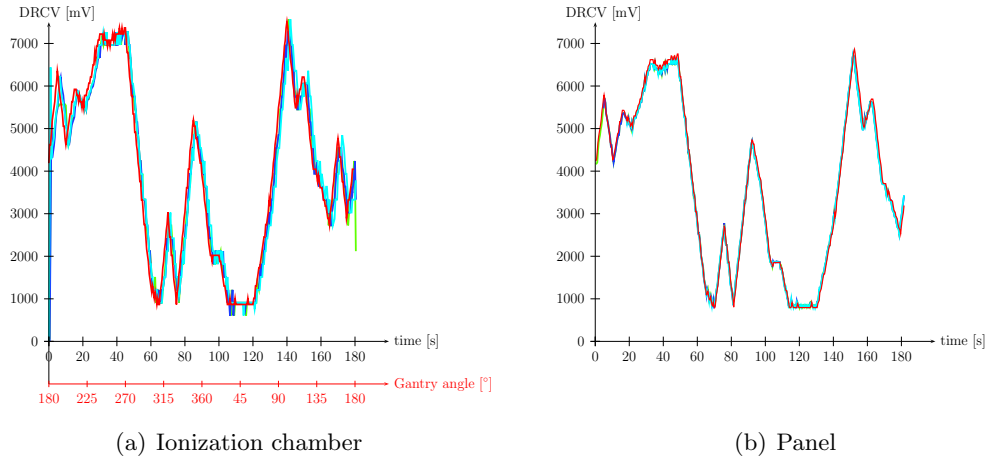


Figure 6.6: Progression of the DRCV value for a prostate patient treatment. The red curve displays the calculated DRCV values. The blue, green and cyan colored curves show the measured DRCV.

Finally, the dose rate that was optimized for a prostate cancer treatment was delivered without variation of the field shapes during dose delivery. The delivered dose was measured with the ionization chamber and with the flat panel detector. Figure 6.6 shows a comparison of the measurement and the theoretical progression of the DRCV value. For the measurement with the ionization chamber the dose was measured every 0.5 seconds and the gantry rotation speed was $120^\circ/\text{min}$. The treatment time for a 360° rotation with $v_{\text{gantry}} = 120^\circ/\text{min}$ is 180 sec. In this example the theoretical progression of the DRCV value is plotted against the gantry angle (red curve and axis in figure 6.6(a)) and the measured DRCV is plotted against time. If the gantry rotates with the specified gantry speed then the time and gantry axes would correspond with each other (according to $t = 60 * \frac{\varphi}{v_{\text{gantry}}}$, φ denotes the gantry angle). There is a good agreement between the prescribed and measured DRCV, but there is a small shift between the curves. This difference in time stays constant for the whole treatment. Presumably it is caused by an incorrect gantry rotation speed at the beginning of the treatment (see section 6.3).

For the measurement with the flat panel detector the gantry speed was $110^\circ/\text{min}$, which results in lower DRCV values. The integration time of the detector was 399 ms. The curves in figure 6.6(b) were shifted in time to get the best agreement between measurement and the theoretical progression of the DRCV value. This measurement confirms

the feasibility of using the DRCV board to change the dose rate during dose delivery in accordance to the planned dose rate.

6.2 MLC control

In this section the dynamic performance of a Siemens 160MLCTM was tested for rotation therapy. This MLC consists of 80 leaf pairs with an isocentric leaf width of 5 mm and a maximum field width of $40 * 40 \text{ cm}^2$. For step and shoot IMRT the movement of the MLC leaves takes place while the radiation is off, therefore the behavior of the leaves during movement is of no importance. For arc therapy the leaves move during irradiation and therefore they need to move to a specified position without (or with as little as possible) delay. During his PhD thesis project Martin Tacke worked on software and hardware developments to realize dynamic control of the MLC to realize tumor tracking with this MLC. The system architecture for the MLC control is described in his thesis [57]. The dynamic MLC control system was used for the realization of dynamic arc therapy.

In contrast to a tracking approach in which the movement of the patient is not known before the treatment the leaf positions for arc therapy are a priori known. The information of the leaf positions are read from the plan file. The program that controls the MLC movement (TrackingTool) linearly interpolates leaf positions for each gantry angle within the rotational interval in steps of 0.1 degree. During treatment the program receives the actual gantry angle and sends leaf positions for this angle to the MLC control console.

The leaves of the MLC are mounted on carriages. For a fixed carriage position the leaves can move a maximum distance of 20 cm to each side. So far the movement of the carriages is not considered within the MLC control software, and therefore the maximum radiation field size that is adjustable with the MLC is $20 * 40 \text{ cm}^2$.

To verify the MLC leaf movement during treatment two methods were used. Treatments were recorded with a flat panel detector and the movement of the leaves as visible on the panel images was compared to the planned positions. Moreover, during treatment the TrackingTool logs the gantry angle, the planned leaf position and the "real-time" leaf position, e.g. the position of the leaves during treatment. This information was also used to determine the positioning accuracy of the leaves during treatment.

The agreement of the planned and "real-time" positions of the leaves as logged by the TrackingTool software is good in most cases. The overview of the movement of leaf pair 40 in figure 6.7(a) shows that the leaves start moving as soon as the gantry starts to rotate. The agreement between the planned and "real-time" positions looks good in this figure. A more detailed view is given in figure 6.7(b). Here it is visible that at the turning points the "real-time" positions slightly deviate from the planned positions. The reason for this is a prediction algorithm which is necessary to account for the systems latency and delay times. The time needed from sending a new leaf position until the leaves start to move to this position is about 400 ms. Therefore it is necessary to employ a prediction algorithm to calculate the next position of the leaves and send this information before the rotation angle for this field shape is reached. In the current implementation this leads to small deviations at extreme points of the MLC movement.

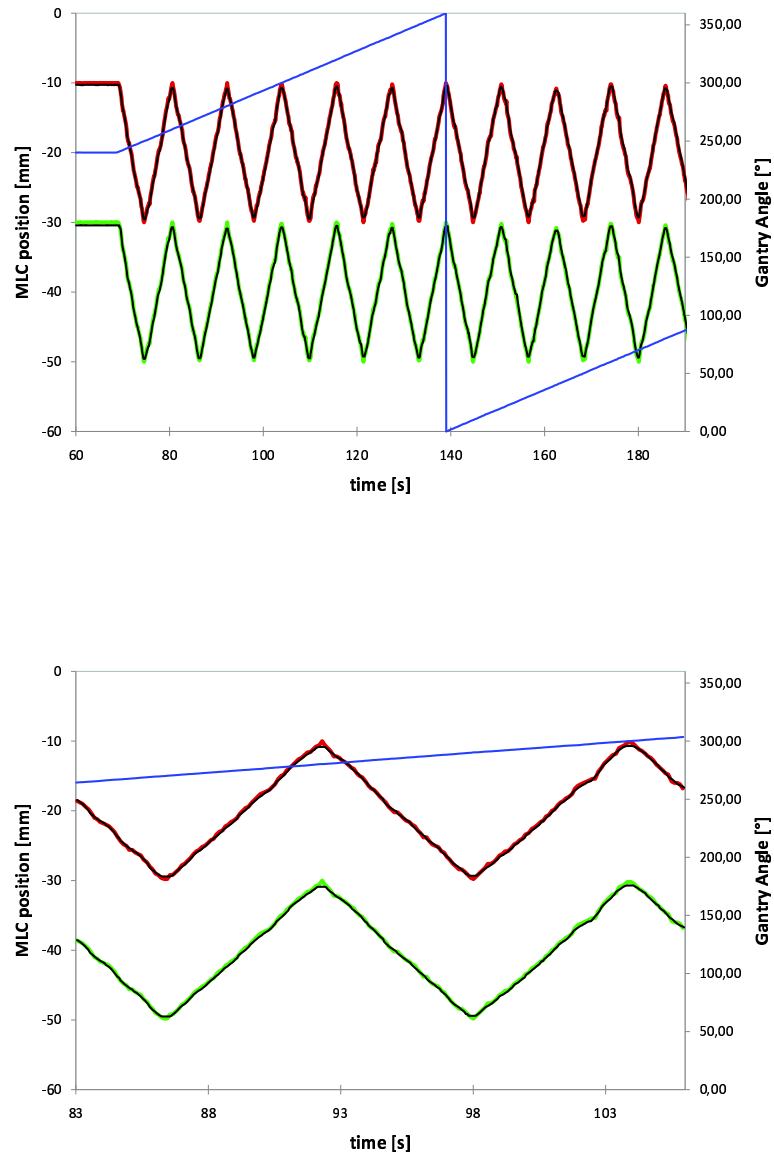


Figure 6.7: Comparison of the planned (green and red curve) and realized (black curve) movement for one leaf pair. The position of the gantry is displayed with the blue curve. The data was recorded during treatment with the MLC control software.

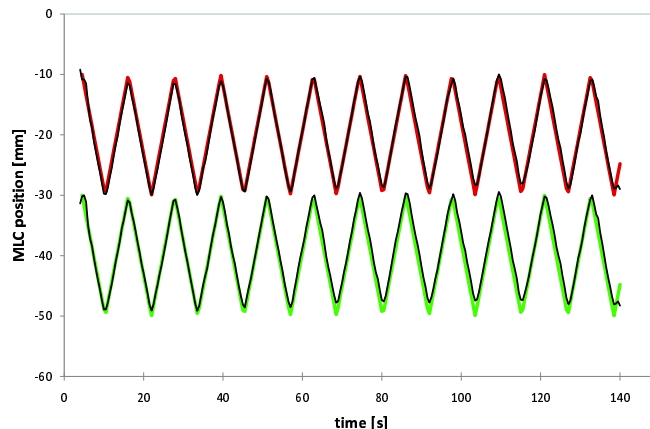


Figure 6.8: Comparison of the planned (green and red curve) and realized (black curve) movement for one leaf pair. The data was recorded during treatment with the a flat panel detector and processed afterwards in MatLab.

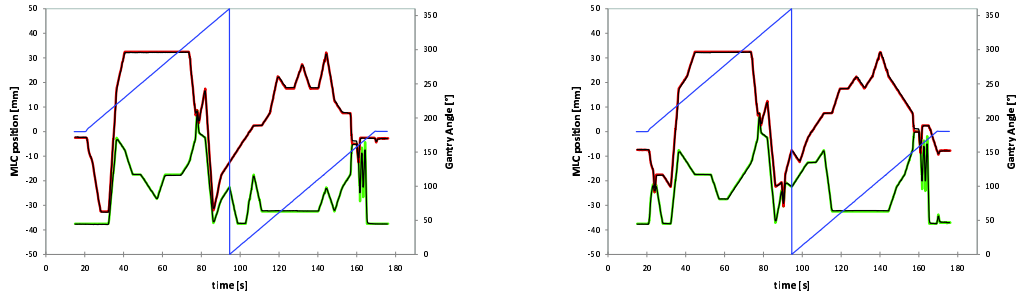
The above example treatment was also recorded with the flat panel detector. Radiation was switched on with a constant dose rate. The linear correlation between leaf positions and the radiation field on the image was determined before the measurement. Therefore a set of rectangular radiation fields with known size were imaged with the detector and the correlation of the MLC leaf positions and the start and stop pixel of the radiation field determined. In figure 6.8 the leaf movement for one leaf pair is shown. This also confirms an agreement between planned and measured leaf positions.

Lastly, the leaf movement for an optimized treatment plan for a prostate cancer patient is shown in figure 6.9 for two leaf pairs. Also for this more complicated leaf movement the agreement between measured and planned leaf positions is good.

6.3 Gantry Rotation

For arc-modulated cone beam therapy a continuously rotating gantry with constant rotation speed is necessary. During treatment plan optimization the gantry speed is calculated from the total number of MUs for a specific plan, as described in section 3.2. A slow gantry rotation speed, e.g. $50^\circ/\text{min}$, allows for large MLC movements and a high number of monitor units per beam direction. With a faster rotating gantry the treatment time decreases, but the restrictions on MLC movement and the maximum number of MUs are more severe. A variable gantry speed would increase the flexibility in arc therapy treatment planning, but for delivery this would also increase the complexity.

During treatment the gantry position is recorded every 100 ms. The dose rate modulation



(a) Leaf pair 40

(b) Leaf pair 41

Figure 6.9: Comparison of the planned (green and red curve) and realized (black curve) movement for an optimized prostate treatment plan. The position of the gantry is displayed with the blue curve. Data was recorded with the MLC control software during treatment.

board taps the gantry signal at the linac backplane and sends it to a PC in the control room. Depending on the current gantry angle the dose rate and MLC leaf positions are adjusted as stated in the plan file. Since the dose rate and leaf positions depend on the gantry angle, it is important that the gantry rotates with the correct constant speed.

In figure 6.10 the measured gantry positions are plotted against time for different rotation speeds. For comparison, the dashed lines represent calculated gantry positions for the specified gantry rotation speed which were shifted in time to best match the measured gantry position data. For all gantry speeds the measured gantry positions agree well with the calculated ones. Figure 6.11 shows the comparison of the calculated and measured positions for a shorter time period. During rotation both curves are in good agreement, but at the beginning of the rotation there are larger differences between the measured and calculated angular positions. To start moving the heavy gantry it needs some time to level off at the specified speed. As visible in figure 6.11 the correct gantry speed is reached after approximately one second, so the overall influence of the slower or faster gantry rotation speed at the beginning of the rotation on the complete single arc dose delivery seems to be negligible.

For all measurements the MV flat panel detector was moved out at a source imager distance of 145 cm. For this setting the movement of the gantry agrees best with the specified speed. In figure 6.12 the movement of the gantry is shown with and without the MV panel in position. If the panel is not retracted the speed of the gantry fluctuates, as visible for the blue curve in figure 6.12.

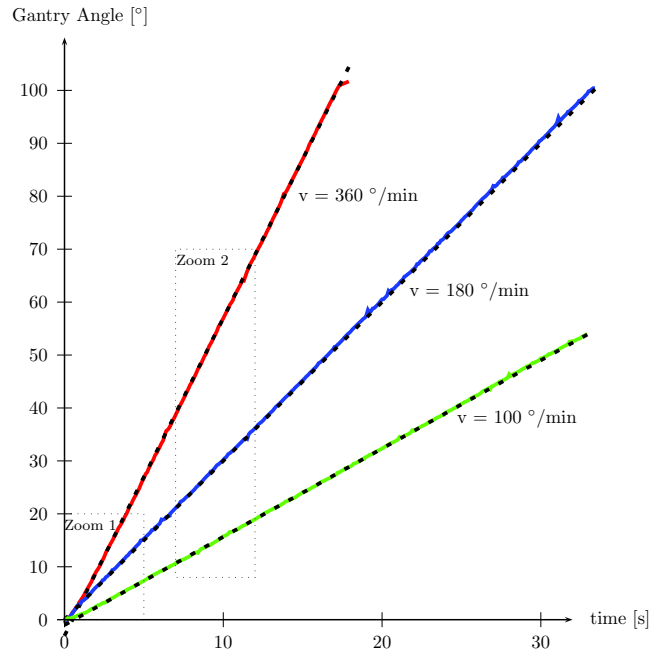


Figure 6.10: The solid lines represent the measured gantry positions for different rotation speeds. As a comparison the dashed lines represent calculated gantry positions for the specified gantry rotation speed.

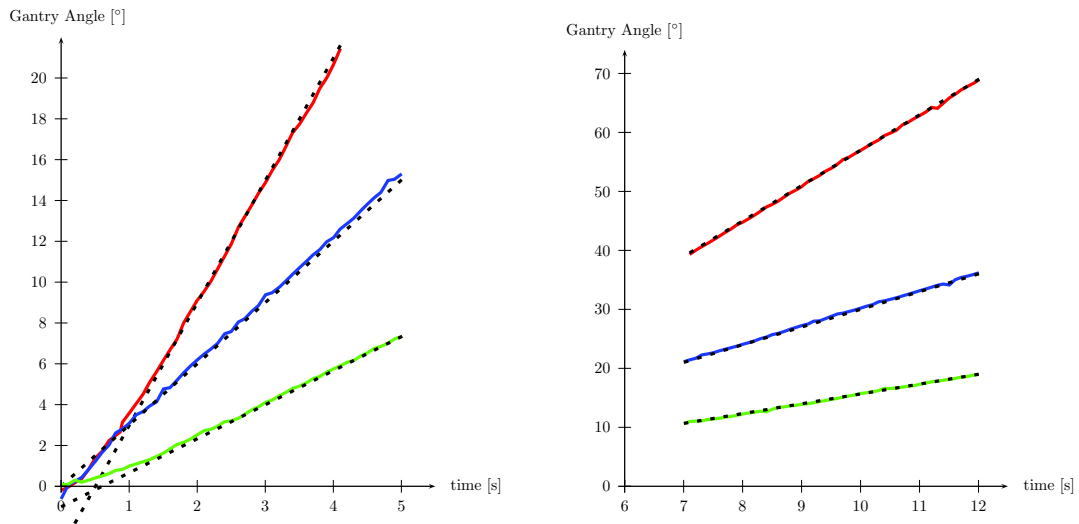


Figure 6.11: Amplification of figure 6.10 for the beginning of the rotation and during rotation.

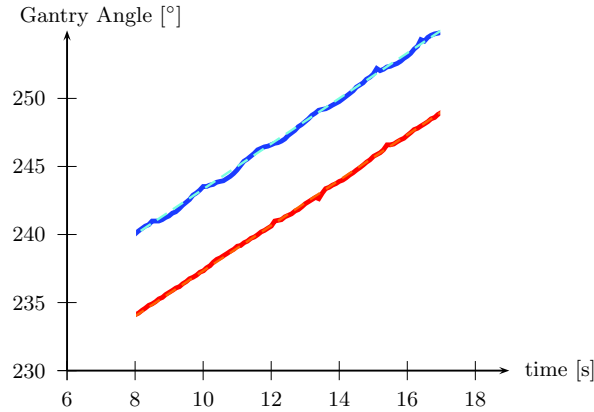


Figure 6.12: Measured gantry positions versus calculated gantry positions for a rotation with the MV panel extracted (red) and retracted (blue).

6.4 Dosimetric verification of AMCBT delivery

6.4.1 Methods and materials

For the verification of the dose distributions calculated for AMCBT measurements were performed with phantoms that were either equipped with films or with ionization chambers. Both phantoms had almost the same geometry: a cylinder with a diameter of 20 cm consisting of 1 cm thick RW3 plates bolted together on two plexiglass rods. Figure 6.13(a) shows the phantom with the first film put between two RW3 plates. With the holes in the RW3 plates it is possible to mark the film and define the same coordinate system on the film as on the transversal slice of the calculated dose distribution. For the film measurement gafchromic EBT films were used. To analyze the measured dose distribution and to compare it with the calculated dose distribution the software VerisoftTM by PTW was used. Only a relative comparison of the dose distributions was performed for the film measurement. For an absolute dosimetric verification the ionization chambers were used. A difference between both phantoms is the position of the plexiglass sticks - they are rotated by 90°. The phantom that could be equipped with multiple ionization chambers is displayed in figure 6.13(b). 25 notches allow the insertion of ionization chambers into the cylindrical phantom. The photograph shows a phantom that is equipped with 5 ionization chambers. The chambers are read out with the PTW MultidosTM multi-channel dosimeter. If the phantom is aligned with the room lasers the middle notch corresponds to the gantry rotation axis. Within the coordinate system of the phantom this notch has the coordinates $x = 0 \text{ mm}$ and $y = 0 \text{ mm}$. All other notches are separated by 20 mm.

For the dose measurements two different treatment plans were used. In the first treatment the dose rate decreases and the MLC leaves move back and forth as seen in figure 6.7 for a gantry rotation of 240°. The second treatment plan was optimized for a prostate cancer patient. Field shapes and weights from this treatment plan were copied to the phantom

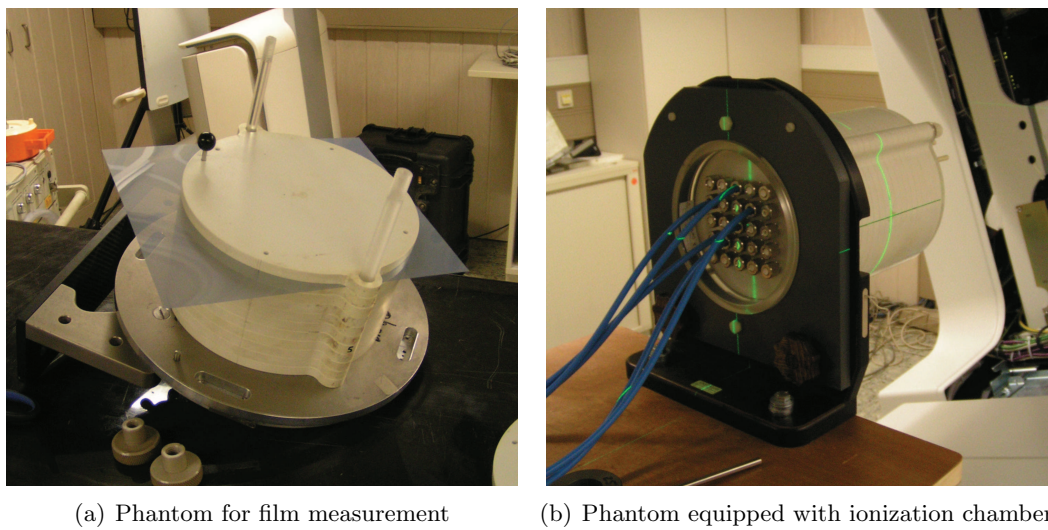


Figure 6.13: *Phantoms used for dose measurements.*

geometry and the dose distribution was recalculated. The gantry speed for a 360° rotation is $v_{Gantry} = 144^\circ/min$. The dose distributions for both treatments are shown in figure 6.14.

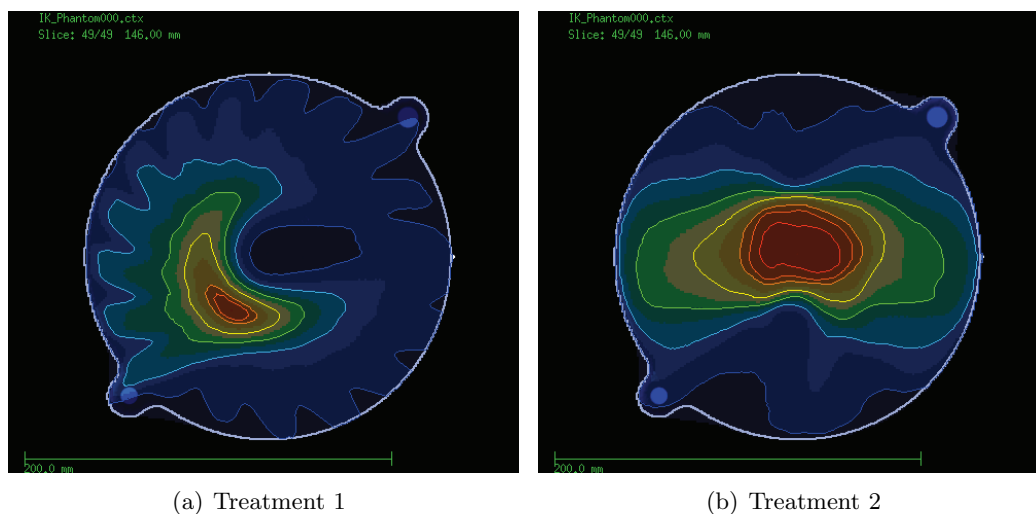


Figure 6.14: *Dose distributions for the treatment plans used for dosimetric verification of AMCBT dose delivery.*

6.4.2 Results 1: multi-ionization chambers

Table 6.2 displays the dose values that were calculated for treatment plan 1 for all possible x-y-coordinates of the ionization chambers for the slice in the isocenter ($z = 146$). Profiles

in x- and y-direction for y and x positions of -40 mm, -20 mm, 0 mm, 20 mm and 40 mm, respectively, are displayed in figure 6.15. The measured values and the deviations from the calculated doses are reported in table 6.3 for 3 measurements.

		x-coordinate				
		-40	-20	0	20	40
y-coordinate	40	0.663	0.795	0.601	0.382	0.261
	20	1.077	0.832	0.293	0.22	0.207
	0	1.371	0.626	0.106	0.094	0.157
	-20	1.422	1.458	0.775	0.595	0.484
	-40	1.026	1.357	1.138	0.716	0.441

Table 6.2: *Calculated dose values for treatment 1. Dose values are given in Gy, coordinates in mm.*

(a) Measurement 1

		x-coordinate				
		-40	-20	0	20	40
y-coordinate	40					
	20		0.831	0.270		
	0	1.328		0.114		
	-20	1.369				
	-40					

		x-coordinate				
		-40	-20	0	20	40
y-coordinate	40					
	20		-0.1	-7.8		
	0	-3.1		7.1		
	-20	-3.7				
	-40					

(b) Measurement 2

		x-coordinate				
		-40	-20	0	20	40
y-coordinate	40					
	20		0.835	0.273		
	0	1.331		0.115		
	-20	1.371				
	-40					

		x-coordinate				
		-40	-20	0	20	40
y-coordinate	40					
	20		0.4	-6.7		
	0	-3.0		8.8		
	-20	-3.6				
	-40					

(c) Measurement 3

		x-coordinate				
		-40	-20	0	20	40
y-coordinate	40			0.627		
	20	1.058			0.204	
	0			0.112		
	-20		1.463			
	-40					

		x-coordinate				
		-40	-20	0	20	40
y-coordinate	40			4.3		
	20	-1.7			-7.1	
	0			5.8		
	-20		0.4			
	-40					

Table 6.3: *On the left side the measured dose values for treatment plan 1 for 3 measurements are shown (values are in Gy). On the right side the percentage deviation of the measured value from the calculated value is displayed (in %).*

The first measurement shows an acceptable agreement between the measured and calculated dose values for high doses, but for dose values below 0.3 Gy the percentage deviation exceeds 5%. The results of the second measurement are in good agreement with the first measurement. For the third measurement the positions of the ionization chambers was

changed. As seen before, there is a good agreement for high dose values but too large deviations in the low dose region.

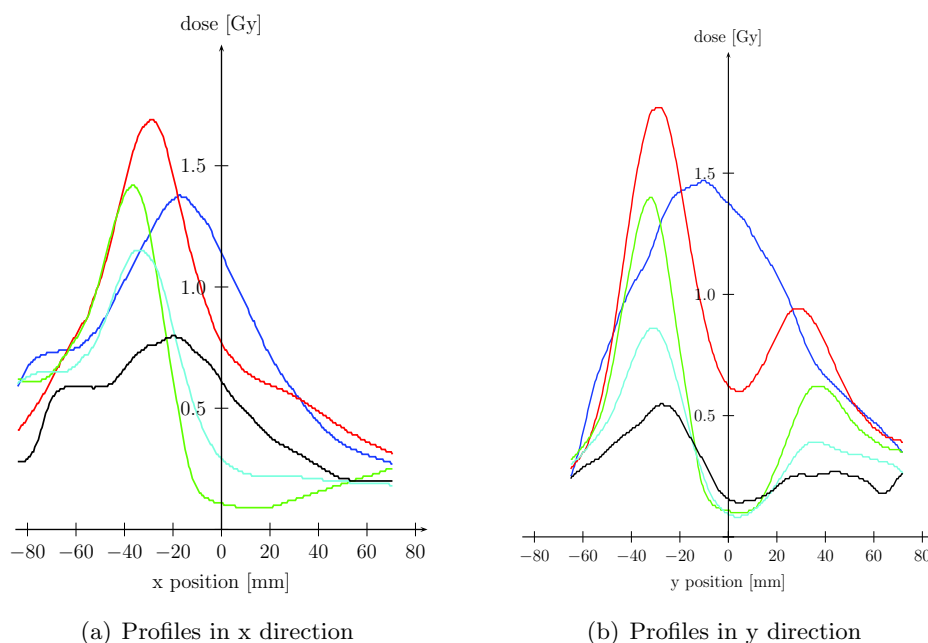


Figure 6.15: *Calculated dose profiles along the possible positions of the ionization chamber in the phantom. The profile in x direction at a y position of -40 mm is displayed in blue, -20 mm in red, 0 mm in green, 20 mm in cyan and 40 mm in black. For profiles in y direction the same colors are used.*

For the second treatment plan the comparison of the measured and calculated dose values for several ionization chamber positions is displayed in table ???. For this treatment the z-position of the chambers was also varied between measurements. Most measurements were performed with the chambers positioned in the isocenter plane at $z = 146$. For a maximum acceptable deviation of 5% all measured dose values agree with the calculated dose values. Those chamber positions that were repeatedly measured showed a very good reproducibility of the dose delivery, e.g. the dose measured with the chamber at the isocenter was 2.072 Gy, 2.098 Gy, 2.095 Gy and 2.095 Gy.

For the second treatment plan there was an improved agreement of the measurements with the calculated dose values. This might be caused by the fact that most dose values were higher compared to the dose values of treatment plan 1 and moreover dose gradients are not as steep as for the first treatment plan (see figure 6.18).

z = 156 mm	<table><tr><th colspan="2"></th><th colspan="5">x-coordinate</th></tr><tr><th colspan="2"></th><th>-40</th><th>-20</th><th>0</th><th>20</th><th>40</th></tr><tr><th rowspan="4">y-coordinate</th><th>40</th><td></td><td></td><td></td><td></td><td></td></tr><tr><th>20</th><td></td><td></td><td>1.927</td><td>2.020</td><td></td></tr><tr><th>0</th><td>1.753</td><td></td><td></td><td>2.107</td><td></td></tr><tr><th>-20</th><td>1.568</td><td></td><td></td><td></td><td></td></tr><tr><th>-40</th><td></td><td></td><td></td><td></td><td></td></tr></table>			x-coordinate							-40	-20	0	20	40	y-coordinate	40						20			1.927	2.020		0	1.753			2.107		-20	1.568					-40						<table><tr><th colspan="2"></th><th colspan="5">x-coordinate</th></tr><tr><th colspan="2"></th><th>-40</th><th>-20</th><th>0</th><th>20</th><th>40</th></tr><tr><th rowspan="4">y-coordinate</th><th>40</th><td></td><td></td><td></td><td></td><td></td></tr><tr><th>20</th><td></td><td></td><td>1.980</td><td>2.116</td><td></td></tr><tr><th>0</th><td>1.745</td><td></td><td></td><td>2.127</td><td></td></tr><tr><th>-20</th><td>1.583</td><td></td><td></td><td></td><td></td></tr><tr><th>-40</th><td></td><td></td><td></td><td></td><td></td></tr></table>			x-coordinate							-40	-20	0	20	40	y-coordinate	40						20			1.980	2.116		0	1.745			2.127		-20	1.583					-40						<table><tr><th colspan="2"></th><th colspan="5">x-coordinate</th></tr><tr><th colspan="2"></th><th>-40</th><th>-20</th><th>0</th><th>20</th><th>40</th></tr><tr><th rowspan="4">y-coordinate</th><th>40</th><td></td><td></td><td></td><td></td><td></td></tr><tr><th>20</th><td></td><td></td><td>2.8</td><td>4.8</td><td></td></tr><tr><th>0</th><td>-0.4</td><td></td><td></td><td>1.0</td><td></td></tr><tr><th>-20</th><td>1.0</td><td></td><td></td><td></td><td></td></tr><tr><th>-40</th><td></td><td></td><td></td><td></td><td></td></tr></table>			x-coordinate							-40	-20	0	20	40	y-coordinate	40						20			2.8	4.8		0	-0.4			1.0		-20	1.0					-40					
			x-coordinate																																																																																																																																							
			-40	-20	0	20	40																																																																																																																																			
	y-coordinate	40																																																																																																																																								
		20			1.927	2.020																																																																																																																																				
0		1.753			2.107																																																																																																																																					
-20		1.568																																																																																																																																								
-40																																																																																																																																										
		x-coordinate																																																																																																																																								
		-40	-20	0	20	40																																																																																																																																				
y-coordinate	40																																																																																																																																									
	20			1.980	2.116																																																																																																																																					
	0	1.745			2.127																																																																																																																																					
	-20	1.583																																																																																																																																								
-40																																																																																																																																										
		x-coordinate																																																																																																																																								
		-40	-20	0	20	40																																																																																																																																				
y-coordinate	40																																																																																																																																									
	20			2.8	4.8																																																																																																																																					
	0	-0.4			1.0																																																																																																																																					
	-20	1.0																																																																																																																																								
-40																																																																																																																																										
z = 136 mm	<table><tr><th colspan="2"></th><th colspan="5">x-coordinate</th></tr><tr><th colspan="2"></th><th>-40</th><th>-20</th><th>0</th><th>20</th><th>40</th></tr><tr><th rowspan="4">y-coordinate</th><th>40</th><td></td><td></td><td></td><td></td><td></td></tr><tr><th>20</th><td></td><td></td><td>1.910</td><td>1.948</td><td></td></tr><tr><th>0</th><td>1.597</td><td></td><td></td><td>2.058</td><td></td></tr><tr><th>-20</th><td>1.293</td><td></td><td></td><td></td><td></td></tr><tr><th>-40</th><td></td><td></td><td></td><td></td><td></td></tr></table>			x-coordinate							-40	-20	0	20	40	y-coordinate	40						20			1.910	1.948		0	1.597			2.058		-20	1.293					-40						<table><tr><th colspan="2"></th><th colspan="5">x-coordinate</th></tr><tr><th colspan="2"></th><th>-40</th><th>-20</th><th>0</th><th>20</th><th>40</th></tr><tr><th rowspan="4">y-coordinate</th><th>40</th><td></td><td></td><td></td><td></td><td></td></tr><tr><th>20</th><td></td><td></td><td>1.990</td><td>2.032</td><td></td></tr><tr><th>0</th><td>1.571</td><td></td><td></td><td>2.083</td><td></td></tr><tr><th>-20</th><td>1.254</td><td></td><td></td><td></td><td></td></tr><tr><th>-40</th><td></td><td></td><td></td><td></td><td></td></tr></table>			x-coordinate							-40	-20	0	20	40	y-coordinate	40						20			1.990	2.032		0	1.571			2.083		-20	1.254					-40						<table><tr><th colspan="2"></th><th colspan="5">x-coordinate</th></tr><tr><th colspan="2"></th><th>-40</th><th>-20</th><th>0</th><th>20</th><th>40</th></tr><tr><th rowspan="4">y-coordinate</th><th>40</th><td></td><td></td><td></td><td></td><td></td></tr><tr><th>20</th><td></td><td></td><td>4.2</td><td>4.3</td><td></td></tr><tr><th>0</th><td>-1.6</td><td></td><td></td><td>1.2</td><td></td></tr><tr><th>-20</th><td>-3.0</td><td></td><td></td><td></td><td></td></tr><tr><th>-40</th><td></td><td></td><td></td><td></td><td></td></tr></table>			x-coordinate							-40	-20	0	20	40	y-coordinate	40						20			4.2	4.3		0	-1.6			1.2		-20	-3.0					-40					
			x-coordinate																																																																																																																																							
			-40	-20	0	20	40																																																																																																																																			
	y-coordinate	40																																																																																																																																								
		20			1.910	1.948																																																																																																																																				
0		1.597			2.058																																																																																																																																					
-20		1.293																																																																																																																																								
-40																																																																																																																																										
		x-coordinate																																																																																																																																								
		-40	-20	0	20	40																																																																																																																																				
y-coordinate	40																																																																																																																																									
	20			1.990	2.032																																																																																																																																					
	0	1.571			2.083																																																																																																																																					
	-20	1.254																																																																																																																																								
-40																																																																																																																																										
		x-coordinate																																																																																																																																								
		-40	-20	0	20	40																																																																																																																																				
y-coordinate	40																																																																																																																																									
	20			4.2	4.3																																																																																																																																					
	0	-1.6			1.2																																																																																																																																					
	-20	-3.0																																																																																																																																								
-40																																																																																																																																										
z = 146 mm	<table><tr><th colspan="2"></th><th colspan="5">x-coordinate</th></tr><tr><th colspan="2"></th><th>-40</th><th>-20</th><th>0</th><th>20</th><th>40</th></tr><tr><th rowspan="4">y-coordinate</th><th>40</th><td></td><td></td><td></td><td></td><td></td></tr><tr><th>20</th><td></td><td></td><td>1.936</td><td>1.982</td><td></td></tr><tr><th>0</th><td>1.663</td><td></td><td></td><td>2.063</td><td></td></tr><tr><th>-20</th><td>1.337</td><td></td><td></td><td></td><td></td></tr><tr><th>-40</th><td></td><td></td><td></td><td></td><td></td></tr></table>			x-coordinate							-40	-20	0	20	40	y-coordinate	40						20			1.936	1.982		0	1.663			2.063		-20	1.337					-40						<table><tr><th colspan="2"></th><th colspan="5">x-coordinate</th></tr><tr><th colspan="2"></th><th>-40</th><th>-20</th><th>0</th><th>20</th><th>40</th></tr><tr><th rowspan="4">y-coordinate</th><th>40</th><td></td><td></td><td></td><td></td><td></td></tr><tr><th>20</th><td></td><td></td><td>1.959</td><td>2.060</td><td></td></tr><tr><th>0</th><td>1.641</td><td></td><td></td><td>2.072</td><td></td></tr><tr><th>-20</th><td>1.302</td><td></td><td></td><td></td><td></td></tr><tr><th>-40</th><td></td><td></td><td></td><td></td><td></td></tr></table>			x-coordinate							-40	-20	0	20	40	y-coordinate	40						20			1.959	2.060		0	1.641			2.072		-20	1.302					-40						<table><tr><th colspan="2"></th><th colspan="5">x-coordinate</th></tr><tr><th colspan="2"></th><th>-40</th><th>-20</th><th>0</th><th>20</th><th>40</th></tr><tr><th rowspan="4">y-coordinate</th><th>40</th><td></td><td></td><td></td><td></td><td></td></tr><tr><th>20</th><td></td><td></td><td>1.2</td><td>3.9</td><td></td></tr><tr><th>0</th><td>-1.3</td><td></td><td></td><td>0.4</td><td></td></tr><tr><th>-20</th><td>-2.6</td><td></td><td></td><td></td><td></td></tr><tr><th>-40</th><td></td><td></td><td></td><td></td><td></td></tr></table>			x-coordinate							-40	-20	0	20	40	y-coordinate	40						20			1.2	3.9		0	-1.3			0.4		-20	-2.6					-40					
			x-coordinate																																																																																																																																							
			-40	-20	0	20	40																																																																																																																																			
	y-coordinate	40																																																																																																																																								
		20			1.936	1.982																																																																																																																																				
0		1.663			2.063																																																																																																																																					
-20		1.337																																																																																																																																								
-40																																																																																																																																										
		x-coordinate																																																																																																																																								
		-40	-20	0	20	40																																																																																																																																				
y-coordinate	40																																																																																																																																									
	20			1.959	2.060																																																																																																																																					
	0	1.641			2.072																																																																																																																																					
	-20	1.302																																																																																																																																								
-40																																																																																																																																										
		x-coordinate																																																																																																																																								
		-40	-20	0	20	40																																																																																																																																				
y-coordinate	40																																																																																																																																									
	20			1.2	3.9																																																																																																																																					
	0	-1.3			0.4																																																																																																																																					
	-20	-2.6																																																																																																																																								
-40																																																																																																																																										
z = 146 mm	<table><tr><th colspan="2"></th><th colspan="5">x-coordinate</th></tr><tr><th colspan="2"></th><th>-40</th><th>-20</th><th>0</th><th>20</th><th>40</th></tr><tr><th rowspan="4">y-coordinate</th><th>40</th><td></td><td></td><td></td><td></td><td></td></tr><tr><th>20</th><td></td><td></td><td></td><td></td><td></td></tr><tr><th>0</th><td></td><td>2.015</td><td>2.063</td><td>2.026</td><td></td></tr><tr><th>-20</th><td></td><td></td><td>1.177</td><td></td><td></td></tr><tr><th>-40</th><td></td><td></td><td>0.271</td><td></td><td></td></tr></table>			x-coordinate							-40	-20	0	20	40	y-coordinate	40						20						0		2.015	2.063	2.026		-20			1.177			-40			0.271			<table><tr><th colspan="2"></th><th colspan="5">x-coordinate</th></tr><tr><th colspan="2"></th><th>-40</th><th>-20</th><th>0</th><th>20</th><th>40</th></tr><tr><th rowspan="4">y-coordinate</th><th>40</th><td></td><td></td><td></td><td></td><td></td></tr><tr><th>20</th><td></td><td></td><td></td><td></td><td></td></tr><tr><th>0</th><td></td><td>2.079</td><td>2.098</td><td>2.072</td><td></td></tr><tr><th>-20</th><td></td><td></td><td>1.205</td><td></td><td></td></tr><tr><th>-40</th><td></td><td></td><td>0.272</td><td></td><td></td></tr></table>			x-coordinate							-40	-20	0	20	40	y-coordinate	40						20						0		2.079	2.098	2.072		-20			1.205			-40			0.272			<table><tr><th colspan="2"></th><th colspan="5">x-coordinate</th></tr><tr><th colspan="2"></th><th>-40</th><th>-20</th><th>0</th><th>20</th><th>40</th></tr><tr><th rowspan="4">y-coordinate</th><th>40</th><td></td><td></td><td></td><td></td><td></td></tr><tr><th>20</th><td></td><td></td><td></td><td></td><td></td></tr><tr><th>0</th><td></td><td>3.2</td><td>1.7</td><td>2.3</td><td></td></tr><tr><th>-20</th><td></td><td></td><td>2.4</td><td></td><td></td></tr><tr><th>-40</th><td></td><td></td><td>0.2</td><td></td><td></td></tr></table>			x-coordinate							-40	-20	0	20	40	y-coordinate	40						20						0		3.2	1.7	2.3		-20			2.4			-40			0.2		
			x-coordinate																																																																																																																																							
			-40	-20	0	20	40																																																																																																																																			
	y-coordinate	40																																																																																																																																								
		20																																																																																																																																								
0			2.015	2.063	2.026																																																																																																																																					
-20				1.177																																																																																																																																						
-40			0.271																																																																																																																																							
		x-coordinate																																																																																																																																								
		-40	-20	0	20	40																																																																																																																																				
y-coordinate	40																																																																																																																																									
	20																																																																																																																																									
	0		2.079	2.098	2.072																																																																																																																																					
	-20			1.205																																																																																																																																						
-40			0.272																																																																																																																																							
		x-coordinate																																																																																																																																								
		-40	-20	0	20	40																																																																																																																																				
y-coordinate	40																																																																																																																																									
	20																																																																																																																																									
	0		3.2	1.7	2.3																																																																																																																																					
	-20			2.4																																																																																																																																						
-40			0.2																																																																																																																																							
z = 146 mm	<table><tr><th colspan="2"></th><th colspan="5">x-coordinate</th></tr><tr><th colspan="2"></th><th>-40</th><th>-20</th><th>0</th><th>20</th><th>40</th></tr><tr><th rowspan="4">y-coordinate</th><th>40</th><td></td><td></td><td>0.535</td><td></td><td></td></tr><tr><th>20</th><td>1.395</td><td></td><td></td><td>1.854</td><td></td></tr><tr><th>0</th><td></td><td></td><td>2.063</td><td></td><td></td></tr><tr><th>-20</th><td></td><td>1.535</td><td></td><td></td><td></td></tr><tr><th>-40</th><td></td><td></td><td></td><td></td><td></td></tr></table>			x-coordinate							-40	-20	0	20	40	y-coordinate	40			0.535			20	1.395			1.854		0			2.063			-20		1.535				-40						<table><tr><th colspan="2"></th><th colspan="5">x-coordinate</th></tr><tr><th colspan="2"></th><th>-40</th><th>-20</th><th>0</th><th>20</th><th>40</th></tr><tr><th rowspan="4">y-coordinate</th><th>40</th><td></td><td></td><td>0.551</td><td></td><td></td></tr><tr><th>20</th><td>1.428</td><td></td><td></td><td>1.899</td><td></td></tr><tr><th>0</th><td></td><td></td><td>2.095</td><td></td><td></td></tr><tr><th>-20</th><td></td><td>1.551</td><td></td><td></td><td></td></tr><tr><th>-40</th><td></td><td></td><td></td><td></td><td></td></tr></table>			x-coordinate							-40	-20	0	20	40	y-coordinate	40			0.551			20	1.428			1.899		0			2.095			-20		1.551				-40						<table><tr><th colspan="2"></th><th colspan="5">x-coordinate</th></tr><tr><th colspan="2"></th><th>-40</th><th>-20</th><th>0</th><th>20</th><th>40</th></tr><tr><th rowspan="4">y-coordinate</th><th>40</th><td></td><td></td><td>3.1</td><td></td><td></td></tr><tr><th>20</th><td>2.3</td><td></td><td></td><td>2.4</td><td></td></tr><tr><th>0</th><td></td><td></td><td>1.5</td><td></td><td></td></tr><tr><th>-20</th><td></td><td>1.0</td><td></td><td></td><td></td></tr><tr><th>-40</th><td></td><td></td><td></td><td></td><td></td></tr></table>			x-coordinate							-40	-20	0	20	40	y-coordinate	40			3.1			20	2.3			2.4		0			1.5			-20		1.0				-40					
			x-coordinate																																																																																																																																							
			-40	-20	0	20	40																																																																																																																																			
	y-coordinate	40			0.535																																																																																																																																					
		20	1.395			1.854																																																																																																																																				
0				2.063																																																																																																																																						
-20			1.535																																																																																																																																							
-40																																																																																																																																										
		x-coordinate																																																																																																																																								
		-40	-20	0	20	40																																																																																																																																				
y-coordinate	40			0.551																																																																																																																																						
	20	1.428			1.899																																																																																																																																					
	0			2.095																																																																																																																																						
	-20		1.551																																																																																																																																							
-40																																																																																																																																										
		x-coordinate																																																																																																																																								
		-40	-20	0	20	40																																																																																																																																				
y-coordinate	40			3.1																																																																																																																																						
	20	2.3			2.4																																																																																																																																					
	0			1.5																																																																																																																																						
	-20		1.0																																																																																																																																							
-40																																																																																																																																										
z = 146 mm	<table><tr><th colspan="2"></th><th colspan="5">x-coordinate</th></tr><tr><th colspan="2"></th><th>-40</th><th>-20</th><th>0</th><th>20</th><th>40</th></tr><tr><th rowspan="4">y-coordinate</th><th>40</th><td></td><td></td><td>0.535</td><td></td><td></td></tr><tr><th>20</th><td>1.395</td><td></td><td></td><td>1.854</td><td></td></tr><tr><th>0</th><td></td><td></td><td>2.063</td><td></td><td></td></tr><tr><th>-20</th><td></td><td>1.535</td><td></td><td></td><td></td></tr><tr><th>-40</th><td></td><td></td><td></td><td></td><td></td></tr></table>			x-coordinate							-40	-20	0	20	40	y-coordinate	40			0.535			20	1.395			1.854		0			2.063			-20		1.535				-40						<table><tr><th colspan="2"></th><th colspan="5">x-coordinate</th></tr><tr><th colspan="2"></th><th>-40</th><th>-20</th><th>0</th><th>20</th><th>40</th></tr><tr><th rowspan="4">y-coordinate</th><th>40</th><td></td><td></td><td>0.549</td><td></td><td></td></tr><tr><th>20</th><td>1.428</td><td></td><td></td><td>1.900</td><td></td></tr><tr><th>0</th><td></td><td></td><td>2.095</td><td></td><td></td></tr><tr><th>-20</th><td></td><td>1.554</td><td></td><td></td><td></td></tr><tr><th>-40</th><td></td><td></td><td></td><td></td><td></td></tr></table>			x-coordinate							-40	-20	0	20	40	y-coordinate	40			0.549			20	1.428			1.900		0			2.095			-20		1.554				-40						<table><tr><th colspan="2"></th><th colspan="5">x-coordinate</th></tr><tr><th colspan="2"></th><th>-40</th><th>-20</th><th>0</th><th>20</th><th>40</th></tr><tr><th rowspan="4">y-coordinate</th><th>40</th><td></td><td></td><td>2.7</td><td></td><td></td></tr><tr><th>20</th><td>2.4</td><td></td><td></td><td>2.5</td><td></td></tr><tr><th>0</th><td></td><td></td><td>1.5</td><td></td><td></td></tr><tr><th>-20</th><td></td><td>1.2</td><td></td><td></td><td></td></tr><tr><th>-40</th><td></td><td></td><td></td><td></td><td></td></tr></table>			x-coordinate							-40	-20	0	20	40	y-coordinate	40			2.7			20	2.4			2.5		0			1.5			-20		1.2				-40					
			x-coordinate																																																																																																																																							
			-40	-20	0	20	40																																																																																																																																			
	y-coordinate	40			0.535																																																																																																																																					
		20	1.395			1.854																																																																																																																																				
0				2.063																																																																																																																																						
-20			1.535																																																																																																																																							
-40																																																																																																																																										
		x-coordinate																																																																																																																																								
		-40	-20	0	20	40																																																																																																																																				
y-coordinate	40			0.549																																																																																																																																						
	20	1.428			1.900																																																																																																																																					
	0			2.095																																																																																																																																						
	-20		1.554																																																																																																																																							
-40																																																																																																																																										
		x-coordinate																																																																																																																																								
		-40	-20	0	20	40																																																																																																																																				
y-coordinate	40			2.7																																																																																																																																						
	20	2.4			2.5																																																																																																																																					
	0			1.5																																																																																																																																						
	-20		1.2																																																																																																																																							
-40																																																																																																																																										
z = 166 mm	<table><tr><th colspan="2"></th><th colspan="5">x-coordinate</th></tr><tr><th colspan="2"></th><th>-40</th><th>-20</th><th>0</th><th>20</th><th>40</th></tr><tr><th rowspan="4">y-coordinate</th><th>40</th><td></td><td></td><td>0.476</td><td></td><td></td></tr><tr><th>20</th><td>1.274</td><td></td><td></td><td>1.738</td><td></td></tr><tr><th>0</th><td></td><td></td><td>2.134</td><td></td><td></td></tr><tr><th>-20</th><td></td><td>1.786</td><td></td><td></td><td></td></tr><tr><th>-40</th><td></td><td></td><td></td><td></td><td></td></tr></table>			x-coordinate							-40	-20	0	20	40	y-coordinate	40			0.476			20	1.274			1.738		0			2.134			-20		1.786				-40						<table><tr><th colspan="2"></th><th colspan="5">x-coordinate</th></tr><tr><th colspan="2"></th><th>-40</th><th>-20</th><th>0</th><th>20</th><th>40</th></tr><tr><th rowspan="4">y-coordinate</th><th>40</th><td></td><td></td><td>0.478</td><td></td><td></td></tr><tr><th>20</th><td>1.236</td><td></td><td></td><td>1.757</td><td></td></tr><tr><th>0</th><td></td><td></td><td>2.153</td><td></td><td></td></tr><tr><th>-20</th><td></td><td>1.781</td><td></td><td></td><td></td></tr><tr><th>-40</th><td></td><td></td><td></td><td></td><td></td></tr></table>			x-coordinate							-40	-20	0	20	40	y-coordinate	40			0.478			20	1.236			1.757		0			2.153			-20		1.781				-40						<table><tr><th colspan="2"></th><th colspan="5">x-coordinate</th></tr><tr><th colspan="2"></th><th>-40</th><th>-20</th><th>0</th><th>20</th><th>40</th></tr><tr><th rowspan="4">y-coordinate</th><th>40</th><td></td><td></td><td>0.4</td><td></td><td></td></tr><tr><th>20</th><td>-2.9</td><td></td><td></td><td>1.1</td><td></td></tr><tr><th>0</th><td></td><td></td><td>0.9</td><td></td><td></td></tr><tr><th>-20</th><td></td><td>-0.3</td><td></td><td></td><td></td></tr><tr><th>-40</th><td></td><td></td><td></td><td></td><td></td></tr></table>			x-coordinate							-40	-20	0	20	40	y-coordinate	40			0.4			20	-2.9			1.1		0			0.9			-20		-0.3				-40					
			x-coordinate																																																																																																																																							
			-40	-20	0	20	40																																																																																																																																			
	y-coordinate	40			0.476																																																																																																																																					
		20	1.274			1.738																																																																																																																																				
0				2.134																																																																																																																																						
-20			1.786																																																																																																																																							
-40																																																																																																																																										
		x-coordinate																																																																																																																																								
		-40	-20	0	20	40																																																																																																																																				
y-coordinate	40			0.478																																																																																																																																						
	20	1.236			1.757																																																																																																																																					
	0			2.153																																																																																																																																						
	-20		1.781																																																																																																																																							
-40																																																																																																																																										
		x-coordinate																																																																																																																																								
		-40	-20	0	20	40																																																																																																																																				
y-coordinate	40			0.4																																																																																																																																						
	20	-2.9			1.1																																																																																																																																					
	0			0.9																																																																																																																																						
	-20		-0.3																																																																																																																																							
-40																																																																																																																																										
z = 156 mm	<table><tr><th colspan="2"></th><th colspan="5">x-coordinate</th></tr><tr><th colspan="2"></th><th>-40</th><th>-20</th><th>0</th><th>20</th><th>40</th></tr><tr><th rowspan="4">y-coordinate</th><th>40</th><td></td><td></td><td>0.772</td><td></td><td></td></tr><tr><th>20</th><td>1.373</td><td></td><td></td><td>1.953</td><td></td></tr><tr><th>0</th><td></td><td></td><td>2.107</td><td></td><td></td></tr><tr><th>-20</th><td></td><td>1.742</td><td></td><td></td><td></td></tr><tr><th>-40</th><td></td><td></td><td></td><td></td><td></td></tr></table>			x-coordinate							-40	-20	0	20	40	y-coordinate	40			0.772			20	1.373			1.953		0			2.107			-20		1.742				-40						<table><tr><th colspan="2"></th><th colspan="5">x-coordinate</th></tr><tr><th colspan="2"></th><th>-40</th><th>-20</th><th>0</th><th>20</th><th>40</th></tr><tr><th rowspan="4">y-coordinate</th><th>40</th><td></td><td></td><td>0.806</td><td></td><td></td></tr><tr><th>20</th><td>1.408</td><td></td><td></td><td>1.991</td><td></td></tr><tr><th>0</th><td></td><td></td><td>2.123</td><td></td><td></td></tr><tr><th>-20</th><td></td><td>1.766</td><td></td><td></td><td></td></tr><tr><th>-40</th><td></td><td></td><td></td><td></td><td></td></tr></table>			x-coordinate							-40	-20	0	20	40	y-coordinate	40			0.806			20	1.408			1.991		0			2.123			-20		1.766				-40						<table><tr><th colspan="2"></th><th colspan="5">x-coordinate</th></tr><tr><th colspan="2"></th><th>-40</th><th>-20</th><th>0</th><th>20</th><th>40</th></tr><tr><th rowspan="4">y-coordinate</th><th>40</th><td></td><td></td><td>4.4</td><td></td><td></td></tr><tr><th>20</th><td>2.5</td><td></td><td></td><td>1.9</td><td></td></tr><tr><th>0</th><td></td><td></td><td>0.8</td><td></td><td></td></tr><tr><th>-20</th><td></td><td>1.4</td><td></td><td></td><td></td></tr><tr><th>-40</th><td></td><td></td><td></td><td></td><td></td></tr></table>			x-coordinate							-40	-20	0	20	40	y-coordinate	40			4.4			20	2.5			1.9		0			0.8			-20		1.4				-40					
			x-coordinate																																																																																																																																							
			-40	-20	0	20	40																																																																																																																																			
	y-coordinate	40			0.772																																																																																																																																					
		20	1.373			1.953																																																																																																																																				
0				2.107																																																																																																																																						
-20			1.742																																																																																																																																							
-40																																																																																																																																										
		x-coordinate																																																																																																																																								
		-40	-20	0	20	40																																																																																																																																				
y-coordinate	40			0.806																																																																																																																																						
	20	1.408			1.991																																																																																																																																					
	0			2.123																																																																																																																																						
	-20		1.766																																																																																																																																							
-40																																																																																																																																										
		x-coordinate																																																																																																																																								
		-40	-20	0	20	40																																																																																																																																				
y-coordinate	40			4.4																																																																																																																																						
	20	2.5			1.9																																																																																																																																					
	0			0.8																																																																																																																																						
	-20		1.4																																																																																																																																							
-40																																																																																																																																										
z = 136 mm	<table><tr><th colspan="2"></th><th colspan="5">x-coordinate</th></tr><tr><th colspan="2"></th><th>-40</th><th>-20</th><th>0</th><th>20</th><th>40</th></tr><tr><th rowspan="4">y-coordinate</th><th>40</th><td></td><td></td><td>0.559</td><td></td><td></td></tr><tr><th>20</th><td>1.351</td><td></td><td></td><td>1.935</td><td></td></tr><tr><th>0</th><td></td><td></td><td>2.058</td><td></td><td></td></tr><tr><th>-20</th><td></td><td>1.494</td><td></td><td></td><td></td></tr><tr><th>-40</th><td></td><td></td><td></td><td></td><td></td></tr></table>			x-coordinate							-40	-20	0	20	40	y-coordinate	40			0.559			20	1.351			1.935		0			2.058			-20		1.494				-40						<table><tr><th colspan="2"></th><th colspan="5">x-coordinate</th></tr><tr><th colspan="2"></th><th>-40</th><th>-20</th><th>0</th><th>20</th><th>40</th></tr><tr><th rowspan="4">y-coordinate</th><th>40</th><td></td><td></td><td>0.536</td><td></td><td></td></tr><tr><th>20</th><td>1.382</td><td></td><td></td><td>1.879</td><td></td></tr><tr><th>0</th><td></td><td></td><td>2.040</td><td></td><td></td></tr><tr><th>-20</th><td></td><td>1.525</td><td></td><td></td><td></td></tr><tr><th>-40</th><td></td><td></td><td></td><td></td><td></td></tr></table>			x-coordinate							-40	-20	0	20	40	y-coordinate	40			0.536			20	1.382			1.879		0			2.040			-20		1.525				-40						<table><tr><th colspan="2"></th><th colspan="5">x-coordinate</th></tr><tr><th colspan="2"></th><th>-40</th><th>-20</th><th>0</th><th>20</th><th>40</th></tr><tr><th rowspan="4">y-coordinate</th><th>40</th><td></td><td></td><td>-4.1</td><td></td><td></td></tr><tr><th>20</th><td>2.3</td><td></td><td></td><td>-2.9</td><td></td></tr><tr><th>0</th><td></td><td></td><td>-0.9</td><td></td><td></td></tr><tr><th>-20</th><td></td><td>2.1</td><td></td><td></td><td></td></tr><tr><th>-40</th><td></td><td></td><td></td><td></td><td></td></tr></table>			x-coordinate							-40	-20	0	20	40	y-coordinate	40			-4.1			20	2.3			-2.9		0			-0.9			-20		2.1				-40					
			x-coordinate																																																																																																																																							
			-40	-20	0	20	40																																																																																																																																			
	y-coordinate	40			0.559																																																																																																																																					
		20	1.351			1.935																																																																																																																																				
0				2.058																																																																																																																																						
-20			1.494																																																																																																																																							
-40																																																																																																																																										
		x-coordinate																																																																																																																																								
		-40	-20	0	20	40																																																																																																																																				
y-coordinate	40			0.536																																																																																																																																						
	20	1.382			1.879																																																																																																																																					
	0			2.040																																																																																																																																						
	-20		1.525																																																																																																																																							
-40																																																																																																																																										
		x-coordinate																																																																																																																																								
		-40	-20	0	20	40																																																																																																																																				
y-coordinate	40			-4.1																																																																																																																																						
	20	2.3			-2.9																																																																																																																																					
	0			-0.9																																																																																																																																						
	-20		2.1																																																																																																																																							
-40																																																																																																																																										

Table 6.4: Comparison of the calculated and measured dose for 9 measurements with treatment plan 2 for different positions of the ionization chambers. The left row displays the calculated dose [Gy], the middle column the measured dose [Gy] and in the right column the deviation is shown [%].

6.4.3 Results 2: film measurement

The film measurement was performed for the same two treatment plans. For these measurements only a relative comparison of the dose values is performed. Figure 6.16 shows the results for the first measurement. Displayed are the calculated dose distribution, the measured dose distribution, the gamma index and a comparison of both dose distributions.

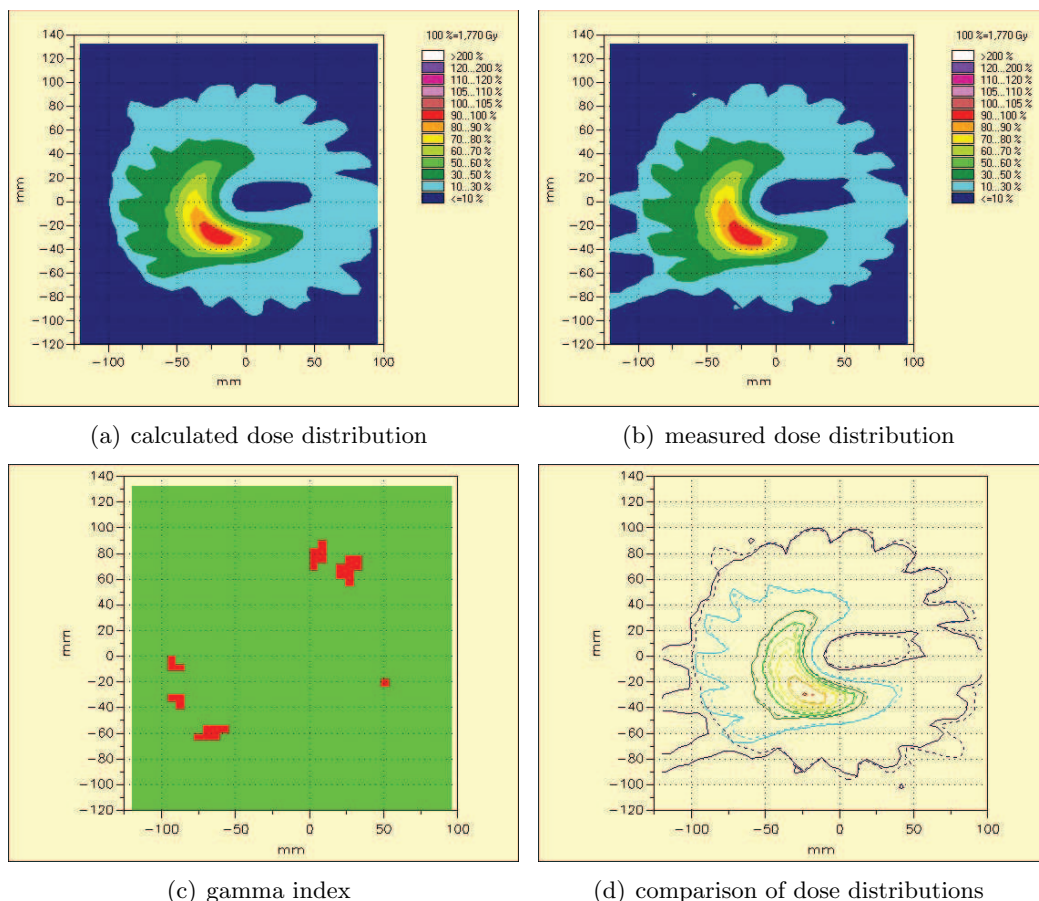


Figure 6.16: Film measurement for treatment plan 1. In the comparison of the dose distributions the dashed line represents the calculated dose distribution, the solid line represents the measured dose distribution.

The criteria for the calculation of the gamma index were a local dose difference of 3% and a distance to agreement of 3 mm. Dose values below 5% of the maximum dose in the calculated dose distribution were excluded from the comparison. Otherwise the area around the phantom would not pass the gamma test because no dose was calculated outside of the phantom, but a low dose was delivered to the film. The dose distributions are very similar, only in the low dose area there are some parts not passing the gamma test. In figure 6.17 dose profiles along the x-axis and y-axis are shown. In the profile along the y-axis the agreement between measured and calculated dose is good. Differences for high

doses are visible in the profile along the x-axis. The peak in the measured profile along the x-axis is a result of labeling the film with a needle to define a coordinate system.

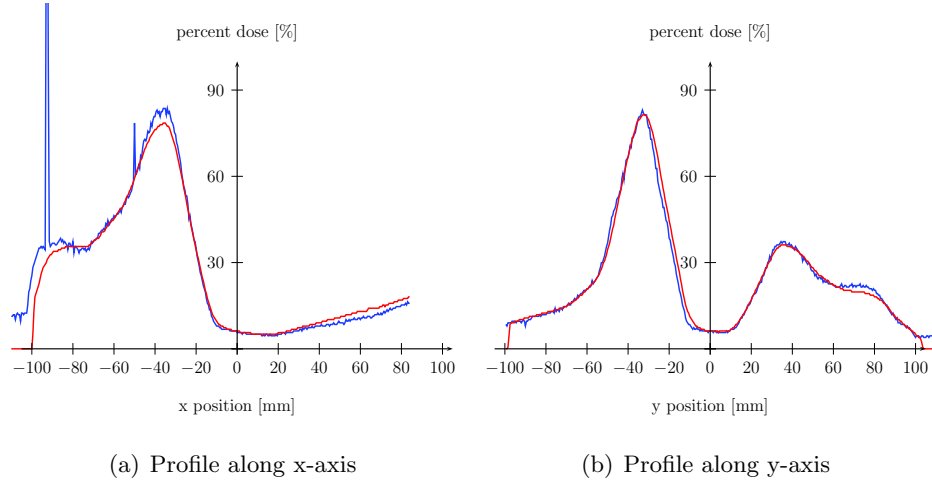


Figure 6.17: Dose profiles for film measurement 1. The measured profile is plotted in blue, the calculated in red.

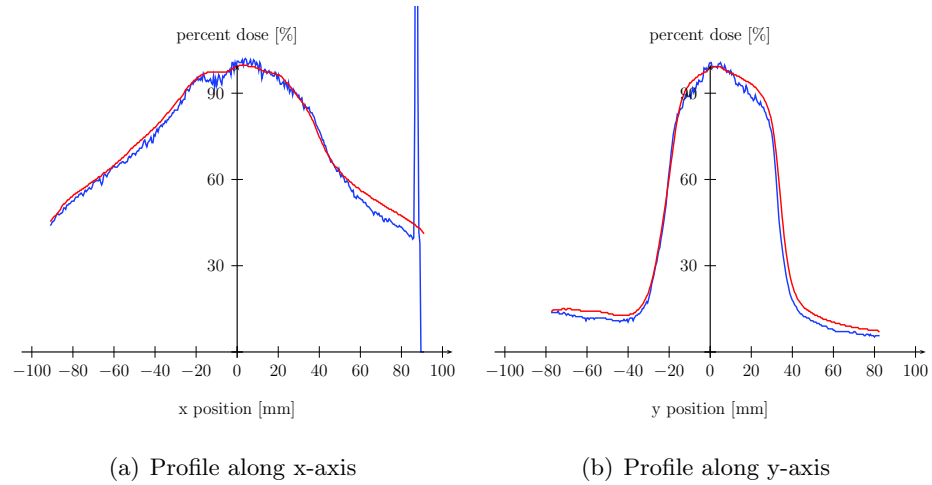


Figure 6.18: Dose profiles for film measurement 2. The measured profile is plotted in blue, the calculated in red.

The results of the second measurement are displayed in figure 6.19 and 6.18. Within the target volume the agreement of the measured and calculated dose values is within the acceptance criteria of the gamma test. For this measurement there is an increased deviation between the measurement and calculation within the low dose area. This is also visible in both dose profiles.

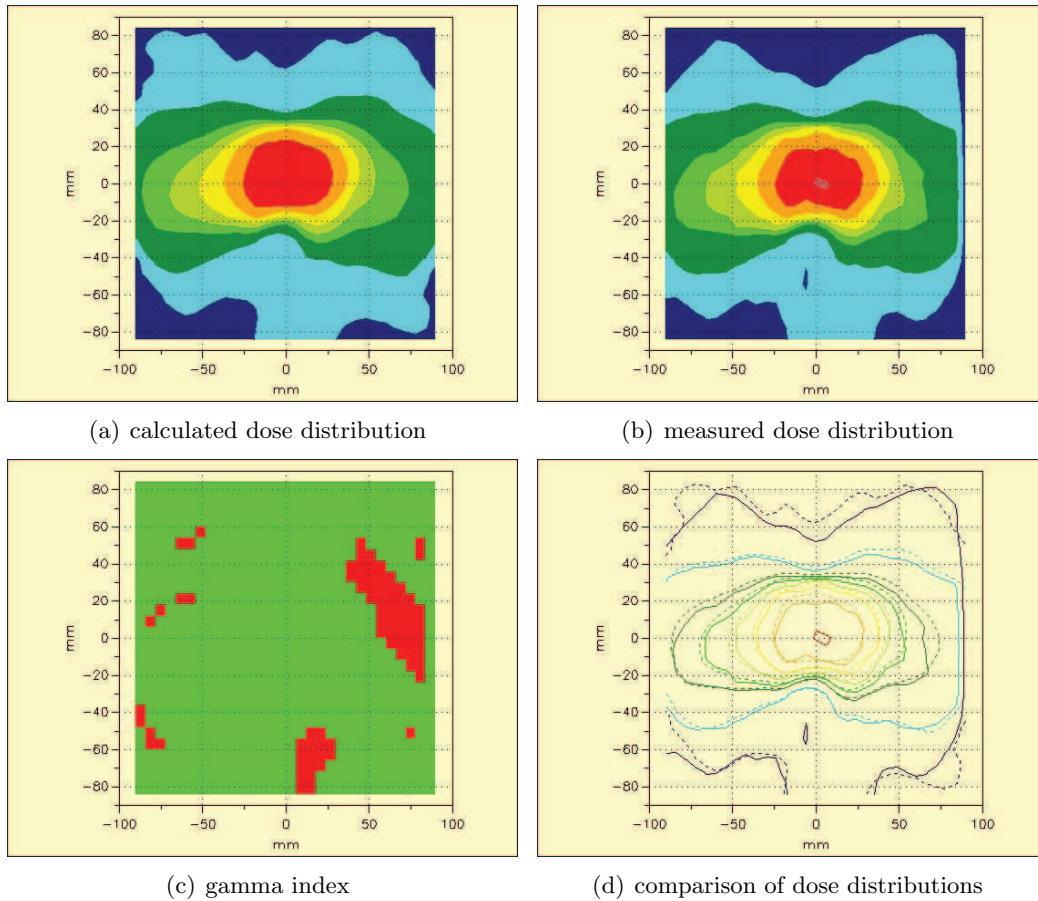


Figure 6.19: Film measurement for treatment plan 2. In the comparison of the dose distributions the dashed line represents the calculated dose distribution, the solid line represents the measured dose distribution.

6.5 Discussion

The measurements described in this chapter have shown the feasibility to perform arc-modulated cone beam therapy with a Siemens ArtisteTM linac. By using the DRCV modulation board it is possible to vary the dose rate during dose delivery in good agreement with the prescribed DRCV values. Within the limits imposed by the linac the dose rate could be changed quickly and accurately during treatment. For challenges such as the high dose rate at the beginning of the treatment a solution was presented. The rotation of the gantry during treatment is constant with the specified speed, except in the beginning of the rotation there are deviations from the specified gantry speed. An idea of how to avoid dose delivery errors imposed by a wrong gantry rotation speed at the beginning of a treatment is to start rotating the gantry a few degrees before starting the irradiation. It was shown that the dynamic control of the MLC is feasible and that there is a good agreement of the planned and realized leaf positions during treatment.

Even though it is feasible to perform dynamic rotation therapy with variable dose rate with the Siemens ArtisteTM linac there are further issues that need to be addressed in more detail. Especially for low doses there were differences between the measured and calculated dose values. One possible explanation for this is leakage radiation through the closed MLC leaves. Examples for three treatment fields for the prostate treatment plan are displayed in figure 6.20. These images show that there is a gap between closed leaves. The radiation coming through this gap might be a reason for an increased dose, which will be most pronounced in areas receiving low doses during a treatment.

In this example the leaves are closed at $x = 0$. To reduce the influence of leakage radiation through closed leaves it is better not to place them in the center of the field.

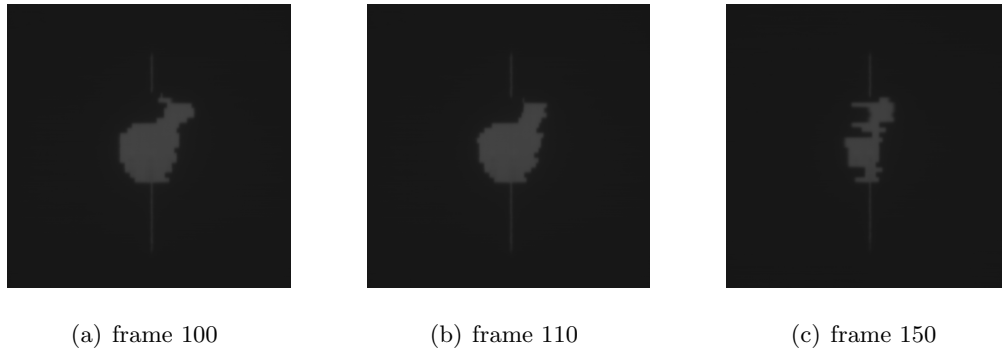


Figure 6.20: *Treatment fields for a prostate cancer treatment imaged with a flat panel detector. The time between image frames is 399 ms. At $x=0$ leakage radiation is coming through the closed leaf pairs.*

Both the dose rate modulation board and the modified control unit for the MLC are research developments which are not approved for patient treatments. Therefore the hardware realization for AMCBT described in this chapter is not certified for clinical use.

7 Discussion and conclusions

Arc-modulated cone beam therapy is a dose delivery technique that uses variable field shapes and field weights during irradiation. In this thesis an optimization concept for AMCBT was introduced. This treatment plan optimization algorithm was used to assess the treatment plan quality achievable for AMCBT against other intensity-modulated treatment techniques. Moreover the sensitivity of the plan quality for different hardware and planning related aspects was investigated. A dose delivery solution employing a dose rate modulation board and a dynamic MLC was developed and tested during this thesis project.

Optimization concept

The optimization concept presented in this thesis is a direct aperture optimization algorithm. Therefore field shapes and field weights are optimized directly and no sequencing step is required before the dose delivery. The mathematical optimization of the field weights is performed with a gradient algorithm and for the optimization of the field shapes a tabu search is used. The ability of the algorithm to obtain dose distributions of good quality was shown in this thesis.

For AMCBT there is only one aperture per beam direction. To use the same DAO concept for the optimization of treatment plans for fixed gantry IMRT the algorithm was extended to allow for several apertures per beam directions. First results have shown a sensitivity of the algorithm on the choice of the initial solution used for DAO planning for fixed gantry IMRT. Starting with target conformal field shapes does not result in clinically acceptable treatment plans. It is assumed that by choosing different initial aperture shapes the generation of treatment plans with a dose distribution quality similar to bixel weight optimized treatment plans is possible for fixed gantry IMRT. Presumably a reduction of the number of monitor units is possible with a DAO algorithm.

Limitations that are imposed by the dose delivery hardware were considered within the optimization concept. A detailed description of the implementation was given in section 3.2. There are mainly two assumptions made for this implementation which might not be the best choice for all cases. First, the treatment plan specific gantry speed depends on the weights of the beams and thus the number of monitor units that needs to be delivered within the angular interval between two beams. This approach is reasonable, for the delivery of a larger number of MUs the gantry needs to rotate slower. A treatment plan with a total of 500 MU could not be delivered with a dose rate of 300 MU/min and a gantry rotation speed of $360^\circ/\text{min}$ in a gantry rotation of 360° . Even with $v_{\text{Gantry}} = 216^\circ/\text{min}$ there would be no modulation of the dose rate possible if a total of 500 MU is required for a single arc treatment. Therefore, the gantry speed is calculated based on the mean dose

rate achievable with the linac and the number of MUs. The drawback of this approach is that it does not consider the complexity of a specific patient geometry and the amount of modulation needed to find the best treatment quality. Second, the gantry speed is calculated only once in the optimization. This is done after the weights for the initial field shapes were optimized and the first stopping criterium in the optimization algorithm is fulfilled. This approach is based on some example cases for which the sum of all weights at this point of the optimization was compared to the final value. For these cases the sum was similar. Still, for other cases there might be a bigger change during the optimization and it would be beneficial to calculate a new gantry speed during the optimization.

Limitations imposed by the MLC leaf speed did not lead to a degradation of the plan quality for any of the cases considered during this thesis project. In section 5.1 it was shown that for some cases the range of the dose rate stated above is not sufficient to completely exploit the potential advantages of dynamically modulated rotation therapy. The amount of modulation that was assumed for this analysis was estimated before implementing the dose rate modulation board. The measurements have shown that a restriction of the dose rate variation to 20 MU/min per second is possibly not necessary and that this limitation should be reconsidered. Experiments that were performed to find the maximum possible change of the dose rate showed that this value depends on the value of the DRCV. Therefore it might be better to include a percentage dose rate variation limitation instead of a fixed value.

Treatment plan quality

AMCBT treatment plans were assessed in comparison to fixed gantry IMRT treatment plans, to helical tomotherapy treatment plans and to "idealized IMRT" treatment plans. In comparison to fixed gantry IMRT the treatment plan quality achievable with AMCBT was at the same level. A benefit of AMCBT - besides reducing the time to treat a patient - was a lower number of MUs required for a specific treatment. This statement was made in a number of papers, e.g. for prostate cancer treatments the number of MUs could be reduced by up to 75% in one study [25], another study showed a reduction from 1819 MU for IMRT to 949 MU for RapidArc [48]. For head and neck cancer the number of MU decreased by nearly 60% [68] and for an integrated boost radiotherapy for bilateral breast treatments the monitor units were reduced from 1398 ± 301 MU for IMRT to 796 ± 121 MU for RapidArc [34], just to give a few examples. All these studies compared IMRT treatment plans that were planned with the traditional two step approach and RapidArc treatment plans generated with a DAO algorithm. Several studies comparing treatment plans for fixed gantry IMRT that were either optimized in two steps or with DAO also showed a reduction in MUs with DAO planning [51], [17], [66], [3], [13], [24]. However, one should compare DAO optimized fixed gantry IMRT plans with dynamic rotation therapy to fairly address the issue of required MU.

The comparison of AMCBT and "idealized IMRT", i.e. treatment plans that were optimized with the same number of beams but intensity-modulated fluence fields, showed for highly complex target geometries a benefit of intensity-modulated fields even for a high number of beam directions. Therefore a dose delivery in several arcs might lead to a better

treatment plan quality compared to a single arc. The number of arcs needed to get the optimal treatment plan quality was not examined yet.

The focus in the assessment of the treatment plan quality achievable with AMCBT was on the comparison with helical tomotherapy. The good dosimetric qualities of tomotherapy were demonstrated in several previous studies. For the first type of cancer considered in this study - prostate cancer - the dose distributions optimized for arc therapy were at least as good as plans optimized for tomotherapy. Moreover single arc therapy has the advantages of a faster dose delivery and a lower integral dose. From a shortened treatment time the patient can benefit in terms of comfort and less risk of organ movement. Moreover the patient throughput can be increased.

For the anal cancer patients the quality of the dose distribution was better for tomotherapy than for AMCBT. With helical tomotherapy, there is an improved sparing of the genitals and a very good dose coverage of the tumor. Nonetheless, the quality of dose distributions for single arc therapy is also of a high quality and seems to be clinically acceptable. Possibilities to further improve the quality of arc therapy could be the use of several arcs or non-coplanar beams. This would result in longer treatment times, but presumably the treatment time would still be shorter compared to the 10 minutes needed for tomotherapy. For the group of patients with a tumor in the head and neck region the treatment time for tomotherapy also exceeds 10 minutes. The very high dose gradients achievable with tomotherapy are especially helpful for the sparing of the parotid glands in close proximity to the boost volume. Moreover a very low dose to the normal tissue in the neck is possible with helical tomotherapy. With single arc therapy the dose to most organs at risk is higher compared to tomotherapy.

To summarize this treatment plan comparison study, the plan quality of tomotherapy treatment plans was not achieved with AMCBT therapy for all cases. For many clinical cases single arc therapy will offer a very good plan quality, e.g. for prostate cancer, whereas for very complex cases the dosimetric quality provided by tomotherapy was not achieved with AMCBT. Whether this is an inherent limitation of arc therapy in a single rotation or if the dose distribution could be improved with another optimization approach is a question of future research. However, the dose distributions achievable with single arc therapy seem to be also clinically acceptable for many cases. Furthermore this treatment technique has also advantages compared to tomotherapy, e.g. the faster treatment time and a lower integral dose. A reduction of the integral dose in tomotherapy would be possible with a sharper dose gradient in the superior and inferior borders of the field. This could be reached with a variable field width, as already proposed in the original work about tomotherapy [29].

Another advantage of arc therapy is the possibility to use a conventional linac for dose delivery and therefore other degrees of freedom are available, e.g. different angles for collimator, treatment couch and different beam energies.

Of course the results of these planning comparisons are largely influenced by the optimization method used for AMCBT and the planning approach used for the other treatment techniques. A more general approach to compare single arc therapy techniques with state-of-the-art intensity-modulated techniques was pursued in a paper titled ‘Single-Arc IMRT?’ [8]. The differences between fixed gantry IMRT, single-arc IMRT and tomotherapy are investigated for the archetypical IMRT example case [9]. For this example, the

optimal solution is calculable analytically and can therefore serve as a benchmark solution in comparison to the solutions achievable with the different delivery techniques. Tomotherapy provides the best dose shaping capabilities and comes closest to the optimal solution. The authors concluded that single-arc IMRT is an efficient dose delivery technique, but that for complex cases the quality of the dose distribution is not as good as for tomotherapy. Even this analytical approach led to a discussions on the capabilities of single arc therapy with variable dose rate, since the authors had to make assumptions on the implementation of the dose delivery techniques, e.g. the collimator angle ([41], [69]). Some considerations on a general theory for arc therapy with variable dose rate could be found in [74].

Sensitivity of plan quality

The stability of the treatment plan quality was examined for the inclusion of hardware constraints into the optimization algorithm, for different primary fluences, for the number of beam directions used for treatment planning, for different collimator angles, for different MLC leaf widths, for a restriction of the dose rate to constant values and for possible dose delivery errors.

Optimization of treatment plans for AMCBT with a non flattened beam results in dose distributions with good conformity to the tumor volume and sparing of adjacent OARs. For the three cases under investigation the differences in target coverage, conformity and OAR sparing were small. Disadvantages of removing the beam flattening filter are an increase in the number of monitor units needed for treatment and an approximately 5% increased mean dose inside the patient contour. Further research is necessary to analyse the possible treatment time reduction for the higher dose rate achievable without a beam flattening filter. Moreover, measurements need to be performed to verify the dose distributions that were calculated for the non-flattened primary fluence.

Even though more beam directions lead to a higher number of DOF for the planning process it was shown for the example of a prostate cancer patient that the quality of the dose distribution was not improved with 72 beams compared to 36 beams. Also for other example cases there was no improvement on the beam quality by increasing the number of beams from 36 beams to 51 beams. The sampling rate seems to be high enough to accurately model the dose distribution for the rotational dose delivery, at least an interpolation of the small number of beams to 360 beam directions showed only a slight influence on the dose distribution.

The choice of the collimator angle was shown to have an impact on the quality of the dose distribution. For many of the example patient cases a collimator angle of 0° was best. This is presumable based on the choice of the initial solution and might vary for other optimization concepts.

The standard setting used for the size of the bixels was $(5\text{ mm})^2$. As assumed, it was shown that wider MLC leaves result in an increased dose to the OARs.

A restriction of the dose rate to constant values results in a degradation of the plan quality for most cases. If the DOF to vary the field weights is turned off in the optimization only

the shape of the field could be varied to conform the dose to the target. If the restriction of a constant dose rate is not considered in the optimization and the dose distribution is recalculated for a constant dose rate with the field shapes that were optimized before, there is an even larger degradation of the plan quality.

The analysis of the sensitivity of AMCBT treatment plans against dose delivery errors showed a small influence of random MLC leaf displacements and bigger differences for systematic displacements. Dose rate errors particularly influenced the dose distribution if the dose rate was higher or lower as planned for the complete treatment. If the dose rate was only altered for very high and low values the influence was less distinctive. The dose distribution seems to be not very sensitive on an angular displacement of the gantry.

A more detailed analysis with the knowledge that was gained from the measurements would intensify the knowledge on the sensitivity of AMCBT treatment plans against dose delivery errors. For example the MLC measurements have shown small leaf displacements in particular at inflecting points in the leaf trajectory profiles and the influence of this on the dose distribution was not examined yet. For the gantry rotation only positioning errors were investigated. If the speed is systematically lower or faster for the complete treatment this would give the same results as a higher or lower dose rate. But how would a variation of the gantry rotation speed during irradiation influence the dose distribution? A recalculation of the dose distributions based on the information that was gained during irradiation (e.g. the MLC log files and the information on the flat panel images) is also an interesting project to further explore the influence of errors that might happen during irradiation.

Dose delivery

In this thesis a hardware solution for the performance of arc-modulated cone beam therapy was presented. First, AMCBT requires a linac with the ability to vary the dose rate during irradiation. The solution used for this thesis project is a board that interrupts the DRCV signaling pathway and multiplies the constant DRCV value with a modulation function. It was shown that with this solution a fast and accurate variation of the dose rate is possible. The second component needed for AMCBT is a dynamically controlled MLC. Comparisons of planned and realized leaf positions demonstrated the ability of the MLC to move the leaves in accordance with the planned positions. Information about the realized leaf positions was gained from the MLC log files and from flat panel images made during irradiation. Small deviations were visible at the inflection points of the leaf trajectory profiles.

The verification of dose distributions calculated for AMCBT showed deviations that in some cases exceeded the acceptance criteria. The absolute dosimetry with the ionization chambers showed a very good agreement of the calculated and measured values in a number of measurements for a treatment plan that was optimized for a prostate cancer patient. The results of the dose measurements were reproduced in a number of measurements very accurately. These measurements verified the dose distribution that was calculated for AMCT for a number of points in the dose distribution. However, the film measurements

indicate that for low doses there were deviations exceeding the acceptance criteria.

For the C-shaped dose distribution that was delivered with a decreasing dose rate and MLC leaves traveling back and forth there were deviations of up to almost 9% measured for doses below 0.3 Gy. Again, the similarity between two measurements was very high, e.g. for a calculated dose of 0.106 Gy doses of 0.114 Gy and 0.115 Gy were measured. So the difference between calculated and measured dose for this example is 0.009 Gy, which might be caused by leakage radiation and explain the deviation of 9%.

A more detailed and quantitative analysis of dosimetric verification measurements for AM-CBT is needed, like for example reported for RapidArcTM [28], [35], [26], [5], [4]).

In this thesis project the feasibility to deliver dose distributions that were optimized for AMCBT was shown and first experiments showed an acceptable agreement for dose values exceeding approximately 0.3 Gy.

To conclude, dose delivery in a single arc is a promising dose delivery technique. The newly developed optimization concept for AMCBT was used to demonstrate the ability to deliver dose distributions with a quality similar to other intensity-modulated treatment techniques in a single arc. For a variety of tumor types treatment plans of clinically acceptable quality were presented in this thesis. The feasibility to deliver those dose distributions was proven with a newly developed hardware solution which uses a dynamic MLC to shape the fields and an electronic board to vary the dose rate during irradiation.

Bibliography

- [1] <http://medicalphysicsweb.org/cws/article/research/32365>.
- [2] *Krebs in Deutschland*. Gesellschaft der epidemiologischen Krebsregister in Deutschland e.V. in Zusammenarbeit mit dem Robert Koch Institut, Saarbrücken, 5. überarbeitete, aktualisierte ausgabe edition, 2006.
- [3] E.E. Ahunbay, G.P. Chen, S. Thatcher, P.A. Jursinic, J. White, K. Albano, and X. Li. Direct aperture optimization-based intensity-modulated radiotherapy for whole breast irradiation. *Int J Radiat Oncol Biol Phys*, 67:1248–1258, 2007.
- [4] J. Bedford, Y. Lee, P. Wai, C. South, and A. Warrington. Evaluation of the Delta4 phantom for IMRT and VMAT verification. *Int.J.Radiation Oncology Biol.Phys.*, 54:167–176, 2009.
- [5] J. Bedford and A. Warrington. Comissioning of volumetric modulated arc therapy (VMAT). *Int.J.Radiation Oncology Biol.Phys.*, 73:537–545, 2009.
- [6] T. Bortfeld. Optimized planning using physical objectives and constraints. *Seminars in Radiation Oncology*, 9(1):20–34, 1999.
- [7] T. Bortfeld. Imrt: a review and preview. *Physics in Medicine and Biology*, 51:R363–R379, 2006.
- [8] T. Bortfeld and S. Webb. Single-Arc IMRT. *Physics in Medicine and Biology*, 54:N9–N20, 2009.
- [9] A. Brahme, J.E. Roos, and I. Lax. Solution of an integral equation encountered in radiation therapy. *Physics in Medicine and Biology*.
- [10] C. Cameron. Sweeping-window arc therapy: an implementation of rotational IMRT with automatic beam-weight calculation. *Physics in Medicine and Biology*, 50:4317–4336, 2005.
- [11] L. Cozzi, K.A. Dinshaw, S.K. Shrivastava, U. Mahantshetty, R. Engineer, D.D. Deshpande, S.V. Jamema, E. Vanetti, A. Clivio, G. Nicolini, and A. Fogliata. A treatment planning study comparing volumetric arc modulation with RapidArc and fixed field IMRT for cervix uteri radiotherapy. *Radiotherapy and Oncology*, 89:180–191, 2007.
- [12] M. De Ridder, K. Tournel, Y. Van Nieuwenhove, B. Engels, A. Hoorens, H. Everaert, B. Op de Beeck, V. Vinh-Hung, J. De Grève, G. Delvaux, D. Verellen, and G. Storme. Phase II Study of Preoperative Helical Tomotherapy for Rectal Cancer. *Int J Radiat Oncol Biol Phys*, 70:728–734, 2008.

- [13] B. Dobler, F. Pohl, L. Bogner, and O. Koelb. Comparison of direct machine parameter optimization versus fluence optimization with sequential sequencing in imrt of hypopharyngeal cancer. *Radiat Oncol*, 2:33, 2007.
- [14] R. Ferrigno, RA. Nakamura, and PE. Dos Santos Novaes. Radiochemotherapy in the conservative treatment of anal canal carcinoma: retrospective analysis of results and radiation dose effectiveness. *Int J Radiat Oncol Biol Phys*, 61:1136–1142, 2005.
- [15] C. Fiorino, I. Dell’Oca, and A Pierelli. Significant improvement in normal tissue sparing and target coverage for head and neck cancer by means of helical tomotherapy. *Radiother Oncol*, 78:276–282, 2006.
- [16] A. Fogliata, A. Clivio, G. Nicolini, E. Vanetti, and L. Cozzi. Intensity modulation with photons for benign intracranial tumours: A planning comparison of volumetric single arc, helical arc and fixed gantry techniques. *Radiotherapy and Oncology*, 89:254–262, 2009.
- [17] D. Georg, B. Kroupa, P. Georg, P. Winkler, J. Bogner, K. Dieckmann, and K. Potter. Inverse planning-a comparative intersystem and interpatient constraint study. *Strahlenther Onkol*, 182:473–480, 2006.
- [18] JP. Gerard. Chemoradiotherapy in treatment of cancer of the anal canal. *Cancer Radiother*, 2:708–712, 1998.
- [19] F. Glover and M. Laguna. *Tabu Search*. Kluwer Academic Publishers, Boston, 1997.
- [20] V. Gregoire, W. De Neve, and A. Eisbruch. Intensity-modulated radiation therapy for head and neck carcinoma. *Oncologist*, 12:555–564, 2007.
- [21] E.J. Hall. Intensity-modulated radiation therapy, protons, and the risk of second cancers. *I.J.Radiation Oncology Biol. Phys.*, 65(1):1–7, 2006.
- [22] ICRU. Prescribing, recording and reporting photon beam therapy. Bethesda: International Commission on Radiation Units and Measurements (Supplement to ICRU Report No. 50). *ICRU Report No. 62*.
- [23] ICRU. Prescribing, recording and reporting photon beam therapy. Bethesda: International Commission on Radiation Units and Measurements. *ICRU Report No. 50*, 1993.
- [24] S. Jones and M. Williams. Clinical evaluation of direct aperture optimization when applied to head-and-neck imrt. *Med Dosim*, 33:86–92, 2008.
- [25] F. Kjaer-Kristoffersen, L. Ohlhues, J. Medin, and S. Korreman. RapidArc volumetric modulated therapy planning for prostate cancer patients. *Acta Oncologica*, 48:227–232, 2009.
- [26] S. Korreman, J. Medin, and F. Kjaer-Kristoffersen. Dosimetric verification of RapidArc treatment delivery. *Acta Oncologica*, 48:185–191, 2009.

- [27] C.C. Ling, Y. Archambault, P. Bocanek, J. Zhang, T. LoSasso, and G. Tang. CScylla and Charybdis: Longer Beam-on Time or Lesser Conformality the Dilemma of Tomotherapy. *Int.J.Radiation Oncology Biol.Phys.*, 75:8–9, 2009.
- [28] C.C. Ling, P. Zhang, Y. Archambault, J. Bocanek, G. Tang, and T. LoSasso. Commissioning and quality assurance of RapidArc radiotherapy delivery systems. *Int.J.Radiation Oncology Biol.Phys.*, 72:575–581, 2008.
- [29] T.R. Mackie. Tomotherapy: A new concept for the delivery of dynamic conformal radiotherapy. *Medical physics*, 20:1709–1719, 1993.
- [30] M. Mehta, P. Hoban, and T.R. Mackie. Commissioning and Quality Assurance of RapidArc Radiotherapy Delivery System: In Regard to Ling et al. (Int J Radiat Oncol Biol Phys 2008;72:575-581): Absence of Data Does Not Constitute Proof: The Proof is in Tasting the Pudding. *Int.J.Radiation Oncology Biol.Phys.*, 75:4–6, 2009.
- [31] JJ. Meyer, CG. Willett, and BG. Czito. Emerging role of intensity-modulated radiation therapy in anorectal cancer. *Expert Rev Anticancer Ther*, 8:585–593, 2008.
- [32] MT. Milano, AB. Jani, and KJ Farrey. Intensity-modulated radiation therapy (IMRT) in the treatment of anal cancer: toxicity and clinical outcome. *Int J Radiat Oncol Biol Phys*, 63:354–361, 2005.
- [33] R. Mohan. Dueling Technologies: In regard to Ling et al. (Int J Radiat Oncol Biol Phys 2008;72:575-581). *Int.J.Radiation Oncology Biol.Phys.*, 75:6–7, 2009.
- [34] G. Nicolini, A. Clivio, A. Fogliata, E. Vanetti, and L. Cozzi. Simultaneous integrated boost radiotherapy for bilateral breast: a treatment planning and dosimetric comparison for volumetric modulated arc and fixed field intensity modulated therapy. *Radiation Oncology*, 4:27, 2009.
- [35] G. Nicolini, E. Vanetti, A. Clivio, A. Fogliata, S. Korreman, J. Bocamek, and L. Cozzi. The GLAaS algorithm for portal dosimetry and quality assurance of RapidArc, an intensity modulated rotational therapy. *Radiation Oncology*, 3:24, 2008.
- [36] ND. Nigro. An evaluation of combined therapy for squamous cell cancer of the anal canal. *Dis Colon Rectum*, 27:763–766, 1984.
- [37] S. Nill. *Development and application of a multi-modality inverse treatment planning system*. Dissertation, University of Heidelberg, Germany, 2001.
- [38] S. Nill, T. Bortfeld, and U. Oelfke. Inverse planning of intensity modulated proton therapy. *Z. Med. Phys.*, 14:35–40, 2004.
- [39] U. Oelfke and T. Bortfeld. Inverse planning for photon and proton beams. *Medical Dosimetry*, 26:113–124, 2001.
- [40] K. Otto. Volumetric modulated arc therapy: IMRT in a single gantry arc. *Medical physics*, 35:310–317, 2007.

- [41] K. Otto. Letter to the Editor on "Single-Arc IMRT". *Physics in Medicine and Biology*, 54:L37–L41, 2009.
- [42] D. Palma, E. Vollans, K. James, S. Nakano, V. Moiseenko, R. Shaffer, M. McKenzie, J. Morris, and K. Otto. Volumetric Modulated Arc Therapy for Delivery of Prostate Radiotherapy: Comparison With Intensity-Modulated Radiotherapy and Three-Dimensional Conformal Radiotherapy. *Int.J.Radiation Oncology Biol.Phys.*, 72:996–1001, 2008.
- [43] J.A. Penagaricano, N. Papanikolaou, and Y. Yan. Feasibility of cranio-spinal axis radiation with the Hi-Art tomotherapy system. *Radiother Oncol*, 76:72–78, 2005.
- [44] C.R. Ramsey, K.M. Langen, and P.A. Kupelian. A technique for adaptive image-guided helical tomotherapy for lung cancer. *Int J Radiat Oncol Biol Phys*, 64:1237–1244, 2006.
- [45] N. Rochet, F. Sterzing, and A. Jensen. Helical tomotherapy as a new treatment technique for whole abdominal irradiation. *Strahlenther Onkol*, 184:145–149, 2008.
- [46] Y. Rong, G. Tang, J. Welsh, B. Paliwal, and C. Yu. A collaborative dosimetric comparison for helical tomotherapy and single-arc intensity modulated arc therapy (IMAT) between two institutions. *Radiotherapy and Oncology*, 92:S24, 2009.
- [47] JK. Salama, LK. Mell, and DA. Schomas. Concurrent chemotherapy and intensity-modulated radiation therapy for anal canal cancer patients: a multicenter experience. *J Clin Oncol*, 4581-4586:25, 2007.
- [48] R. Shaffer, W. J. Morris, V. Moiseenko, M. Welsh, C. Crumley, S. Nakano, M. Schmuland, T. Pickles, and K. Otto. Volumetric Modulated Arc Therapy and Conventional Intensity-modulated Radiotherapy for Simultaneous Maximal Intraprostatic Boost: a Planning Comparison Study. *Clinical Oncology*, 21:401–407, 2009.
- [49] K. Sheng, J.A. Molloy, and P.W. Read. Intensity-modulated radiation therapy (IMRT) dosimetry of the head and neck: a comparison of treatment plans using linear accelerator-based IMRT and helical tomotherapy. *Int J Radiat Oncol Biol Phys*, 65:917–923, 2006.
- [50] D.M Shepard, M.A. Earl, X.A. Li, S. Naqvi, and C. Yu. Direct aperture optimization: A turnkey solution for step-and-shoot imrt. *Medical physics*, 29(6):1007–1018, 2002.
- [51] D.M Shepard, Z. Jiang, M.A. Earl, and C. Yu. Simplifying planning and delivery of imrt using direct aperture optimization. *I.J.Radiation Oncology Biol. Phys.*, 60(1):S178, 2004.
- [52] E.T. Soisson, W.A. Tome, and G.M. Richards. Comparison of linac based fractionated stereotactic radiotherapy and tomotherapy treatment plans for skull-base tumors. *Radiother Oncol*, 78:313–321, 2006.

- [53] J. Stein, T. Bortfeld, B. Dörschel, and W. Schlegel. Dynamic X-ray compensation for conformal radiotherapy by means of multi-leaf collimation. *Radiotherapy and Oncology*, 32:163–173, 1994.
- [54] F. Sterzing, MW. Munter, and A. Jensen. What is the impact of new radiotherapy techniques? *Hno*, 56:585–593, 2008.
- [55] F. Sterzing, K. Schubert, and G. Sroka-Perez. Evaluating target coverage and normal tissue sparing in the adjuvant radiotherapy of malignant pleural mesothelioma: Helical tomotherapy compared with step-and-shoot IMRT. *Radiother Oncol*, 2008.
- [56] F. Sterzing, K. Schubert, and G. Sroka-Perez. Helical Tomotherapy : Experiences of the First 150 Patients in Heidelberg. *Strahlenther Onkol*, 184:8–14, 2008.
- [57] M. Tacke. *Adaptation of High-Precision Radiotherapy to Moving Target Volumes in Real-Time Using Dynamic Multileaf Collimators*. Dissertation, University of Heidelberg, Germany, 2009.
- [58] K. Takahashi, J.A. Purdy, and Y.Y. Liu. Treatment planning system for conformation radiotherapy. *Radiology*, 147:567–573, 1983.
- [59] S. Ulrich. Entwicklung eines Optimierungskonzepts fuer die Kegelstrahl-Rotationstherapie. Master's thesis, University of Heidelberg, Germany, 2006.
- [60] S. Ulrich. Development of an optimization concept for arc-modulated cone beam therapy. In *International conference on the use of computers ICCR*, Toronto, Canada, 2007.
- [61] S. Ulrich, S. Nill, and U. Oelfke. Development of an optimization concept for arc-modulated cone beam therapy. *Physics in Medicine and Biology*, 52:4099–4119, 2007.
- [62] S. Ulrich, S. Nill, and U. Oelfke. Influence of hardware constraints on the plan quality in rotation therapy. *Radiotherapy and Oncology*, 88:S46, 2008.
- [63] S. Ulrich, S. Nill, and U. Oelfke. Dynamic rotational arc therapy with a non flattened beam. *Radiotherapy and Oncology*, S191:S46, 2009.
- [64] S. Ulrich, F. Sterzing, S. Nill, K. Schubert, K. Herfarth, J. Debus, and U. Oelfke. Comparison of arc-modulated cone beam therapy and helical tomotherapy for three different types of cancer. *Medical physics*, 36:4702–4710, 2009.
- [65] S. Ulrich, F. Sterzing, S. Nill, K. Schubert, K. Herfarth, J. Debus, and U. Oelfke. Investigation of the dose distribution quality achievable with arc-modulated cone beam therapy . In *IFMBE Proceedings of the World Congress on Medical Physics and Biomedical Engineering 2009, Munich, Germany, Vol. 25/I. Hrsg.: Dössel O., Schlegel W.C. Springer, Heidelberg*, pages 463–466, 2009.
- [66] B. Van Asselen, M. Schwartz, C. Van Vliet-Vroegindewij, J.V. Lebesque, B.J. Mijnheer, and M.F. Damen. Intensity-modulated radiotherapy of breast cancer using direct aperture optimization. *Radiother Oncol*, 79:162–169, 2006.

- [67] M. van Vulpen, C. Field, and C.P. Raaijmakers. Comparing step-and-shoot IMRT with dynamic helical tomotherapy IMRT plans for head-and-neck cancer. *Int J Radiat Oncol Biol Phys*, 62:1535–1539, 2005.
- [68] W.F.A.R. Verbakel, J. Cuijpers, D. Hoffmans, M. Bieker, B. Slotman, and S. Senan. Simultaneous integrated boost radiotherapy for bilateral breast: a treatment planning and dosimetric comparison for volumetric modulated arc and fixed field intensity modulated therapy. *Int.J.Radiation Oncology Biol. Phys.*, 74:252–259, 2009.
- [69] W.F.A.R. Verbakel, S. Senan, F.J. Lagerwaard, J.P. Cuijpers, and B.J. Slotman. Comments on "Single-Arc IMRT". *Physics in Medicine and Biology*, 54:L31–L34, 2009.
- [70] H. Vorwerk, G. Beckmann, M. Bremer, M. Degen, B. Dietl, R. Fietkau, T. Gsänger, R.M. Hermann, M.K.A. Herrmann, U. Höller, M. van Kampen, W. Körber, B. Maier, T. Martin, M. Metz, R. Richter, B. Siekmeyer, M. Steder, D. Wagner, C.F. Hess, E. Weiss, and H. Christiansen. The delineation of target volumes for radiotherapy of lung cancer patients. *Radiotherapy and Oncology*, 91:455–460, 2009.
- [71] C. Wang, S. Luan, G. Tang, Z. Chen, M.A. Earl, and C.X. Yu. Arc-modulated radiation therapy (AMRT): a single-arc form of intensity-modulated arc therapy. *Physics in Medicine and Biology*, 53:6291–6303, 2008.
- [72] S. Webb. The physical basis of imrt and inverse planning. *The British Journal of Radiology*, 76:678–689, 2003.
- [73] S. Webb. Motion effects in (intensity modulated) radiation therapy: a review. *Physics in Medicine and Biology*, 51:R403 – R425, 2006.
- [74] S. Webb and D. McQuaid. Some considerations concerning volume-modulated arc therapy: a stepping stone towards a general theory. *Physics in Medicine and Biology*, 54:4345–4360, 2009.
- [75] C.X. Yu. Intensity-modulated arc therapy with dynamic multileaf collimation: an alternative to tomotherapy. *Physics in Medicine and Biology*, 40:1435–1449, 1995.
- [76] M.J. Zelefsky, Z. Fuks, and S.A. Leibel. Intensity-modulated radiation therapy for prostate cancer. *Semin Radiat Oncol*, 12:229–237, 2002.

List of Figures

2.1	Workflow radiation therapy	5
2.2	Depth dose curve	7
2.3	Optimization loop	11
3.1	Generation of initial field shapes	16
3.2	Beams Eye View of different tumor types.	17
3.3	Flowchart tabu search algorithm	18
3.4	Generation of neighborhood	19
3.5	Optimization loop for AMCBT	22
3.6	Flowchart of optimization algorithm including hardware limitations	25
4.1	Dose distributions for IMRT and AMCBT for prostate cancer	28
4.2	DVH comparing IMRT and AMCB for prostate cancer	29
4.3	DVH comparing IMRT and AMCB for paraspinal case	30
4.4	Dose distributions for IMRT and AMCBT for paraspinal tumor	31
4.5	Dose distribution for IMRT and AMCBT for head tumor	32
4.6	DVH for IMRT and AMCBT for a head tumor	33
4.7	Dose distribution for AMCBT and tomotherapy for prostate cancer	36
4.8	Mean DVH comparing AMCBT and tomotherapy for prostate cancer	37
4.9	Dose distribution for AMCBT and tomotherapy for anal cancer	39
4.10	Mean DVH comparing AMCBT and tomotherapy for anal cancer	40
4.11	Dose distributions for AMCBT and tomotherapy for oropharynx cancer	41
4.12	Mean DVH comparing AMCBT and tomotherapy for oropharynx cancer	43
4.13	Dose values for AMCBT and "IMRT" for prostate cancer	44
4.14	DVH comparing AMCBT and "IMRT" for prostate cancer	44
4.15	Fluence maps for AMCBT and "IMRT"	46
5.1	Influence of hardware constraints on the number of MUs per beam	48
5.2	Leaf movement for AMCBT	49
5.3	Influence of hardware limitations on a DVH for a prostate case	49
5.4	Dose distributions for prostate example case	50
5.5	Influence of hardware limitations on the number of MUs: meningioma	50
5.6	DVH for a meningioma patient	51
5.7	Dose distributions for a meningioma patient	52
5.8	Primary fluence without flattening filter	53
5.9	Number of MUs for different primary fluences	54
5.10	DVHs for different primary fluences: Prostate cancer	54
5.11	DVHs for different primary fluences: Anal cancer	54
5.12	DVHs for different primary fluences: Oropharynx cancer	54

5.13	Dose distributions for different primary fluences	55
5.14	DVHs for different numbers of optimization steps	56
5.15	Progression of objective function and dose distribution during DAO	57
5.16	Treatment fields for AMCBT	58
5.17	DVH for different numbers of beam directions in treatment planning	59
5.18	Leaves crossing an OAR during dose delivery	60
5.19	Schematic illustration of different collimator angles	61
5.20	BEV for different collimator angles	62
5.21	DVH for different collimator angles	62
5.22	Number of open leaf pairs for different collimator angles	63
5.23	DVH for different bixel sizes	64
5.24	DVH and objective function values for a constant and variable dose rate	65
5.25	leaf displacements in the beam's eye view	66
5.26	DVHs for displaced leaf positions	67
5.27	Influence of dose rate errors on dose distribution	69
5.28	Number of MUs for imposed dose rate errors	70
5.29	MUs and dose distribution for a constant and variable dose rate	71
5.30	DVH for imposed errors in the gantry position	71
6.1	Dose rate control board	74
6.2	Measured dose for different DRCV values	76
6.3	Progression of DRCV against time	76
6.4	Rectangular radiation field measured with a flat panel detector	78
6.5	Progression of variable DRCV against time	78
6.6	Measured DRCV for prostate patient treatment	79
6.7	Planned vs. realized leaf movement: data from MLC control software logfile	81
6.8	Planned vs. realized leaf movement: data from flat panel detector	82
6.9	Planned vs. realized leaf movement for prostate treatment plan	83
6.10	Measured gantry rotation speed	84
6.11	Amplification of measured gantry position against time	84
6.12	Gantry rotation without panel in position	85
6.13	Phantoms	86
6.14	Dose distributions for measurements	86
6.15	Calculated dose profiles for treatment 1	88
6.16	Film measurement for treatment plan 1	90
6.17	Dose profiles for film measurement 1	91
6.18	Dose profiles for film measurement 2	91
6.19	Film measurement for treatment plan 2	92
6.20	Treatment fields imaged with a flat panel detector	93

List of Tables

4.1	Dose values for IMRT and AMCBT for prostata cancer	30
4.2	Mean dose values for tomotherapy and AMCBT for prostate cancer	37
4.3	Mean dose values for tomotherapy and AMCBT for anal cancer	40
4.4	Mean dose values for tomotherapy and AMCBT for oropharynx cancer . . .	42
4.5	Dose values for tomotherapy, AMCBT and "IMRT" for oropharynx cancer	45
5.1	Objective function for optimization runs with different hardware limitations	51
5.2	Dose values for different primary fluences	55
6.1	Maximum possible changes of the DRCV	75
6.2	Calculated dose values for treatment 1	87
6.3	Measured dose values for treatment 1	87
6.4	Calculated and measured dose values for treatment 2	89

Acknowledgment

This thesis was carried out in the group of physical models at the department of medical physics at the German Cancer Research Center. For their support during this time I want to express my gratitude to a number of people.

First of all I would like to thank Prof. Dr. Uwe Oelfke for giving me the opportunity to work on this project. I appreciate his helpful support and advice during the last 4 years.

For accepting me into the department of medical physics and his willingness to act as the second referee I am grateful to Prof. Dr. Wolfgang Schlegel.

Dr. Simeon Nill I would like to thank for his assistance, his competent help on problems I encountered, many good ideas to support this project and interesting discussions.

To all colleagues in the department and especially the group of physical models I express my gratitude for creating an enjoyable and friendly working environment and countless nice coffee and cake breaks we spent together. In particular I want to thank Emily Heath, PhD., for proof-reading of this manuscript, Bernhard Rhein, Peter Häring and Andrea Schwahofer for their help with linac, phantom or film related affairs and my various room-mates for their helpfulness and the enjoyable atmosphere they created in the office.

For their help in the treatment plan comparison of AMCBT with helical tomotherapy I would like to thank Dr. Florian Sterzing for sharing his medical knowledge and Dr. Kai Schubert from the university clinic in Heidelberg.

For their support in the development of the DRCV modulation board I am obliged to Kathalin Szep and Franz Dirauf, Siemens OCS and to Ulf Lanz, Siemens CO.

Lastly, I would like to thank Torben for his ceaseless encouragement.